**Performance Comparison of an Extended Kalman Filter and an Iterated Extended Kalman Filter for Orbit Determination of Space Debris with Poor Apriori Information and Intermittent Observations**

by

Jimmy Dale Hicks Jr.

A thesis submitted to the Graduate Faculty of
Auburn University
in partial fulfillment of the
requirements for the Degree of
Master of Science

Auburn, Alabama
December 8, 2012

Keywords: orbit debris, state estimation, kalman filtering



Approved by

David Cicci, Chair, Professor of Aerospace Engineering
John E. Cochran Jr., Professor and Head of Aerospace Engineering
John Hung, Professor of Electrical and Computer Engineering

Abstract

The growing space debris population threatens active and future missions bound for low earth orbit. The purpose of this study is to determine if an iterated extended Kalman filter (IEKF) can be used to yield better performance than the extended Kalman filter (EKF) in the orbit determination of space debris in low earth orbit with poor *apriori* data and intermittent observations. A simulation using two-body and $J_2$ effects was constructed using actual Space Surveillance Network sensor locations to generate experimental observational data, which contains multiple data outages. This data was then used to compare the performance of the EKF and IEKF. The filters are compared using the difference in the filter estimate and the true state and the difference in the estimated observation and true observation. An increase in estimate accuracy will allow for better predictions concerning the interaction of space debris with missions in low earth orbit.

The IEKF was chosen for this study due to the low number of observations provided and the large *apriori* covariance matrix. The state update step in the IEKF includes a local iteration that processes each observation until convergence of the state update is reached, which becomes the new best estimate of the state. Following the local convergence, the covariance matrix is updated using this new estimate, which prevents the covariance matrix from growing small as quickly as that of the EKF.

Acknowledgments

I would like to thank Dr. David Cicci for the opportunity to work on this research as well as his knowledge, invaluable support, and time in assisting in the development of this thesis. Our conversations have lead to a deeper understanding of orbit determination, and also the broader field of state estimation, which I greatly enjoy and have established as the foundation for my future career.

I would also like to thank the Aerospace Engineering Department for its financial assistance and Dr. John Cochran for providing a position in his lab where my interest in precise target tracking grew.

I would like to thank Dr. John Hung for the knowledge of what graduate school really meant. My conversations with him concerning his class led me to broader understanding of the types of planning and research needed to succeed.

Table of Contents

List of Figures

List of Tables

# Chapter 1

# Introduction

The term space debris refers to any human created object in space that is not part of an active mission. This broad scope includes propulsive stages, expired satellites, bolts, pieces of experimental hardware, fuel tanks that could contain unspent fuel, fragments from previous space debris collisions, and even a spare astronaut glove, which are a few examples of space debris cluttering low earth orbit (LEO) and geosynchronous orbit (GEO) paths [1]. Since the launch of *Sputnik 1* in 1957 by the Soviet Union, many nations have engaged in multiple space launches, some of which have created space debris.

While most modern satellites contain a GPS receiver to provide constant and accurate measurements, radar sites and optical telescopes provide the only tracking information available for space debris. This tracking data is used to determine the orbit of each debris object as accurately as possible. Radar sites and optical telescopes provide limited coverage due to environmental and mechanical constraints that can restrict the amount of observations available for a piece of space debris depending on the position, velocity, orientation, and size of each piece of debris. With the use of this intermittent data, traditional orbit determination methods that use the Extended Kalman Filter(EKF) can produce high residuals, which can lead to divergence and failure of the filter. High residuals for a piece of debris can increase the amount of fuel needed for nearby spacecraft to perform collision avoidance maneuvers. This can also lead to poor predictions for close pass scenarios, which may result in a collision.

This research evaluates the conceptual application of an Iterated Extended Kalman Filter (IEKF) to the orbit determination of space debris in order to improve the accuracy of the orbit determination process. The results of the IEKF are compared to those of a

standard EKF. This chapter will discuss the history of space debris, previous work done concerning the space debris environment, and a more detailed problem description for this specific study.

## 1.1 History

The primary concern of a growing space debris population is the increased probability of collision with active missions; however, a secondary concern also exists, which involves debris colliding with other debris, thereby generating even more debris. In 1978 Kessler and Cour-Palais discussed the concern of an exponential growth of space debris due to fragments from previous collisions causing future collisions. This exponential growth phenomenon due to objects being added to the LEO environment faster than they can decay from orbit was later defined as "The Kessler Syndrome." Kessler and Cour-Palais also discuss hypervelocity impacts, which cover the average impact velocity of 10 $km/s$ of objects in LEO. Kessler points out that a collision at this velocity can produce "very high instantaneous pressures" on the order of 1000 GPa or 1.45 $x$ $10^8$ $psi$, which will usually result in the catastrophic destruction of both objects [2]. NASA also notes that in LEO a 1 $cm$ diameter object with a few grams of mass contains the kinetic energy of a 250 $kg$ mass moving 100 $km/h$ [3].

Seeing a need to characterize the hazards of orbital debris to spacecraft and recommend mitigation techniques to help minimize the growth of the orbit debris environment, NASA established its orbital debris program in 1979. The orbital debris program grew quickly, and even included the construction of hypervelocity gun facilities in order to develop new shielding standards and technologies for the space shuttle and space station. In addition to providing research for shielding technologies, the orbital debris program also began to establish mitigation standards. One of these important standards is the "25-year low-Earth orbit lifetime limitation." Under this standard, NASA stated that "maneuverable spacecraft that are terminating their operational phases at altitudes of less than 2,000 $km$ above Earth shall be maneuvered to reduce their orbital lifetime, commensurate with 25-year low-Earth orbit

lifetime limitations [3]." This is very important in controlling the space debris environment as atmospheric drag will eventually decay the orbits of these expired satellites, removing them from the population [4].

The United States Strategic Command (USSTRATCOM) employs the Space Surveillance Network (SSN) to track and catalog objects approximately 10 $cm$ in diameter and larger to aid in the orbit determination of those objects. Debris size, sensor coverage, orbit parameters, and spacecraft/debris attitude (cross-sectional area visible by sensor) each affect the amount of tracking data available for every object. Kessler mentions the complexity of determining the space debris environment due to the difficulty to track objects smaller than 10 $cm$ in diameter [2]. Moreover, large gaps in data, can cause certain filtering methods to become unreliable and often biased, which can cause convergence to a trajectory other than the true trajectory or to divergence. NASA also suggested in 1999 that for every cataloged object of at least 10 $cm$ diameter there are ten 1 $cm$ and 10,000 1 $mm$ diameter untrackable objects. In 2011, there were approximately 22,000 cataloged objects, of which data is available publicly for about 16,000 of those objects [3].

In 2009, the collision between Iridium-33, an active communications satellite, and Cosmos-2251, a Russian satellite that ceased functioning in 1993, produced 1,275 pieces of debris that have been cataloged. Prediction software estimated a close approach between the two satellites; however, that prediction was only one of many conjunctions that were generated to warn of a pass within 5 $km$. Improvements in modeling, tracking, or filtering the data from measurements could reduce the uncertainty involved in forecasting close similar approaches [4].

In contrast to the accidental collision, the intentional destruction of the Chinese government's Fengyun-1C spacecraft, to test its anti-satellite weapon, produced 3,135 pieces of trackable debris. According to a NASA debris news update [5], the number of orbital debris 1 $cm$ in diameter and larger associated with this satellite destruction is at least 150,000. The amount of debris generated by these two collisions has been said to have effectively negated

the work completed to mitigate the growth of the space debris environment for the past twenty years [3].

### 1.2 Previous Research

Interactions with the space debris environment have been described as being active or passive. Active methods involve techniques that directly interact with the debris, which include the use of tethered satellites, projected lasers, robotics, and other similar techniques. While these methods are expensive, complicated, and largely untested, they could be used to alter the orbit of space debris to prevent collisions of debris with other debris as well as active missions. Passive methods involve techniques that do not physically interact with the debris. These methods include improvements to filtering methods, radar technology, and mitigation techniques similar to NASA's 25-year low-Earth orbit lifetime requirement. Through these methods, the position and velocity of the debris can be estimated with less error, which can lead to fewer collisions with active missions.

In 2008, Liou and Johnson[6] stated that the space debris environment is unstable, and mitigation techniques involving limiting the lifetime of expired satellites to 25 years will not be able to stabilize the population growth. In order to control the growth of the debris environment, they suggest the removal of large debris that has high collision probability. In their sensitivity study, the authors did not explore the technical or economic details of removing high-risk large space debris. If twenty debris objects are removed per year beginning in 2020, they predict the debris environment will stabilize by approximately 2080 [6]. Kessler revisited this phenomenon in 2010, and added that guidelines created in the last ten years must be adhered to while also deploying an active method to retrieve the most likely future debris sources in an attempt to prevent future spacecraft operators from facing limited spacecraft lifetimes due to collisions [7].

In 2012, Sibert and Borgeson[8] wrote a paper focused on the number of detailed conjunction assessments that must be performed and number of collision avoidance maneuvers

required to maintain a safe separation between objects. They began by showing that the orbital debris environment has already reached a stage where The Kessler Syndrome has taken over by presenting data that shows the debris environment growing even with zero future launches. In their paper, they also show that the number of conjunctions and collision avoidance maneuvers can be significantly reduced by reducing any or all of the following: state vector position error at time of update, state vector position error growth rate, and the delay between state vector updates. The most interesting part of their paper shows that improving the previously mentioned tracking performance significantly outweighs actual debris removal due to "very few debris objects turn[ing] out to be reliable repeat offenders[8]."

## 1.3 Problem Description

The growing debris population, shown in Figure 1.1, provided by the NASA Debris Program Office, coupled with the unpredictable nature of debris has created a need for orbit determination methods capable of obtaining more accurate estimates from fewer observations.

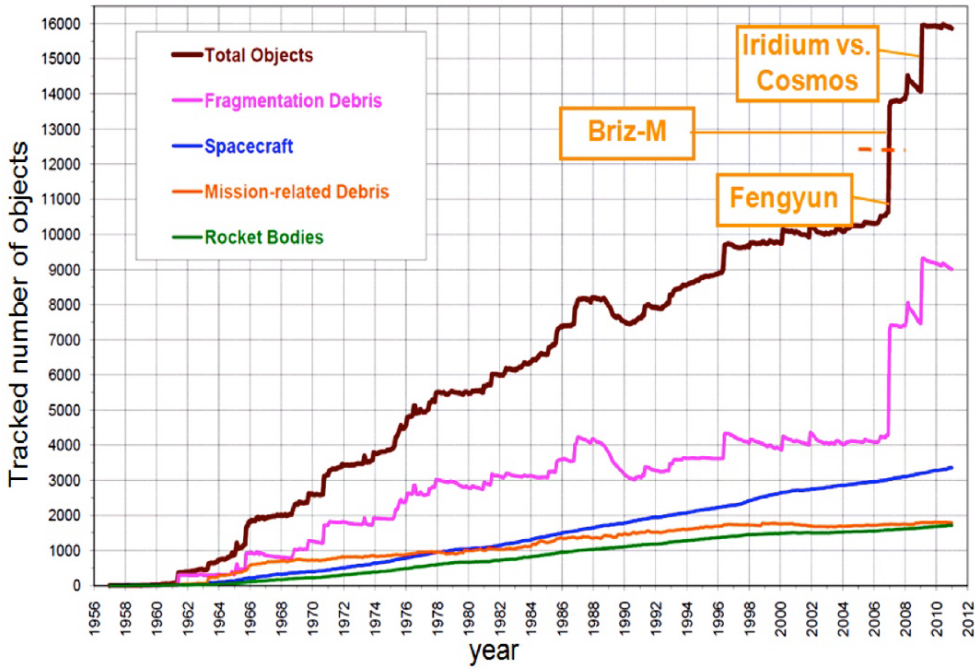


Figure 1.1: Debris Environment Trends

The purpose of this study is to determine if an Iterated Extended Kalman Filter can be used to yield better performance than the Extended Kalman filter in the orbit determination of space debris with poor *apriori* data and intermittent observations. A simulation was constructed using actual USN sensor locations to generate experimental observational data. This data was then used to compare the performance of the EKF and IEKF.

Changes to the orbital parameters of the debris were analyzed to determine the effects on filter performance. These initial conditions included variations to the following: altitude, inclination, longitude of the ascending node, argument of perigee, and true anomaly.

It was necessary to determine the performance characteristics in order to define the comparison of the two filters. The difference between the estimated state and actual state was chosen as the first characteristic. Since the actual state is not available in a realistic application, the second characteristic to be compared was the residuals of the estimates.

# Chapter 2

# Relevant Theory

The first step in developing a simulation is to select the specific coordinate systems and dynamical model. Orbit determination can use multiple reference frames, and many different dynamical models. First, the coordinate systems will be introduced. Following the coodinate systems, the equations of motion, orbital elements, and coordinate transformations will be defined. A number of assumptions and limitations were taken into account and addressed during this research. Gravity was modeled as the gradient of the geopotential function using two-body and $J_2$ effects only. Atmospheric drag was not modeled, which had no effect on the research as the measurements were generated using the same assumption. No other perturbation effects were involved.

## 2.1 Reference Frames

### 2.1.1 Earth Centered Inertial Coordinate System (ECI)

The origin of the ECI coordinate system, also referred to as the Geocentric equatorial coordinate system, is the center of the earth. The coordinate system is right-handed and has the following properties: the **X** axis points towards the vernal equinox with unit vector **I**, the **Z** axis points in the direction of the north pole with unit vector **K**, and the fundamental XY-plane coincides with the equatorial plane, defining the **Y** axis with unit vector **J**. The coordinate system is not fixed to the earth, and therefore doesn't rotate with it, but rather the earth rotates relative to it. The ECI coordinate system is represented in Figure 2.1.

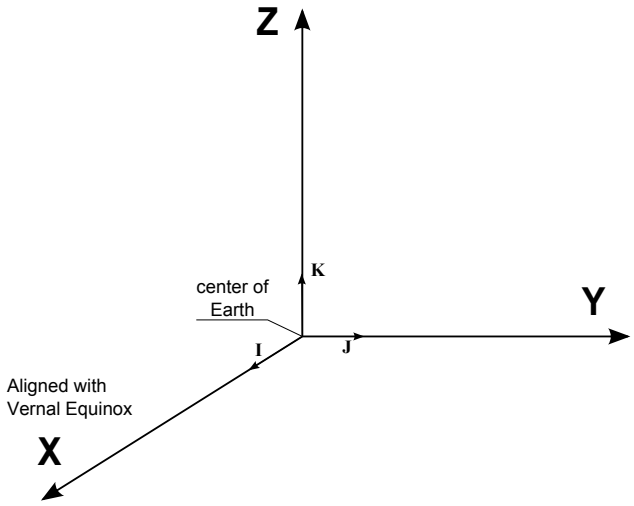


Figure 2.1: ECI coordinate system

### 2.1.2 Earth-Centered, Earth-Fixed Coordinate System (ECEF)

The origin of the ECEF coordinate system, is the center of the spherical earth. The coordinate system is right-handed and has the following properties: the $\mathbf{X}_E$ axis points towards the Greenwich meridian with unit vector $\mathbf{i}$, the $\mathbf{Z}_E$ axis points in the direction of the north pole with unit vector $\mathbf{k}$, and the fundamental plane coincides with the equatorial plane, defining the $\mathbf{Y}_E$ axis with unit vector $\mathbf{j}$. The ECEF coordinate system rotates with the earth, and therefore is not an inertial coordinate system. Tracking station coordinates are typically provided in this system. See Figure 2.2 for a ECEF coordinate system compared with the ECI system. Angle $\theta$ is known as the sidereal angle.

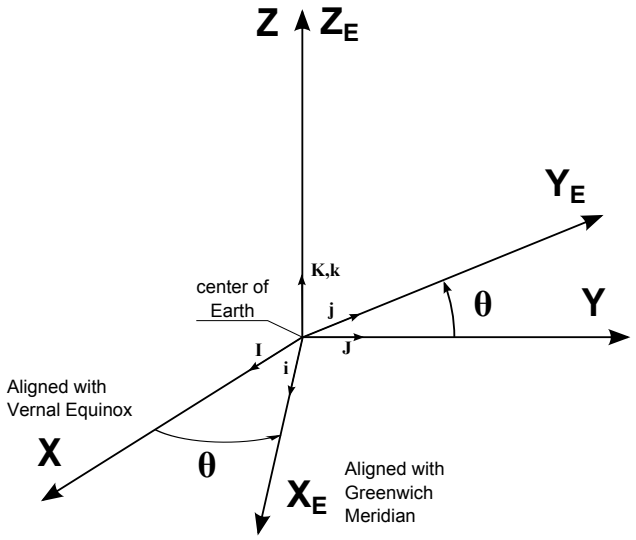


Figure 2.2: ECEF coordinate system

### 2.1.3 Perifocal Coordinate System

The fundamental plane of the perifocal coordinate system is the orbital plane. The coordinate system is right-handed and has the following properties: the **P** axis points towards perigee, the **Q** axis lies in the orbital plane rotated 90 degrees from **P**, and the **W** axis is perpendicular to the orbital plane and aligned with the angular momentum vector. The perifocal coordinate system is shown in Figure 2.3.

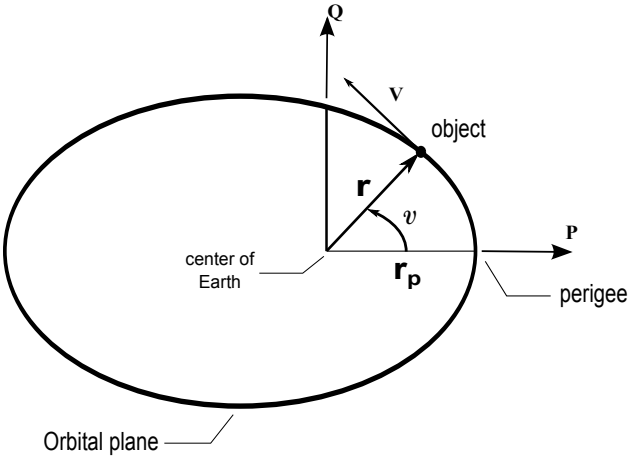


Figure 2.3: Perifocal coordinate system

## 2.2 Two-body Equations of Motion

Newton's second law of motion states that the sum of the external forces acting on a particle with mass, $m$, position, $\mathbf{r}$, and velocity, $\mathbf{v}$, is equal to the time rate of change of the product of the mass and velocity of the particle, which is represented in Equation 2.1.

$$\sum \mathbf{F} = \frac{d}{dt}(m\mathbf{v}) \tag{2.1}$$

If the mass of the particle is constant with respect to time, Equation 2.1 becomes Equation 2.2 where $\ddot{\mathbf{r}}$ represents the acceleration.

$$\sum \mathbf{F} = m\ddot{\mathbf{r}} \tag{2.2}$$

Netwon's law of universal gravitation states that any two particles exert a gravitational force on one another with magnitude,

$$F = G\frac{m_1 m_2}{r^2} \tag{2.3}$$

where $m_1$ and $m_2$ are the masses of the particles, $G$ is the universal gravitational constant, and $r$ is the magnitude of the position vector between them [9]. In the formulation of the two-body problem, the masses of those two bodies are assumed to be point masses, which satisfies the assumption of particles used in the formulation of Newton's laws.

While Newton's second law is valid in an inertial coordinate system, it can be modified to be valid in the geocentric equatorial (ECI) coordinate system shown in Figure 2.1. In this coordinate system, the acceleration of mass $m_2$ relative to the Earth due to two-body effects can be shown in Equation 2.4.

$$\ddot{\boldsymbol{r}} = -\frac{\mu}{r^3}\boldsymbol{r} \tag{2.4}$$

The gravitational parameter, $\mu$, is defined such that

$$\mu = G(m_1 + m_2) \tag{2.5}$$

The motion of $m_2$ relative to $m_1$ in the ECI coordinate system is shown in Figure 2.4.

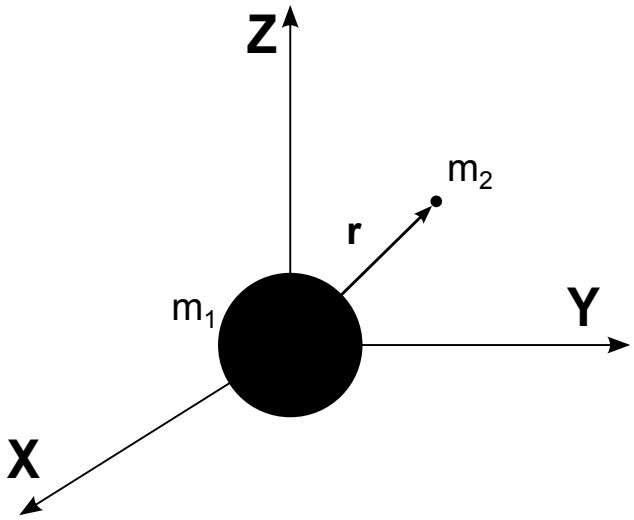


Figure 2.4: Two-body problem in a relative coordinate system

## 2.3 $J_2$ Perturbation

It is well known that the Earth is a non-spherical, inhomogeneous body and not a point mass. To model this non-uniform mass distribution, the equations of motion canl be presented as the gradient of the gravity potential function $U$ in Equation 2.6.

$$\ddot{\boldsymbol{r}} = \vec{\nabla} U \tag{2.6}$$

The dominating member of this gravity potential function is referred to as the oblateness of the Earth, $J_2$. The oblateness of the Earth, which is a bulge of mass symmetric about the equator, is often modeled in orbit determination due to it being approximately 1000 times larger than any of the other perturbation forces in LEO. The $J_2$ perturbation causes short period, long period, and secular changes in the orbital elements as presented in Table 2.1.

Table 2.1: $J_2$ changes in the orbital elements

| Periodic | Secular |
|---|---|
| a (semi-major axis) | $\Omega$ (Longitude of the Ascending Node) |
| e (eccentricity) | $\omega$ (Argument of periapsis) |
| i (inclination) | $\nu$ (True anomaly) |

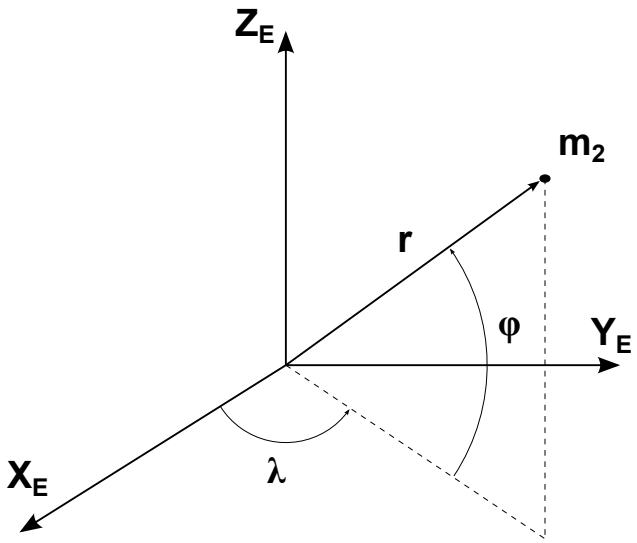


Figure 2.5: Orbit in Spherical Coordinates

In spherical coordinates, shown in Figure 2.5, the potential function of the $J_2$ perturbation is given in Equation 2.7 [10], where $J_2$ is the oblateness constant, $r_e$ is the mean radius of the Earth, $\phi$ is the latitude, and $\lambda$ is the longitude.

$$U_{J_2} = \frac{-\mu}{r} J_2 \left(\frac{r_e}{r}\right)^2 \left(\left(\frac{3}{2}\right) sin(\phi) - \left(\frac{1}{2}\right)\right) \tag{2.7}$$

The acceleration on $m_2$ due to $J_2$ is obtained by taking the gradient of $U_{J_2}$. The equations of motion of $m_2$ can then be expressed by Equation 2.8 as

$$\ddot{\boldsymbol{r}} = -\frac{\mu}{r^3}\boldsymbol{r} + \vec{\nabla} U_{J_2} \tag{2.8}$$

Appendix A provides the transformation of $\vec{\nabla} U_{J_2}$ into the ECI coordinate frame, for which the result is presented in Equation 2.9, where $X_1$, $X_2$, and $X_3$ are the **I**, **J**, and **K** components of the ECI position vector .

$$\vec{\nabla} U_{J_2} = \ddot{\boldsymbol{r}}_{J_2} = \frac{\frac{3}{2}\mu J_2 r_e^2}{r^7} \begin{bmatrix} X_1\left(5X_3^2 - r^2\right) \\ X_2\left(5X_3^2 - r^2\right) \\ X_3\left(5X_3^2 - 3r^2\right) \end{bmatrix} \tag{2.9}$$

The updated equations of motion will consist of the two-body effects combined with the $J_2$ effects. This is presented in Equation 2.10.

$$\mathbf{a} = -\frac{\mu}{r^3} \begin{bmatrix} X_1 \\ X_2 \\ X_3 \end{bmatrix} + \frac{\frac{3}{2}\mu J_2 r_e^2}{r^7} \begin{bmatrix} X_1\left(5X_3^2 - r^2\right) \\ X_2\left(5X_3^2 - r^2\right) \\ X_3\left(5X_3^2 - 3r^2\right) \end{bmatrix} \tag{2.10}$$

## 2.4 Orbital Plane Orientation in Space

The use of orbital elements is a common way to describe an orbit in three-dimensional space. Instead of solely dealing with position and velocity vectors, one can use a set of the orbital elements that completely describe the orbit. For this problem, the classical Keplerian orbital elements set will be used. The classical orbital elements are as follows (also see Figure 2.6) [11]:

1. Semi-major axis ($a$) - specifies the size of the orbit

2. Eccentricity ($e$) - specifies the shape of the orbit

3. Inclination ($i$) - specifies the angle between the equatorial plane and orbital plane (one of two elements that specify the orientation of the orbit plane)

4. Longitude of the ascending node ($\Omega$) - specifies the angle measured counterclockwise in the $XY$ plane of the ECI system from the $X$ axis to the point where the spacecraft crosses the equatorial plane from south-to-north (one of two elements that specify the orientation of the orbit plane)

5. Argument of perigee ($\omega$) - specifies the angle measured in the orbit plane in the direction of motion, from the ascending node to perigee (specifies the orientation of the orbit in the orbit plane)

6. True anomaly ($\nu$) - measured from periapsis to **r** in the direction of travel (specifies where on the orbit the spacecraft is located at any instant in time)

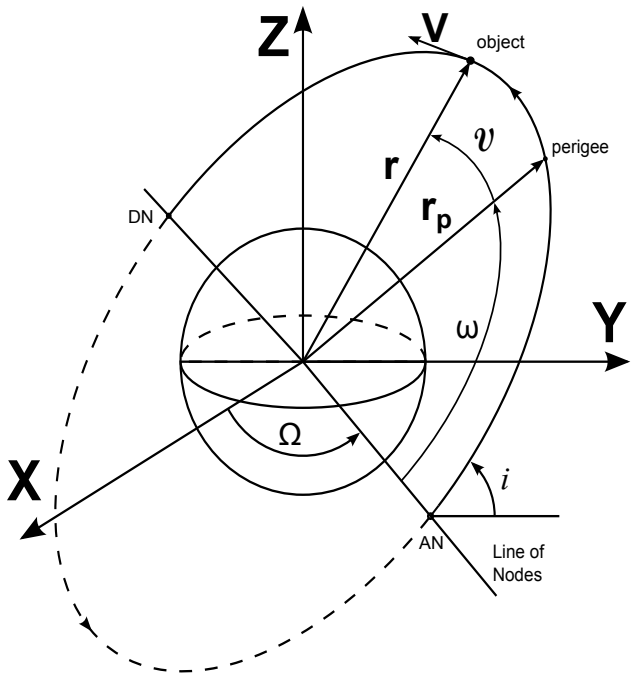


Figure 2.6: Orbital Elements

## 2.5 Coordinate Transformations

Orbital data can be represented by different values in different coordinate systems. Orbit determination deals with multiple types of data from various coordinate frames, and it is important to be able to clearly transform data from one system to another. This section discusses the necessary coordinate transformations used in this research.

### 2.5.1 Obtain ECI position and velocity vectors from the Keplerian orbital elements

Given the set of Keplerian orbital elements ($a$, $e$, $i$, $\Omega$, $\omega$, $\nu$), calculate $\mathbf{r}$ and $\mathbf{v}$ as follows [10]:

Step 1 - Calculate the parameter, or semi-latus rectum, $p$

$$p = a(1 - e^2) \tag{2.11}$$

Step 2 - Calculate r using the trajectory equation

$$r = \frac{p}{1 + e \cdot cos(\nu)} \tag{2.12}$$

Step 3 - Calculate the perifocal position vector

$$\mathbf{r_p} = \begin{bmatrix} r \cdot cos(\nu) \\ r \cdot sin(\nu) \\ 0 \end{bmatrix} \tag{2.13}$$

Step 4 - Calculate the perifocal velocity vector

$$\mathbf{v_p} = \begin{bmatrix} -\sqrt{\frac{\mu}{p}} \cdot sin(\nu) \\ \sqrt{\frac{\mu}{p}} \cdot (e + cos(\nu)) \\ 0 \end{bmatrix} \tag{2.14}$$

Step 5 - Calculate the transformation matrix from the perifocal to ECI

$$[T] = \begin{bmatrix} cos(\Omega)cos(\omega) - sin(\Omega)cos(i)sin(\omega) & -cos(\Omega)sin(\omega) - sin(\Omega)cos(i)cos(\omega) & sin(\Omega)sin(i) \\ sin(\Omega)cos(\omega) + cos(\Omega)cos(i)sin(\omega) & -sin(\Omega)sin(\omega) + cos(\Omega)cos(i)cos(\omega) & -cos(\Omega)sin(i) \\ sin(i)sin(\omega) & sin(i)cos(\omega) & cos(i) \end{bmatrix}$$

Step 6 - Calculate the ECI position and velocity vectors

$$\mathbf{r} = [T]\mathbf{r_p} \tag{2.15}$$

$$\mathbf{v} = [T]\mathbf{v_p} \tag{2.16}$$

### 2.5.2 Calculate the classical Keplerian orbital elements from ECI position and velocity vectors

Step 1 - Calculate the orbital eccentricity, $e$

$$r = |\vec{\mathbf{r}}|$$

$$v = |\vec{\mathbf{v}}|$$

$$\mathbf{e} = \left(\frac{v^2}{\mu} - \frac{1}{r}\right)\mathbf{r} - \frac{1}{\mu}\left(\mathbf{r}\cdot\mathbf{v}\right)\mathbf{v}$$

$$e = |\mathbf{e}| \tag{2.17}$$

Step 2 - Calculate the semi-major axis, $a$

$$\mathbf{h} = \mathbf{r} \times \mathbf{v}$$

$$h = |\mathbf{h}|$$

$$p = \frac{h^2}{\mu}$$

$$a = \frac{p}{1 - e^2} \tag{2.18}$$

Step 3 - Calculate the inclination, $i$

$$h_K = \mathbf{h} \cdot \mathbf{K}$$

$$i = \cos^{-1}\left(\frac{h_K}{h}\right) \tag{2.19}$$

Step 4 - Calculate the longitude of the ascending node, $\Omega$, and determine the correct quadrant

$$\mathbf{n} = \mathbf{K} \times \mathbf{h}$$

$$\mathbf{n} = \begin{bmatrix} n_I \\ n_j \\ 0 \end{bmatrix} \begin{bmatrix} \mathbf{I} & \mathbf{J} & \mathbf{K} \end{bmatrix}$$

$$n = |\mathbf{n}|$$

$$\Omega = \cos^{-1}\left(\frac{n_I}{n}\right) \tag{2.20}$$

$$\text{If } n_J < 0, \text{ then } \Omega > 180^\circ \rightarrow \Omega = 360^\circ - \Omega \tag{2.21}$$

$$\text{If } n_J > 0, \text{ then } \Omega < 180^\circ \tag{2.22}$$

Step 5 - Calculate the argument of periapsis, $\omega$, and determine the correct quadrant

$$\omega = \cos^{-1}\left(\frac{\mathbf{n} \cdot \mathbf{e}}{n\, e}\right) \tag{2.23}$$

$$\text{If } e_K > 0, \text{ then } \omega > 180^\circ \rightarrow \omega = 360^\circ - \omega \tag{2.24}$$

$$\text{If } e_K < 0, \text{ then } \omega < 180^\circ \tag{2.25}$$

Step 6 - Calculate the true anomaly, $\nu$, and determine the correct quadrant

$$\nu = \cos^{-1}\left(\frac{\mathbf{e} \cdot \mathbf{r}}{e\, r}\right) \tag{2.26}$$

$$\text{If } \mathbf{r} \cdot \mathbf{v} < 0, \text{ then } \nu > 180^\circ \rightarrow \nu = 360^\circ - \nu \tag{2.27}$$

$$\text{If } \mathbf{r} \cdot \mathbf{v} > 0, \text{ then } \nu < 180^\circ \tag{2.28}$$

### 2.5.3 ECI to ECEF

To convert from the ECI coordinate frame to the ECEF coordinate frame, rotate through the sidereal angle, $\theta$, about the Z axis, as shown in Figure 2.2. This transformation is produced in Equation 2.29.

$$\boldsymbol{r}_{ECEF} = \begin{bmatrix} cos(\theta) & sin(\theta) & 0 \\ -sin(\theta) & cos(\theta) & 0 \\ 0 & 0 & 1 \end{bmatrix} \boldsymbol{r}_{ECI} \tag{2.29}$$

# Chapter 3

# State Estimation and Kalman Filtering

The general formulation of the orbit determination problem includes the following well known relationships [12]:

$$\dot{\mathbf{X}} = F(\mathbf{X}, t), \qquad \mathbf{X}\left(t_k\right) \equiv \mathbf{X_k} \tag{3.1}$$

$$\mathbf{Y_k} = G(\mathbf{X}_k, t_k) + \epsilon_k; \qquad k = 1, ..., m \tag{3.2}$$

where Equation 3.1 represents an $n$-dimensional system of differential equations, $\dot{\mathbf{X}}$, as a nonlinear function, $F$, of the states, $\mathbf{X}$, and time, $t$, and Equation 3.2 a measurement model, $\mathbf{Y}_k$, with each entry as a nonlinear function, $G$, of the epoch states, $\mathbf{X}(t_k) \equiv \mathbf{X}_k$, the epoch time, $t_k$, and an additive residual at the epoch time, $\epsilon_i$, for a number of measurements, $m$.

The orbit determination is clearly a nonlinear estimation problem; however, Tapley [12] shows that if a reference trajectory which remains sufficiently close to the true trajectory can be determined, the trajectory can be linearized by using a Taylor series expansion about the reference trajectory [12], $\mathbf{X}^*$. This is an important step that will allow the application of linear theory.

## 3.1 Linearization

The following linearization is provided by Tapley [12]. The state deviation, $\mathbf{x}(t)$, the difference between the true trajectory, $\mathbf{X}$ and reference trajectory, $\mathbf{X}^*$, is given in Equation 3.3. The observation residual, $\mathbf{y}(t)$, the difference between the observation and expected observation, is given in Equation 3.4.

$$\mathbf{x}(t) = \mathbf{X}(t) - \mathbf{X}^*(t) \tag{3.3}$$

$$\mathbf{y}(t) = \mathbf{Y}(t) - \mathbf{Y}^*(t) \tag{3.4}$$

The derivative of the state deviation, $\dot{\mathbf{x}}(t)$, will be useful in the linearization process, and is given in Equation 3.5.

$$\dot{\mathbf{x}}(t) = \dot{\mathbf{X}}(t) - \dot{\mathbf{X}}^*(t) \tag{3.5}$$

The Taylor series expansion of Equation 3.1 and Equation 3.2 are given in Equation 3.6 and Equation 3.7 respectively where $[\ ]^*$ indicates that the partial derivative is evaluated at the reference solution, and $O_F$ and $O_G$ are orders of magnitude of the higher order terms in the expansion that will be ignored due to their small magnitudes.

$$\dot{\mathbf{X}}(t) = F(\mathbf{X}, t) = F(\mathbf{X}^*, t) + \left[\frac{\partial F(t)}{\partial \mathbf{X}(t)}\right]^* [\mathbf{X}(t) - \mathbf{X}^*(t)] + O_F[\mathbf{X}(t) - \mathbf{X}^*(t)]^2 \tag{3.6}$$

$$\mathbf{Y_k} = G(\mathbf{X}_k, t_k) + \epsilon_k = G(\mathbf{X}_k^*, t_k) + \left[\frac{\partial G}{\partial \mathbf{X}}\right]_k^* [\mathbf{X}(t_k) - \mathbf{X}_k^*(t)]_k + O_G[\mathbf{X}_k(t) - \mathbf{X}_k^*(t)]^2 + \epsilon_k \tag{3.7}$$

Using the conditions $\dot{\mathbf{X}}^* = F(\mathbf{X}^*, t)$ and $\mathbf{Y}_k^* = G(\mathbf{X}_k^*, t_k)$, Equation 3.6 and Equation 3.7 can be written as Equation 3.10 and Equation 3.11 where the definitions of $\mathbf{A}(t)$ and $\mathbf{H}_k$ are given below in Equation 3.8 and Equation 3.9 respectively.

$$\mathbf{A}(t) = \left[\frac{\partial F(t)}{\partial \mathbf{X}(t)}\right]^* \tag{3.8}$$

$$\mathbf{H}_k = \left[\frac{\partial G}{\partial \mathbf{X}}\right]_k^* \tag{3.9}$$

$$\dot{\mathbf{x}}(t) = \mathbf{A}(\mathbf{t})\mathbf{x}(t) \tag{3.10}$$

$$y_k = \mathbf{H}_k\mathbf{x}_k + \epsilon_k; \qquad k = 1, ..., m \tag{3.11}$$

## 3.2 Kalman Filter

The sequential estimation algorithm, often called the Kalman Filter, processes measurements individually as they are received. From Tapley [12], the Kalman filter equations are given in Equation 3.12, Equation 3.13, and Equation 3.14. These equations assume that the propagated state vector, $\hat{\mathbf{x}}_k^-$, propagated covariance matrix, $\mathbf{P}_k^-$, current observation, $Y_k$, and current observation covariance, $\mathbf{R_k}$ are known.

$$\mathbf{K}_k = \mathbf{P}_k^-\mathbf{H}_k^T\left[\mathbf{H}_k\mathbf{P}_k^-\mathbf{H}_k^T + \mathbf{R_k}\right]^{-1} \tag{3.12}$$

$$\hat{\mathbf{x}}_k^+ = \hat{\mathbf{x}}_k^- + \mathbf{K}_k\left[Y_k - \mathbf{H}_k\hat{\mathbf{x}}_k^-\right] \tag{3.13}$$

$$\mathbf{P}_k^+ = \left[\mathbf{I} - \mathbf{K}_k\mathbf{H}_k\right]\mathbf{P}_k^- \tag{3.14}$$

### 3.2.1 Extended Kalman Filter

Large deviations from the reference trajectory can cause filter divergence. The Kalman Filter performs an update to the reference trajectory only after all observations have been

processed, regardless of processing each measurement individually. In constrast, the Extended Kalman Filter performs an update to the reference trajectory after each measurement has been processed.

The following algorithm is provided by Tapley [12].

1. Integrate from $t_{k-1}$ to $t_k$ using the dynamical model

$$\hat{\mathbf{x}}_{\mathbf{k-1}}^{+} \rightarrow \hat{\mathbf{x}}_{\mathbf{k}}^{-} \tag{3.15}$$

$$\mathbf{P}_{\mathbf{k-1}}^{+} \rightarrow \mathbf{P}_{\mathbf{k}}^{-} \tag{3.16}$$

2. Compute the residual and $H_k$ matrix

$$\mathbf{y}_k = \mathbf{Y}_{\mathbf{k}} - G(\mathbf{X}_{\mathbf{k}}^{*}, t_k) \tag{3.17}$$

$$\mathbf{H}_k = \left.\frac{\partial \mathbf{G}}{\partial \mathbf{x}}\right|_{\hat{\mathbf{x}}_{k-1}^{+}} \tag{3.18}$$

3. Compute the Kalman gain

$$\mathbf{K_k} = \mathbf{P_k H_k^T} \left[\mathbf{H_k P_k H_k^T} + \mathbf{R_k}\right]^{-1} \tag{3.19}$$

4. Compute the updated state and covariance

$$\hat{\mathbf{x}}_k^{+} = \hat{\mathbf{x}}_k^{-} + \mathbf{K}_k \left[Y_k - \mathbf{H}_k \hat{\mathbf{x}}_k^{-}\right] \tag{3.20}$$

$$\mathbf{P}_{\mathbf{k}}^{+} = \left[\mathbf{I} - \mathbf{K_k H_k}\right] \mathbf{P}_{\mathbf{k}}^{-} \tag{3.21}$$

5. Update the reference trajectory to the current state estimate. If additional measurements exist go to 1, otherwise stop.

$$\hat{\mathbf{X}}^* = \hat{\mathbf{x}}_k^+ \tag{3.22}$$

### 3.2.2 Iterated Extended Kalman Filter

In order to help minimize linearization errors in highly nonlinear problems, higher order methods are often applied to a problem. In the linearization process used in Equation 3.6 and Equation 3.7, the measurement equation was expanded about the reference solution. With the use of the extended Kalman filter, the reference solution is updated by propagation, $\hat{\mathbf{x}}_{k-1}^+ \rightarrow \hat{\mathbf{x}}_k^-$, and processing of a measurement, $\hat{\mathbf{x}}_k^- \rightarrow \hat{\mathbf{x}}_k^+$, which is the step including the linearization about $\hat{\mathbf{x}}_k^-$. Since $\hat{\mathbf{x}}_k^+$ represents the best estimate of the state $\mathbf{x}_k$ after the measurement is processed, the measurement equation could be re-linearized about this new best estimate of the state to obtain a more accurate solution through as many iterations as are desired.

The application of higher order filters carries the weight of additional computational cost. In 1974, Gelb includes the iterated extended Kalman filter in his book with emphasis on "computation time required to mechanize the filter [13]." Jazwinski shows the IEKF converges more quickly to the exact solution than the EKF; however,he notes that the EKF will converge to the exact solution given enough measurements [14]. The solutions of both filters are subject to changes in the *a priori* covariance matrix, measurement covariance, and availability of measurements. As the *a priori* covariance matrix grows, measurement covariance decreases, and number of measurements decreases, the performance IEKF is superior to the EKF [14].

This derivation of the iterated extended Kalman filter algorithm is summarized from Simon [15].

IEKF Algorithm

1. Initialize the IEKF to the EKF estimate

$$\hat{\mathbf{x}}_{k,0}^{+} = \hat{\mathbf{x}}_{k}^{+} \tag{3.23}$$

$$\mathbf{P}_{k,0}^{+} = \mathbf{P}_{k}^{+} \tag{3.24}$$

2. Expanding the measurement equation around $\hat{\mathbf{x}}_{k,i-1}^{+}$ yields Equation 3.26.

$$\mathbf{H}_{k,i} = \left.\frac{\partial \mathbf{G}}{\partial \mathbf{x}}\right|_{\hat{\mathbf{x}}_{k,i-1}^{+}} \tag{3.25}$$

$$\mathbf{y}_{k,i} = \mathbf{Y}_{k} - \mathbf{G}(\mathbf{x}_{k,i-1}^{+}, t_k) \tag{3.26}$$

3. Calculate the Kalman gain, $\mathbf{K}_{k,i}$ for the current iteration.

$$\mathbf{K}_{k,i} = \mathbf{P}_{k}^{-}\mathbf{H}_{k,i}^{T}[\mathbf{H}_{k,i}\mathbf{P}_{k}^{-}\mathbf{H}_{k,i}^{T} + \mathbf{R}_{\mathbf{k}}]^{-1} \tag{3.27}$$

4. Calculate the covariance matrix, $\mathbf{P}$, and the new best estimate of the state, $\mathbf{x}_{k,i+1}^{+}$, for the current iteration.

$$\mathbf{P}_{k,i}^{+} = (\mathbf{I} - \mathbf{K}_{k,i}\mathbf{H}_{k,i})\mathbf{P}_{k}^{-} \tag{3.28}$$

$$\hat{\mathbf{x}}_{k,i}^{+} = \hat{\mathbf{x}}_{k}^{+} + \mathbf{K}_{k,i}[\mathbf{y}_{k,i} - \mathbf{H}_{k,i}(\hat{\mathbf{x}}_{k}^{+} - \hat{\mathbf{x}}_{k,i-1}^{+})] \tag{3.29}$$

5. Check for convergence. If convergence criterion not met, initialize the next iteration and goto 2, otherwise stop.

$$\hat{\mathbf{x}}_{k,i+1}^{+} = \hat{\mathbf{x}}_{k,i}^{+} \tag{3.30}$$

$$\mathbf{P}_{k,i+1}^{+} = \mathbf{P}_{k,i}^{+} \tag{3.31}$$

# Chapter 4

# Simulation

A simulation was constructed to compare the performance of the EKF and IEKF in the orbit determination scenario involving poor *apriori* information and intermittent observation data for a piece of space debris. The simulation consisted of multiple functions and programs to construct the orbit determination problem, and will be discussed in this chapter. The initial conditions and statistical data, which vary for most test cases, will also be presented.

## 4.1 Baseline Initial Conditions

The initial conditions chosen for the baseline case included an eccentricity and inclination similar to the International Space Station, and are presented in Table 4.1. This orbit was an important candidate for testing due to the future traffic and amount of debris existing at that altitude.

Table 4.1: Baseline Initial Conditions

| Orbital Elements | Value |
|---|---|
| Perigee Altitude (m) | 375134.9875 |
| Apogee Altitude (m) | 400249.8545 |
| Inclination Angle (degrees) | 51.6164 |
| Longitude of Ascending Node (degrees) | 270.1324 |
| Argument of Periapsis (degrees) | 0.0135 |
| True Anomaly (degrees) | 0.0297 |

The true initial state is given in Equation 4.1. The initial standard deviations, shown in Equation 4.2, were chosen based on the results by Kelso [16] for approximately 5 days

of propagation error of a TLE dataset. From these data, the initial covariance matrix in Equation 4.3 was chosen, where $\sigma_r$ is the covariance of the position and $\sigma_v$ is the covariance of the velocity.

$$\begin{bmatrix} X \\ Y \\ Z \\ V_x \\ V_y \\ V_z \end{bmatrix} = \begin{bmatrix} 165109.2914 & m \\ -6748615.7425 & m \\ 188744.0459 & m \\ 4771.0926 & m/s \\ 284.9491 & m/s \\ 6023.9774 & m/s \end{bmatrix} \tag{4.1}$$

$$\begin{aligned} \sigma_r &= 2500\, m \\ \sigma_v &= 10\, m/s \end{aligned} \tag{4.2}$$

$$P_0 = \begin{bmatrix} \sigma_{r_x}^2 & 0 & 0 & 0 & 0 & 0 \\ 0 & \sigma_{r_y}^2 & 0 & 0 & 0 & 0 \\ 0 & 0 & \sigma_{r_z}^2 & 0 & 0 & 0 \\ 0 & 0 & 0 & \sigma_{v_x}^2 & 0 & 0 \\ 0 & 0 & 0 & 0 & \sigma_{v_y}^2 & 0 \\ 0 & 0 & 0 & 0 & 0 & \sigma_{v_z}^2 \end{bmatrix} = \begin{bmatrix} 2500^2 & 0 & 0 & 0 & 0 & 0 \\ 0 & 2500^2 & 0 & 0 & 0 & 0 \\ 0 & 0 & 2500^2 & 0 & 0 & 0 \\ 0 & 0 & 0 & 10^2 & 0 & 0 \\ 0 & 0 & 0 & 0 & 10^2 & 0 \\ 0 & 0 & 0 & 0 & 0 & 10^2 \end{bmatrix} \tag{4.3}$$

## 4.2 Test Cases

In order to properly compare the performance of the EKF and IEKF, multiple sets of initial conditions and observational data were evaluated. The altitude, inclination, longitude

of the ascending node, argument of periapsis, and true anomaly were altered individually for each case.

A summary of non-baseline cases can be found in Table 4.2, which are listed by how each case differs from the baseline case.

Table 4.2: Variations from Baseline Case

| Case Number | Variation of | Value of Varied Terms |
|---|---|---|
| 2 | Altitude | $r_a = 500km$ and $r_p = 700km$ |
| 3 | Altitude | $r_a = 800km$ and $r_p = 1000km$ |
| 4 | Inclination | $i = 28.5°$ |
| 5 | Inclination | $i = 75°$ |
| 6 | Longitude of the Ascending Node | $\Omega = 45°$ |
| 7 | Longitude of the Ascending Node | $\Omega = 90°$ |
| 8 | Argument of Periapsis | $\omega = 45°$ |
| 9 | Argument of Periapsis | $\omega = 90°$ |
| 10 | True Anomaly | $\nu = 90°$ |
| 11 | True Anomaly | $\nu = 270°$ |

## 4.3 Constants

Many constants are used when performing orbit determination. For completeness, Table 4.3 lists the values of each constant used in this simulation.

Table 4.3: Constants

| |
|---|
| $\mu = 3.9860044150 * 10^{14} \ \frac{m^3}{s^2}$ |
| $J_2 = 0.1082635666 * 10^{-2}$ |
| $\omega_e = 7.2921156001 * 10^{-5} \ \frac{rad}{s}$ |
| $r_e = 6378.13630 \ km$ |

## 4.4 Dynamical Model

The dynamical model represents the equations of motion of the object, and is used to propagate the state, Equation 4.4, forward through time. The dynamical model in this simulation used Equation 2.10 to form the derivatives of the states, which are given in Equation 4.5. This equation includes accelerations due to two-body motion and the $J_2$ oblateness perturbation effects.

$$\mathbf{X} = \begin{bmatrix} r_x \\ r_y \\ r_z \\ v_x \\ v_y \\ v_z \end{bmatrix} = \begin{bmatrix} X_1 \\ X_2 \\ X_3 \\ X_4 \\ X_5 \\ X_6 \end{bmatrix} \tag{4.4}$$

$$\dot{\mathbf{X}} = \begin{bmatrix} v_x \\ v_y \\ v_z \\ a_x \\ a_y \\ a_z \end{bmatrix} = \begin{bmatrix} X_4 \\ X_5 \\ X_6 \\ \frac{-\mu X_1 r^4 + \frac{3}{2}\mu J_2 r_e^2 X_1 \left(5X_3^2 - r^2\right)}{r^7} \\ \frac{-\mu X_2 r^4 + \frac{3}{2}\mu J_2 r_e^2 X_2 \left(5X_3^2 - r^2\right)}{r^7} \\ \frac{-\mu X_3 r^4 + \frac{3}{2}\mu J_2 r_e^2 X_3 \left(5X_3^2 - 3r^2\right)}{r^7} \end{bmatrix} \tag{4.5}$$

## 4.5 Measurement Model

The measurement consists of the equations for each measurement type. For this simulation, range-only measurements, $Y_R$, were used, and are represented in Equation 4.6, where $X_S$, $Y_S$, and $Z_S$ are the ECEF coordinates of the tracking station and $X_E$, $Y_E$, and $Z_E$ are the ECEF coordinates of the object. Equation 4.7 is used to transform the ECEF coordinates into the ECI coordinates of the model, which are also the first three entries in the ECI

state vector. Substituting this result into Equation 4.6 yields Equation 4.8, the measurement model in ECI coordinates.

$$Y_R = \left[(X_E - X_S)^2 + (Y_E - Y_S)^2 + (Z_E - Z_S)^2\right]^{\frac{1}{2}} \tag{4.6}$$

$$\begin{bmatrix} X_E \\ Y_E \\ Z_E \end{bmatrix} = \begin{bmatrix} cos(\theta) & sin(\theta) & 0 \\ -sin(\theta) & cos(\theta) & 0 \\ 0 & 0 & 1 \end{bmatrix} \begin{bmatrix} X_1 \\ X_2 \\ X_3 \end{bmatrix} \tag{4.7}$$

$$Y_R = \left[(X_1 cos(\theta) + X_2 sin(\theta) - X_S)^2 + (-X_1 sin(\theta) + X_2 cos(\theta) - Y_S)^2 + (X_3 - Z_S)^2\right]^{\frac{1}{2}} \tag{4.8}$$

## 4.6 Tracking Station Network

The tracking stations used to generate experimental data in the simulation were taken from Vallado [17]. The sites used represent actual tracking stations that are a part of the US Space Surveillance Network, and are represented in Table 4.4. This network consists of mainly northern and western hemisphere stations, which lead to large gaps in the measurement data.

To simplify the tracking network, the data in Table 4.5 was implemented. A maximum range of 5,000 $km$ was chosen to ensure range would not prevent the data generator from producing measurements as the maximum range generated is on the order of 1,000 $km$. To mitigate errors associated with sensing near the horizon, the minimum elevation angle required to take a measurement was established at 20 degrees, which Vallado suggests for optical sensors [17]. The sensors were assumed to have no mechanical, geographical, or political constraints that could limit the azimuth. The range noise and bias were assumed to be 5 $m$ and 0 $m$ respectively.

Table 4.4: Tracking Station Coordinates (Geodetic C.S.)

| Site | Latitude(degrees) | Longitude(degrees) | Altitude(meters) |
|---|---|---|---|
| Flyingdales, UK | 54.37 | -0.67 | 338.9 |
| Ascension, Atlantic | -7.91 | -14.40 | 56.1 |
| Clear, AK | 64.29 | -149.19 | 213.3 |
| Antigua, West Indies | 17.14 | -61.79 | 0.5 |
| Cape Cod, MA | 41.75 | -70.54 | 80.3 |
| Beale, CA | 39.14 | -121.35 | 115.7 |
| Shemya, AK | 52.74 | -174.09 | 89.8 |
| Thule, Greenland | 76.57 | -68.30 | 424.7 |
| Cavalier, ND | 48.72 | -97.90 | 347.3 |
| Kaena Point, HI | 21.57 | -158.27 | 300.2 |
| Kwajalein Atoll, Pacific Ocean | 9.39 | 167.48 | 62.7 |
| Diego-Garcia, Indian Ocean | -7.41 | 72.45 | -61.2 |
| Moron (MOSS), Spain | 37.10 | -5.37 | 287.0 |
| Eglin, FL | 30.57 | -86.21 | 34.7 |
| Socorro, NM | 33.82 | -106.66 | 1510.2 |
| Globus II, Norway | 70.37 | 31.13 | 1.2 |

Table 4.5: Tracking Station Configuration Information

| | |
|---|---|
| Maximum Range | 5000 $km$ |
| Minimum Elevation | 20° |
| Maximum Elevation | 90° |
| Minimum Azimuth | 0 ° |
| Maximum Azimuth | 360° |
| Range Noise | 5 $m$ |
| Range Bias | 0 $m$ |

The simulated measurements were generated with an assumed maximum range and minimum elevation angle from the tracking station to maintain a sense of realism, as well as to add measurement outages.

The measurement rate was limited to the integration rate of 15 seconds.

The measurements were assumed to originate from tracking stations with zero bias, and 5 $m$ noise in range.

To simulate a debris object for which tracking data is available, the initial estimate of the state of the debris being tracked was obtained from a simulated two-line element (TLE) data set on the order of two to five days old. This method generated a large *apriori* covariance matrix with which to begin the estimation process.

## 4.7 Propagator

The propagation method chosen for this study was a fourth order Runge-Kutta. The Runge-Kutta offers increased accuracy over the basic Euler method by calculating additional interior points along the path from beginning of the step, $t_0$, to the end of the step, $t_0 + \Delta t$. The fourth order Runge-Kutta is widely documented, and can be found below in Equation 4.9 through Equation 4.13 [10].

$$k_1 = \mathbf{f}\left(\mathbf{X}(t_0), t_0\right) \tag{4.9}$$

$$k_2 = \mathbf{f}\left(\mathbf{X}(t_0) + \frac{\Delta t}{2} k_1, t_0 + \frac{\Delta t}{2}\right) \tag{4.10}$$

$$k_3 = \mathbf{f}\left(\mathbf{X}(t_0) + \frac{\Delta t}{2} k_2, t_0 + \frac{\Delta t}{2}\right) \tag{4.11}$$

$$k_4 = \mathbf{f}\left(\mathbf{X}(t_0) + \Delta t\ k_3, t_0 + \frac{\Delta t}{2}\right) \tag{4.12}$$

$$\mathbf{X}(t_o + \Delta t) = \frac{\Delta t}{6}\left(k_1 + 2k_2 + 2k_3 + k_4\right) \tag{4.13}$$

## 4.8 Procedure

For each case, a set of initial conditions was defined. Those initial conditions were used with the dynamics model, measurement model, ground station data, propagator, and data generator to generate a set of data for that specific case. The generated data was then used with the dynamics model, measurement mode, propagator, EKF algorithm, IEKF algorithm, and a post processing script to generate MATLAB plots and data of the performance of each filter. This data will be presented in the next chapter.

# Chapter 5

# Results

## 5.1 Measure of Solution Accuracy

The vectors $\alpha$ and $\beta$ represent the difference in the best estimate of the state given by EKF, $\hat{\mathbf{x}}_{EKF}$, and IEKF, $\hat{\mathbf{x}}_{IEKF}$, respectively and the true solution, $\mathbf{x_{True}}$.

$$\alpha = |\hat{\mathbf{x}}_{EKF} - \mathbf{x}_{True}|$$

$$\beta = |\hat{\mathbf{x}}_{IEKF} - \mathbf{x}_{True}|$$

The normalised mean squared error (NMSE), given by Equation 5.1, will be used to define a performance parameter, $\eta$, which is given in Equation 5.2. By definition, if $\eta > 0$ the IEKF solution is more accurate; however, if $\eta < 0$ the EKF solution is more accurate.

$$\Delta_n = \left[ \sum_{i=1}^{n} \frac{(\hat{\mathbf{x}}_i - \mathbf{x}_i)^2}{\hat{\mathbf{x}}_i} \right]^{\frac{1}{2}} \tag{5.1}$$

$$\eta = \frac{\Delta_{n,EKF}}{\Delta_{n,IEKF}} - 1 \tag{5.2}$$

## 5.2 Baseline Case

The baseline case consisted of 325 observations spanning 8 batches and 12,915 seconds, of which details can be found in Table 5.1. The largest outage occurs between batch 6 and batch 7, and lasts for 4490 seconds, which is approximately 80% of an orbit. The orbital

parameters for this case can be found in Table 5.2, and represent an orbit similar to that of the ISS.

Table 5.1: Baseline: Outage Details

| | Batch Number | | | | | | | |
|---|---|---|---|---|---|---|---|---|
| | 1 | 2 | 3 | 4 | 5 | 6 | 7 | 8 |
| First Measurement No. | 1 | 46 | 92 | 115 | 161 | 211 | 259 | 292 |
| Last Measurement No. | 45 | 91 | 114 | 160 | 210 | 258 | 291 | 325 |
| Start Time ($s$) | 320 | 1195 | 1580 | 5590 | 6960 | 7290 | 12015 | 12750 |
| End Time ($s$) | 540 | 1420 | 1690 | 5815 | 7205 | 7525 | 12175 | 12915 |
| Outage Before Batch ($s$) | 320 | 655 | 160 | 3900 | 1145 | 85 | 4490 | 575 |

Table 5.2: Baseline: Orbit Parameters

| Orbital Elements | Value |
|---|---|
| Perigee Altitude (m) | 375134.9875 |
| Apogee Altitude (m) | 400249.8545 |
| Inclination Angle (degrees) | 51.6164 |
| Longitude of Ascending Node (degrees) | 270.1324 |
| Argument of Periapsis (degrees) | 0.0135 |
| True Anomaly (degrees) | 0.0297 |

The residuals, the difference between the observation and the expected observation, for the full set of data are shown in Figure 5.1. The residuals for both the EKF and IEKF remain small for the entire simulation; however, the residuals for the IEKF remain closer to zero than those of the EKF. This can be attributed to the re-linearization of the observation model that is carried out multiple times for each observation in the IEKF. This trend will remain present in the analysis of each case.

To allow closer inspection, Figure 5.2 and Figure 5.3 show the residuals for batch 6 and batch 7 respectively. Batch 6 consisted of 47 measurements spanning 235 seconds, while batch 7 consisted of 32 measurements spanning 160 seconds. Due to the very small residual prior to the outage, the residual does not grow significantly in either filter between the final

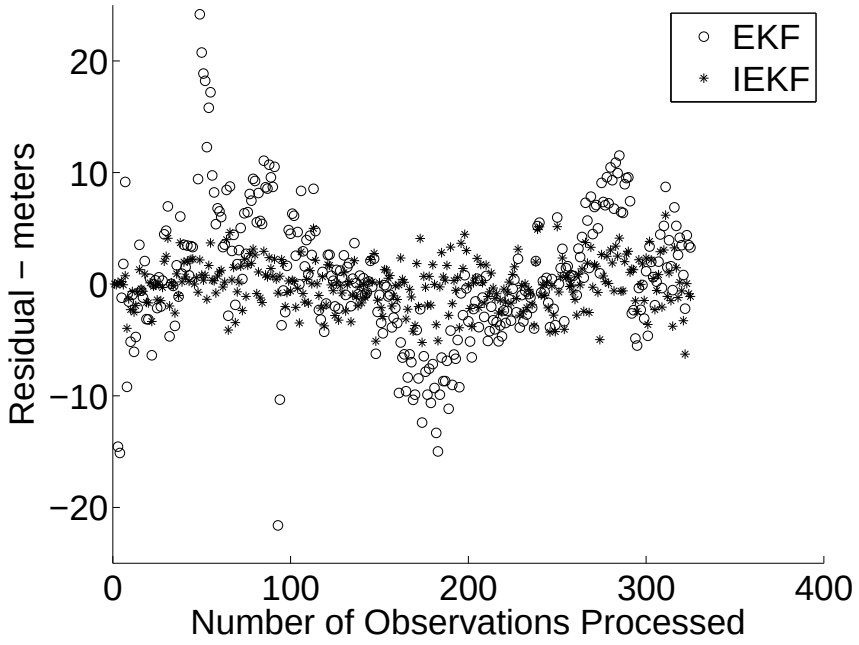


Figure 5.1: Baseline: Residuals vs. Number of Observations Processed

measurement in batch 6 to the first measurement in batch 7. The IEKF residuals for batch 7, Figure 5.3, remain clearly smaller than those for the EKF.

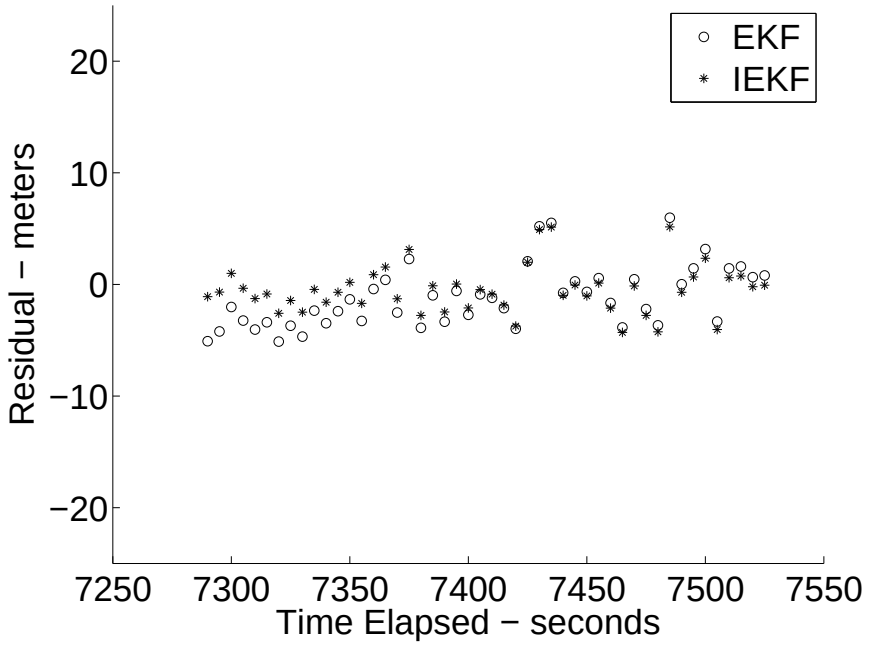


Figure 5.2: Baseline: Residuals for Batch #6

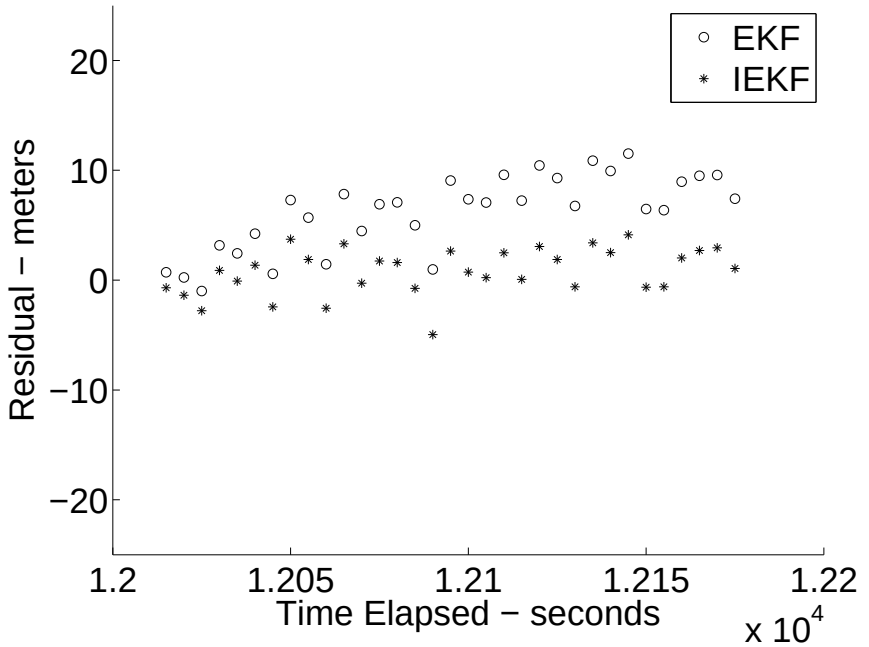


Figure 5.3: Baseline: Residuals for Batch #7

The performance parameter, $\eta$, shown in Figure 5.4, remains above the reference zero line for the entire simulation. This serves as a quick reference that the IEKF produced more accurate estimates of the true state than the EKF.

The NMSE values for batch 6 and 7 are shown together in Figure 5.5. The NMSE values for batch 6 and batch 7 individually are shown in Figure 5.6 and Figure 5.7 respectively. It should be noted that the y-axis scale of these two figures are equal, which allows a direct comparison. The NMSE of the EKF grows approximately 60% during the outage, while the NMSE of the IEKF grows approximately 30%. This growth from an outage is expected; however, the IEKF recovers to a lower value faster than the EKF.

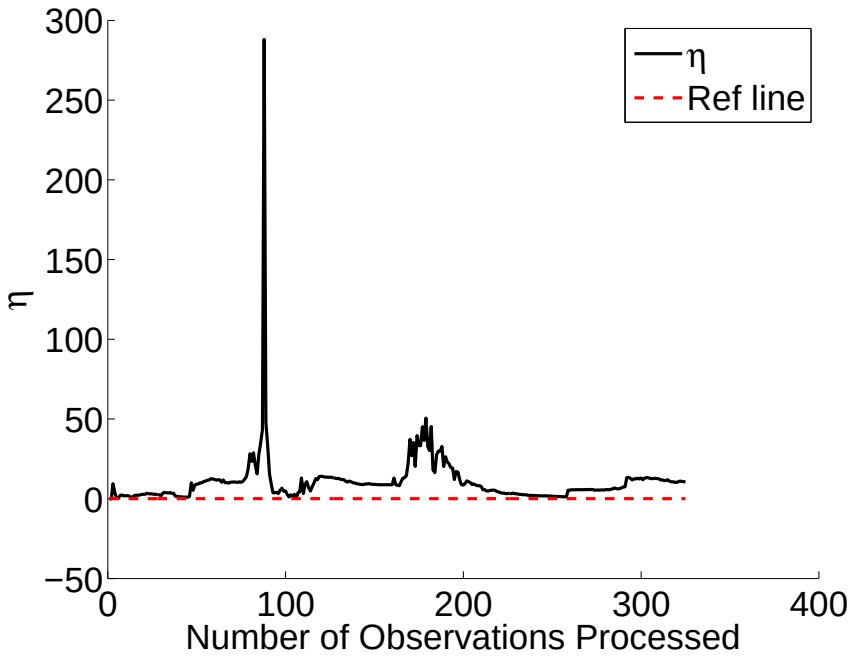


Figure 5.4: Baseline: $\eta$ vs. Number of Observations Processed

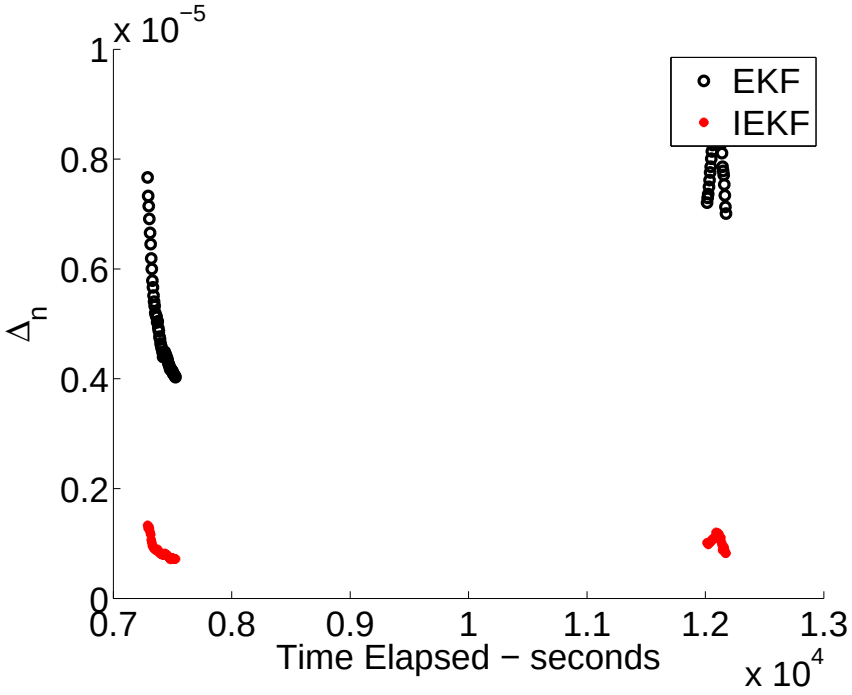


Figure 5.5: Baseline: NMSE for Batch #6 and Batch #7

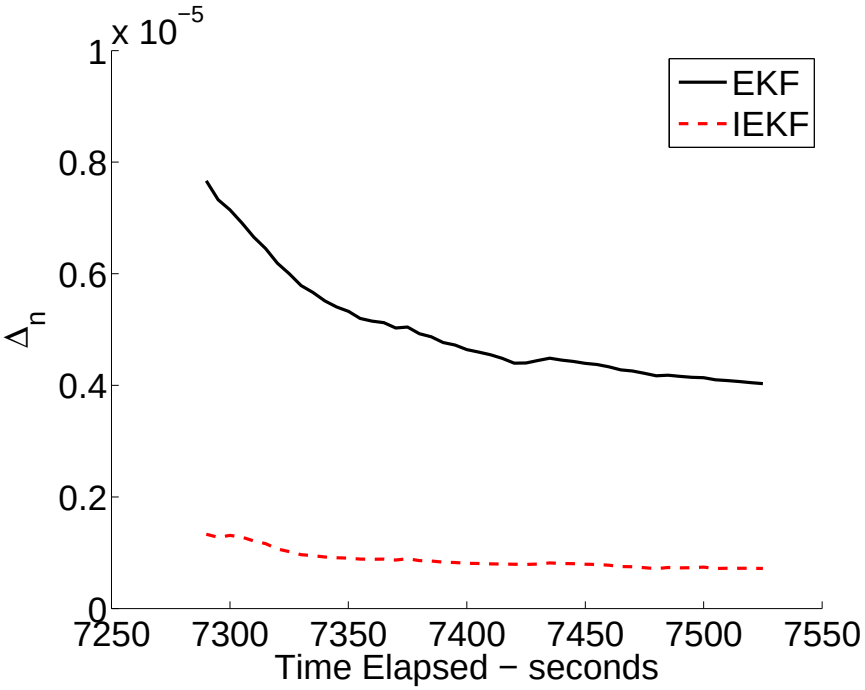


Figure 5.6: Baseline: NMSE for Batch #6

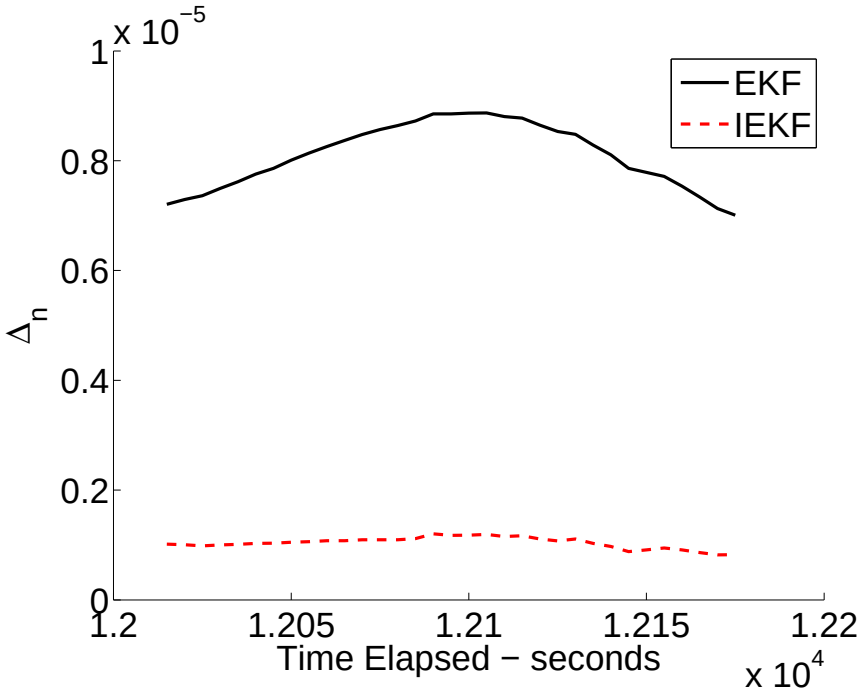


Figure 5.7: Baseline: NMSE for Batch #7

The performance of the filters was evaluated specifically for batch 6 and batch 7. Table 5.3 contains data concerning the state, residual, and NMSE for both filters. For batch 6, the $\alpha$ and $\beta$ performance values, which represent the difference in the estimated state and true state, remained small for both filters prior to the outage. The residuals of both filters were also small; however, the residual of the IEKF was approximately an order of magnitude smaller than that of the EKF.

Following the outage, and processing of batch 7, both residuals have increased. The NMSE of the IEKF also remained smaller than that of the EKF. This is due again to the IEKF processing an observation more than once, which leads to an artifically larger set of observations for the IEKF.

Table 5.3: Baseline: Output Before/After Largest Outage

| | End of Batch #6 | | End of Batch #7 | |
|---|---|---|---|---|
| State | $\alpha$ (EKF) | $\beta$ (IEKF) | $\alpha$ (EKF) | $\beta$ (IEKF) |
| X(m) | 0.7734 | 0.7548 | 5.0188 | 0.9288 |
| Y(m) | 0.5084 | 0.1123 | 6.4405 | 0.5038 |
| Z(m) | 2.7568 | 1.1256 | 3.8424 | 0.1541 |
| Vx(m/s) | 0.0115 | 0.0005 | 0.0065 | 0.0007 |
| Vy(m/s) | 0.0006 | 0.0001 | 0.0034 | 0.0003 |
| Vz(m/s) | 0.0061 | 0.0023 | 0.0043 | 0.0006 |
| yk(m) | 0.7927 | 0.0794 | 7.4162 | 1.0580 |
| NMSE | 4.0298E-006 | 7.1876E-007 | 7.0072E-006 | 8.2265E-007 |

After batch 8 has been processed, all data has been consumed. The performance values can be found in Table 5.4. Given additional observations, the accuracy of the EKF improved, which can be seen by the reduction in size of the residual and NMSE values when compared to Table 5.3.

Table 5.4: Baseline: All Observations (325 observations - 12915 $s$)

| State | $\alpha$ (EKF) | $\beta$ (IEKF) |
|---|---|---|
| X(m) | 2.1986 | 0.1477 |
| Y(m) | 4.9208 | 0.4030 |
| Z(m) | 5.7930 | 0.5380 |
| Vx(m/s) | 0.0112 | 0.0007 |
| Vy(m/s) | 0.0028 | 0.0005 |
| Vz(m/s) | 0.0018 | 0.0012 |
| yk(m) | 3.2716 | 1.0989 |
| NMSE | 4.8866E-006 | 5.3018E-007 |

While the $\alpha$ and $\beta$ values for the EKF continue to remain small, the values for the position components are at least an order of magnitude larger than those of the IEKF. Combining this result with the smaller residual and smaller NMSE value, the IEKF produced a more accurate estimate of the state for the baseline case.

### 5.3 Inclination Variation Case $\rightarrow i = 75.0°$

The $i = 75.0°$ case consisted of 326 observations spanning 9 batches and 13,410 seconds, of which details can be found in Table 5.5. The largest outage occurs between batch 7 and batch 8, and lasts for 5895 seconds, which is approximately 105% of an orbit. This outage and the initial outage, the time before the beginning of batch 1, are approximately 30% larger than those specific outages for the baseline case. These outage increases are due to the finite number of ground stations modeled. The orbital parameters for this case can be found in Table 5.6. This case differs from the baseline case only by the inclination angle.

Table 5.5: $i = 75.0°$: Outage Details

| | Batch Number | | | | | | | | |
|---|---|---|---|---|---|---|---|---|---|
| | 1 | 2 | 3 | 4 | 5 | 6 | 7 | 8 | 9 |
| First Measurement No. | 1 | 22 | 71 | 117 | 153 | 183 | 202 | 232 | 279 |
| Last Measurement No. | 21 | 70 | 116 | 152 | 182 | 201 | 231 | 278 | 326 |
| Start Time ($s$) | 730 | 905 | 1330 | 2755 | 6330 | 6630 | 6970 | 13010 | 13410 |
| End Time ($s$) | 830 | 1145 | 1555 | 2930 | 6475 | 6720 | 7115 | 13240 | 13645 |
| Outage Before Batch ($s$) | 730 | 75 | 185 | 1200 | 3400 | 155 | 250 | 5895 | 170 |

Table 5.6: $i = 75.0°$: Orbit Parameters

| Orbital Elements | Value |
|---|---|
| Perigee Altitude (m) | 375134.9875 |
| Apogee Altitude (m) | 400249.8545 |
| Inclination Angle (degrees) | 75.121 |
| Longitude of Ascending Node (degrees) | 270.1324 |
| Argument of Periapsis (degrees) | 0.0135 |
| True Anomaly (degrees) | 0.0297 |

The residuals for the full set of data are shown in Figure 5.8. The IEKF residuals remain small, compared to the EKF residuals, for all observations; however, the EKF residuals grow to near 200 $m$ for some observations. The 30% increase in the initial outage coupled with the size of the first batch, 20 observations compared to 45 observations for the baseline case, leads the EKF to a less accurate estimate early in the simulation. For each batch of data, the residual of the EKF begins to shrink; however, this process is interrupted by multiple outages.

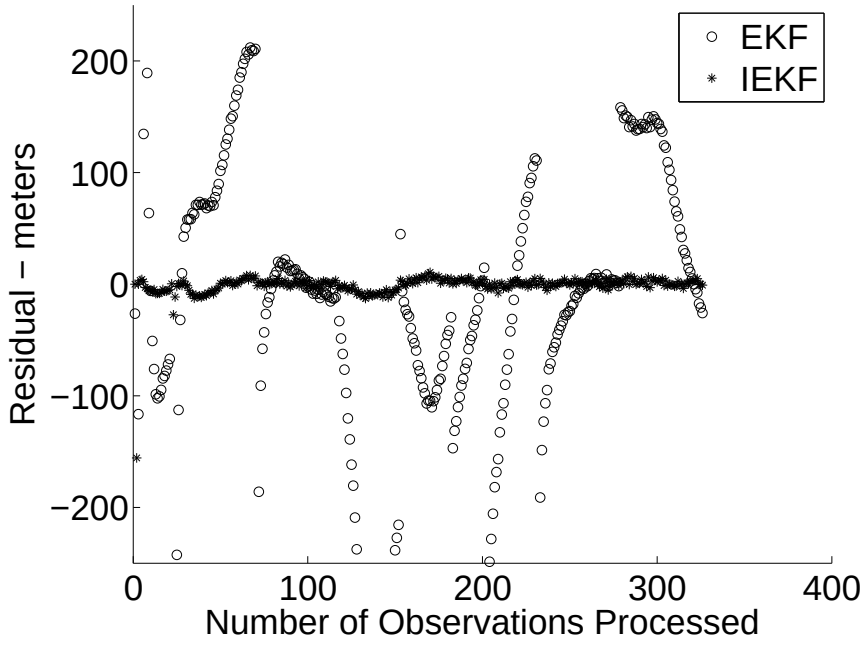


Figure 5.8: $i = 75°$ : Residuals vs. Number of Observations Processed

Figure 5.9 and Figure 5.10 show the residuals for batch 7 and batch 8 respectively. Batch 7 consisted of 29 measurements spanning 145 seconds, while batch 8 consisted of 46 measurements spanning 230 seconds. For batch 7, not enough observations existed to allow the EKF to attain an estimate as accurate as the IEKF. The residuals for the IEKF remained small for the entire batch. For batch 8, the EKF processed enough observations to appear to converge to an accurate estimate very close to that of the IEKF, which remained close to zero for the entire batch.

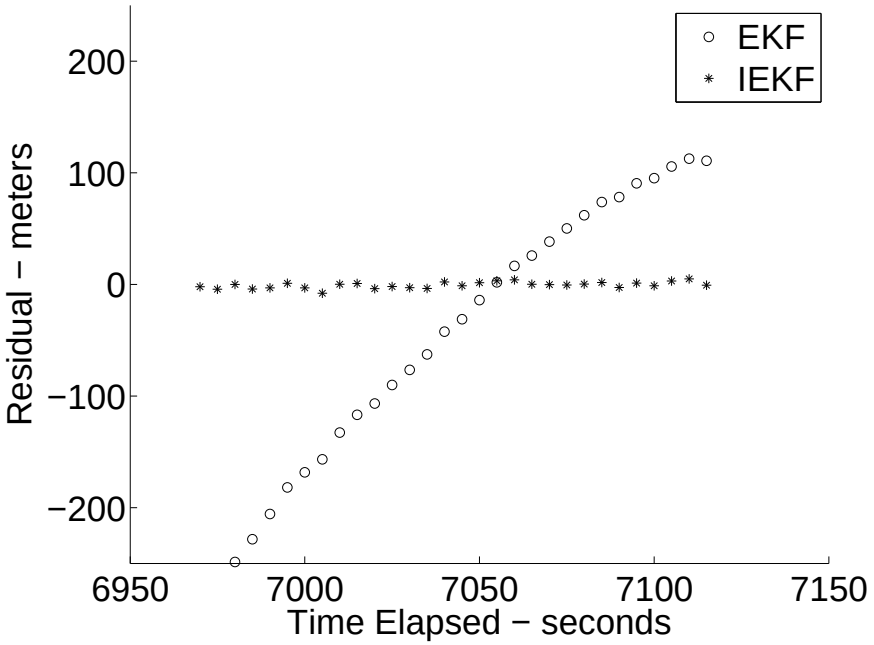


Figure 5.9: $i = 75°$ : Residuals for Batch #7

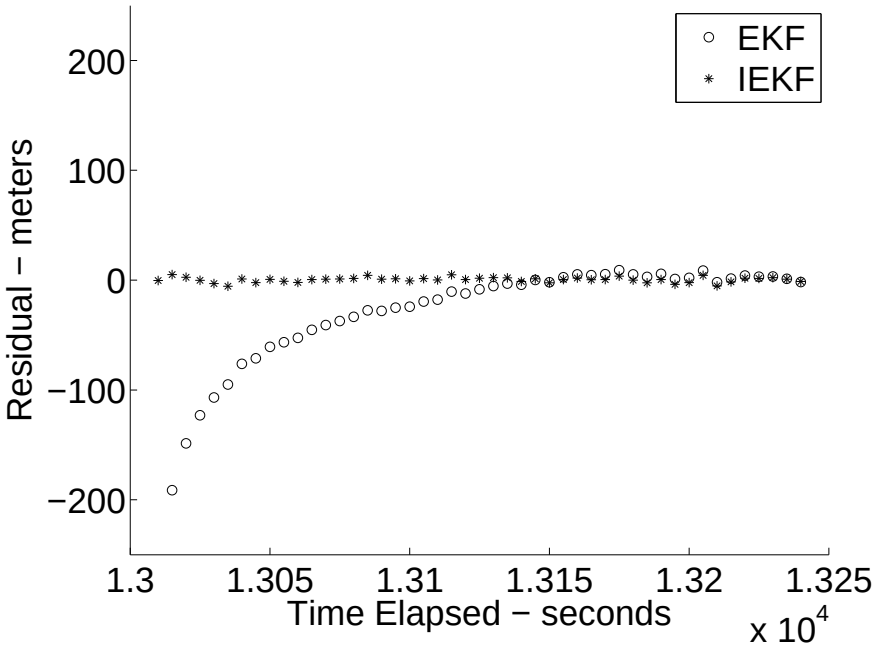


Figure 5.10: $i = 75°$ : Residuals for Batch #8

The performance parameter, $\eta$, shown in Figure 5.11, remains above the reference zero line for the entire simulation. This serves as a quick reference that the IEKF produced more accurate estimates of the true state than the EKF, which is the same result as the baseline case.

The NMSE values for batch 7 and 8 are shown together in Figure 5.12. The NMSE of the EKF begins and ends greater than the NMSE of the IEKF for both batches. The NMSE values for batch 7 and batch 8 individually are shown in Figure 5.13 and Figure 5.14 respectively. For batch 7, the NMSE steadily decreases as observations are processed. Similar to the residual, this trend would have continued given additional observations. For batch 8, the NMSE of the EKF remains much higher, although relatively constant, than the NMSE of the IEKF. This shows that the IEKF estimate of the state remains much closer to the true state than the EKF estimate.

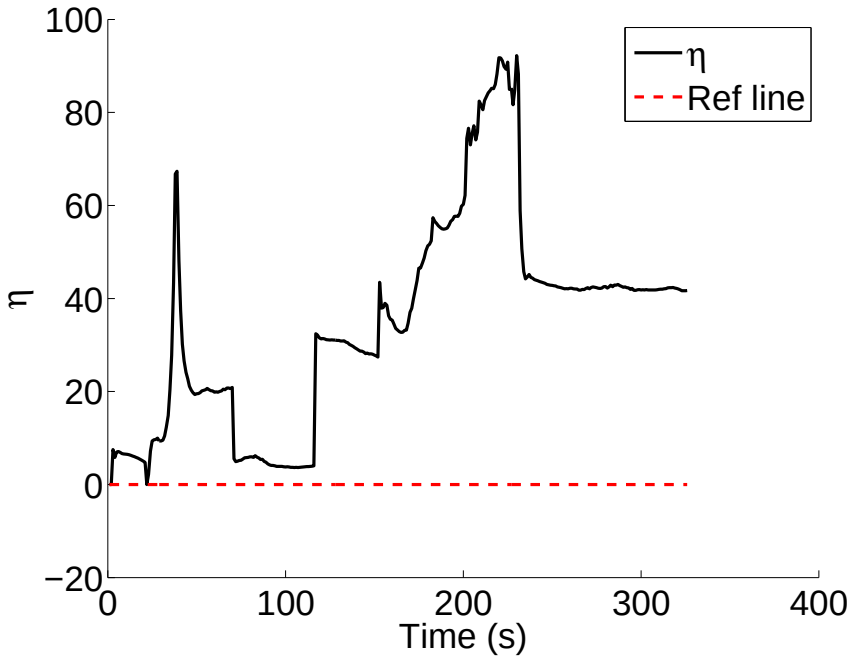


Figure 5.11: $i = 75° : \eta$ vs. Number of Observations Processed

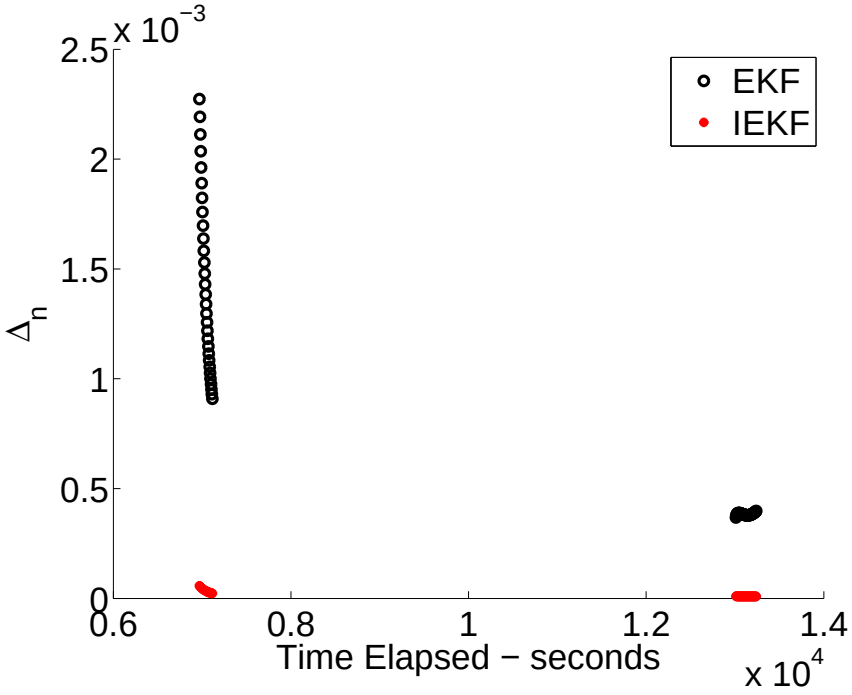


Figure 5.12: $i = 75°$ : NMSE for Batch #7 and Batch #8

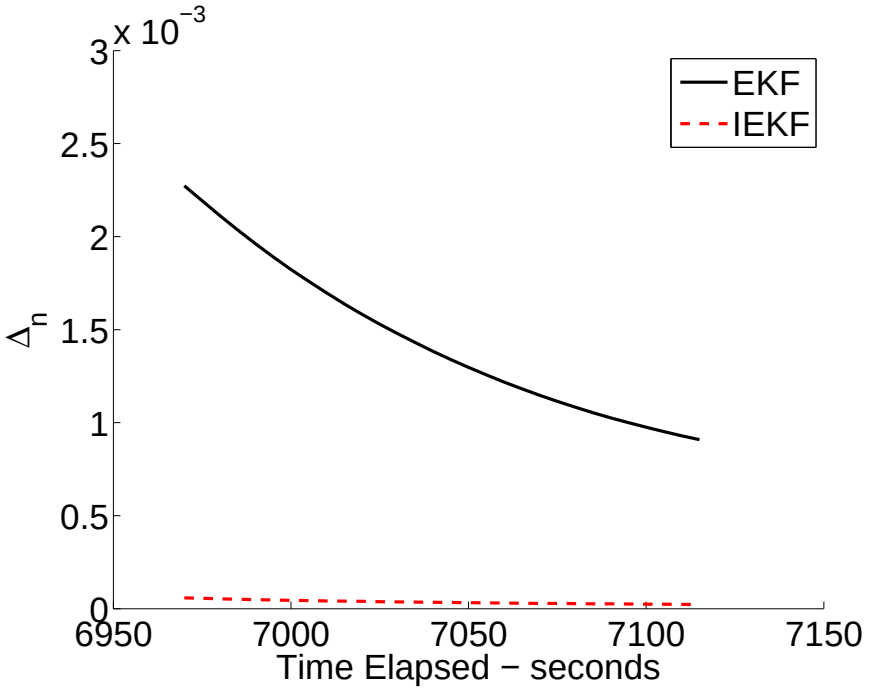


Figure 5.13: $i = 75°$ : NMSE for Batch #7

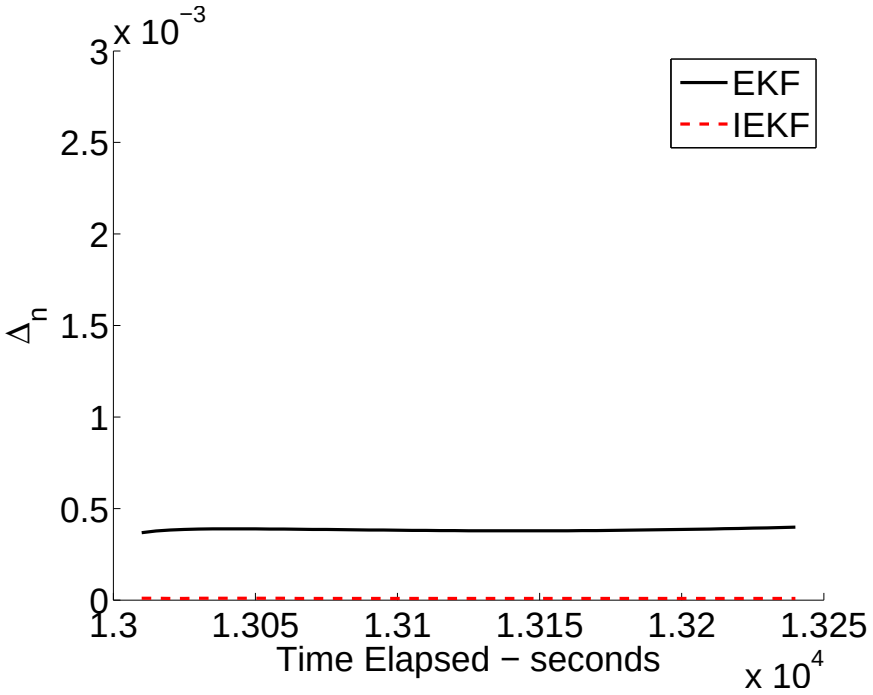


Figure 5.14: $i = 75°$ : NMSE for Batch #8

The performance of the filters was evaluated specifically for batch 7 and batch 8. Table 5.7 contains data concerning the state, residual, and NMSE for both filters. For batch 7 $\alpha$ and $\beta$ performance values remained approximately two orders of magnitude smaller for the IEKF than those of the EKF. This can be attributed to the high residual for the EKF at the end of batch 7. For batch 8 the residual for the EKF approaches a small number as seen in Figure 5.10. However, this low residual does not correspond with a low NMSE value. This is a representation of apparent divergence, which is convergence to the wrong value.

Table 5.7: $i = 75.0°$: Intermediate Output

| | End of Batch #7 | | End of Batch #8 | |
|---|---|---|---|---|
| State | $\alpha$ (EKF) | $\beta$ (IEKF) | $\alpha$ (EKF) | $\beta$ (IEKF) |
| X(m) | 32.0360 | 0.3094 | 317.7501 | 7.2187 |
| Y(m) | 175.8334 | 2.6102 | 109.3774 | 2.8083 |
| Z(m) | 207.6050 | 1.5862 | 48.3734 | 1.2793 |
| Vx(m/s) | 0.4586 | 0.0116 | 0.3879 | 0.0098 |
| Vy(m/s) | 0.2080 | 0.0023 | 0.3018 | 0.0040 |
| Vz(m/s) | 0.0540 | 0.0021 | 0.3622 | 0.0063 |
| yk(m) | 110.7678 | 0.8292 | 1.7156 | 1.1389 |
| NMSE | 9.0870E-004 | 2.2975E-005 | 3.9836E-004 | 9.3518E-006 |

After batch 9 has been processed, all data has been consumed. The performance values can be found in Table 5.8. Similar to the results shown in Table 5.7, the IEKF produced a more accurate estimate of the true state, as shown by the $\beta$ values being at least one order of magnitude smaller than the $\alpha$ values. The NMSE of the IEKF was approximately two orders of magnitude smaller than that of the EKF after processing all observations.

Table 5.8: $i = 75.0°$: Output for All Observations (326 - 13645 $s$) Processed

| State | $\alpha$ (EKF) | $\beta$ (IEKF) |
|---|---|---|
| X(m) | 399.6702 | 9.7243 |
| Y(m) | 234.1288 | 4.8175 |
| Z(m) | 92.1286 | 2.1426 |
| Vx(m/s) | 0.1945 | 0.0055 |
| Vy(m/s) | 0.4273 | 0.0073 |
| Vz(m/s) | 0.3399 | 0.0064 |
| yk(m) | 25.9034 | 0.8774 |
| NMSE | 1.2476E-003 | 2.9886E-005 |

## 5.4 Argument of Perigee Case $\rightarrow \omega = 90°$

The $\omega = 90°$ case consisted of 318 observations spanning 8 batches and 16,460 seconds, of which details can be found in Table 5.9. While the largest outage is smaller than the largest outage of the previous case ($i = 75.0°$), the initial outage is 4625 seconds. The poor *apriori* covariance matrix is propagated for 85% of an orbit before the first observation is processed. The orbital parameters for this case can be found in Table 5.10. This case differs from the baseline case only by the argument of periapsis.

Table 5.9: $\omega = 90°$: Outage Details

| | Batch Number | | | | | | | |
|---|---|---|---|---|---|---|---|---|
| | 1 | 2 | 3 | 4 | 5 | 6 | 7 | 8 |
| First Measurement No. | 1 | 49 | 97 | 133 | 161 | 208 | 222 | 270 |
| Last Measurement No. | 48 | 96 | 132 | 160 | 207 | 221 | 269 | 318 |
| Start Time ($s$) | 4625 | 4895 | 5660 | 7060 | 10235 | 10770 | 15915 | 16220 |
| End Time ($s$) | 4860 | 5130 | 5835 | 7195 | 10465 | 10835 | 16150 | 16460 |
| Outage Before Batch ($s$) | 4625 | 35 | 530 | 1225 | 3040 | 305 | 5080 | 70 |

Table 5.10: $\omega = 90°$: Orbit Parameters

| Orbital Elements | Value |
|---|---|
| Perigee Altitude (m) | 375134.9875 |
| Apogee Altitude (m) | 400249.8545 |
| Inclination Angle (degrees) | 51.6164 |
| Longitude of Ascending Node (degrees) | 270.1324 |
| Argument of Periapsis (degrees) | 90.1943 |
| True Anomaly (degrees) | 0.0297 |

The residuals for the full set of data are shown in Figure 5.15. The IEKF residual remains small for all observations; however, the EKF residual becomes large very quickly. The combination of very accurate measurements (5 $m$ measurement noise) and the large covariance matrix following the starting outage cause the EKF to diverge quickly. The accurate measurements cause the covariance matrix to approach zero before enough measurements are processed to allow for the filter to converge. The small covariance matrix forces the Kalman gain calculation to also be small. If the Kalman gain is small, the state update

will also be small, regardless of the size of the residual. Figure 5.16 and Figure 5.17 provide a closer look at the residuals for batch 6 and batch 7 respectively. Figure 5.16 shows the residual of the EKF growing as more measurements are processed, which shows convergence to an incorrect solution. In Figure 5.17 the EKF residuals become smaller with additional observations; however, the scale of the graph shows that the EKF residuals remain large.

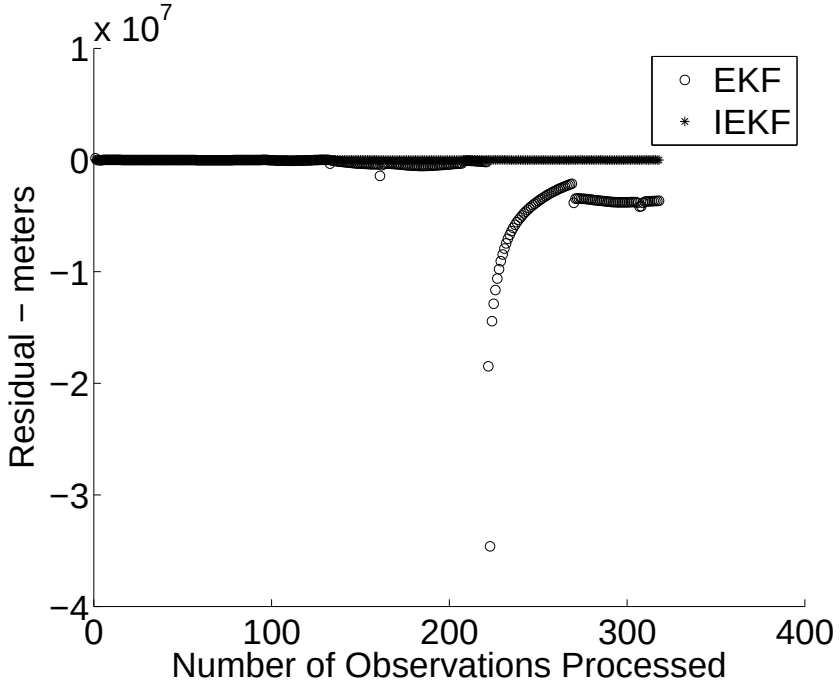


Figure 5.15: $\omega = 90^\circ$ : Residuals vs. Number of Observations Processed

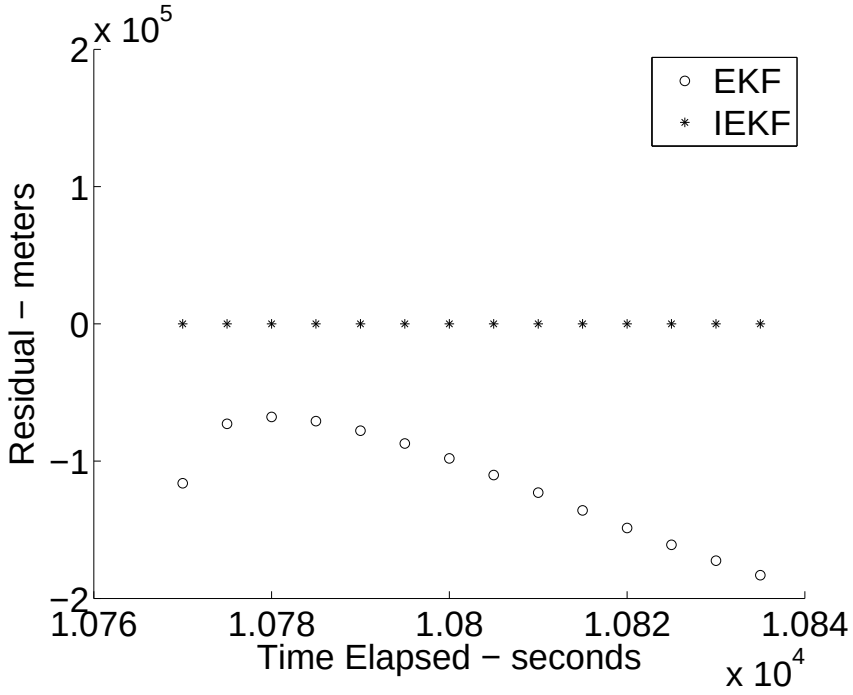


Figure 5.16: $\omega = 90°$ : Residuals for Batch #6

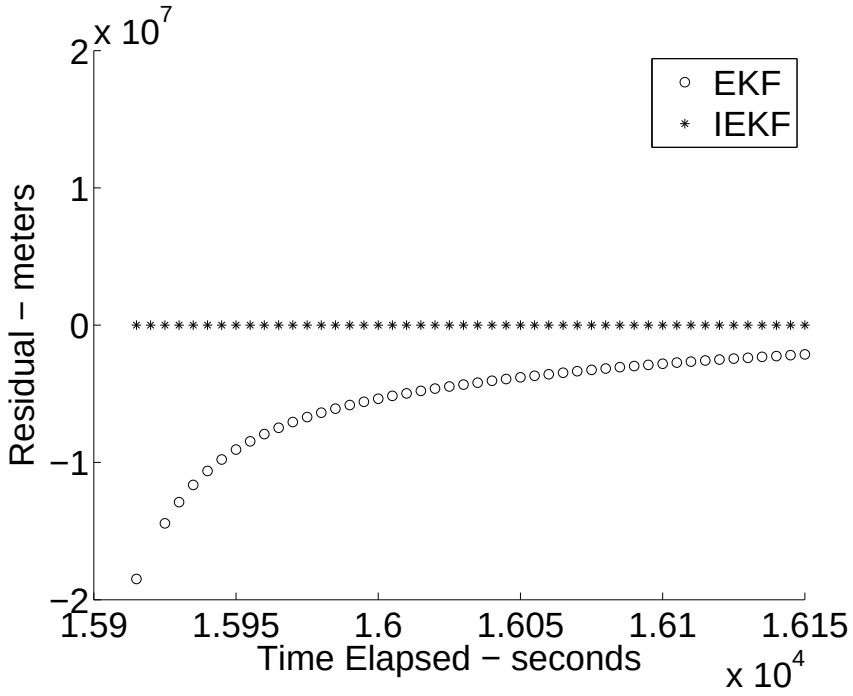


Figure 5.17: $\omega = 90°$ : Residuals for Batch #7

The performance parameter, $\eta$, shown in Figure 5.18, remains above the reference zero line for the entire simulation. Due to the scale on the graph, it is difficult to see this for approximately the first 150 observations.

The NMSE values for batch 6 and 7 are shown together in Figure 5.19. The NMSE of the EKF begins and ends greater than the NMSE of the IEKF for both batches. The NMSE values for batch 6 and batch 7 individually are shown in Figure 5.20 and Figure 5.21 respectively. For both batches, the IEKF NMSE value remains near zero, while the EKF NMSE is many orders of magnitude larger. Figure 5.21 shows the EKF NMSE becoming smaller similar to the residual from Figure 5.17. These large EKF NMSE values are a result of the innacuracy of the EKF estimate.

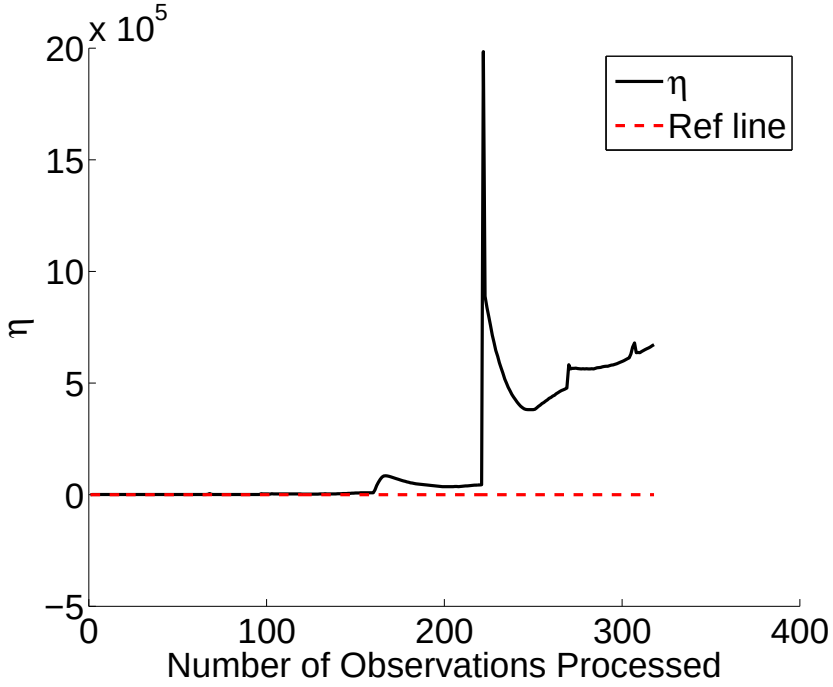


Figure 5.18: $\omega = 90°$ : $\eta$ vs. Number of Observations Processed

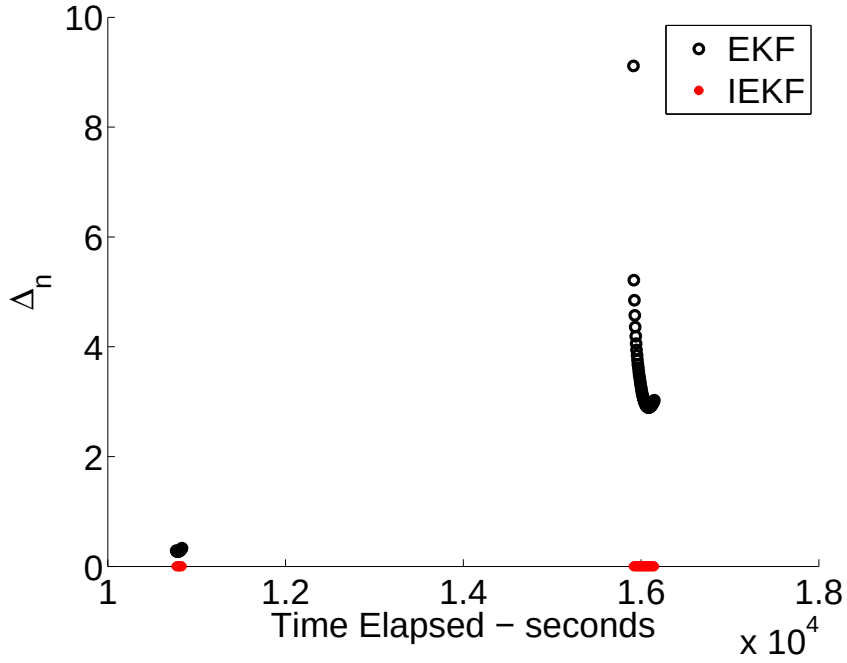


Figure 5.19: $\omega = 90°$ : NMSE for Batch #6 and Batch #7

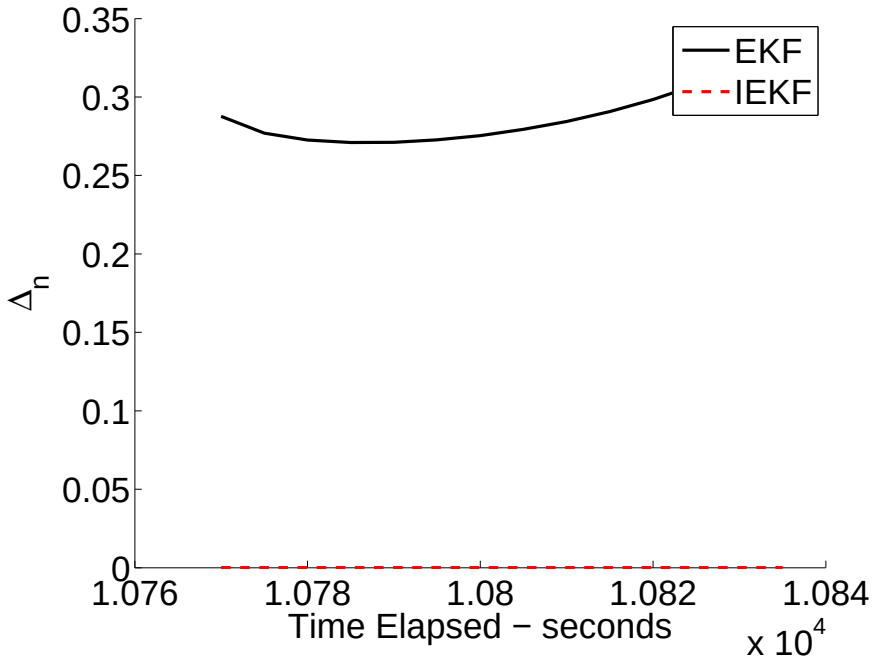


Figure 5.20: $\omega = 90°$ : NMSE for Batch #6

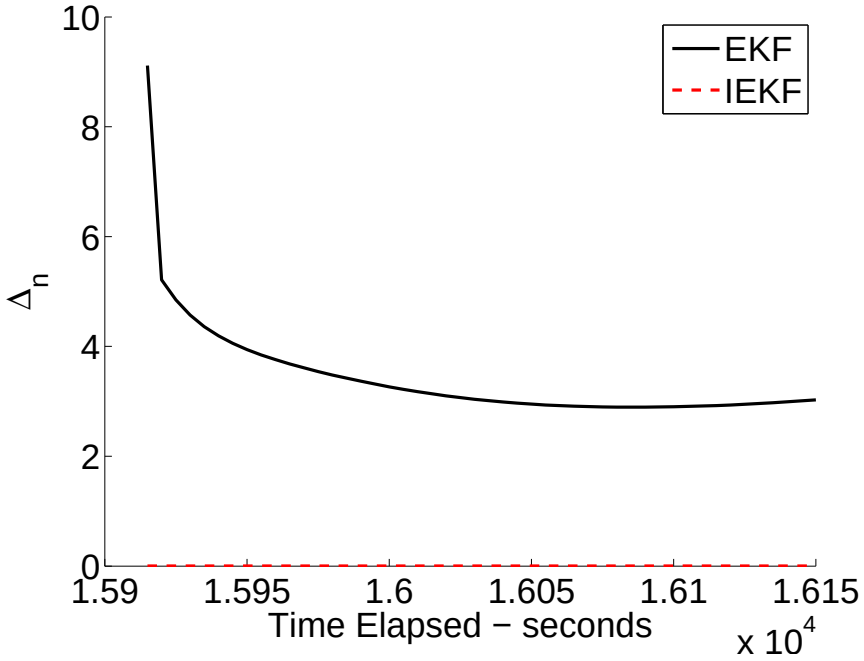


Figure 5.21: $\omega = 90°$ : NMSE for Batch #67

Table 5.11: $\omega = 90°$: Intermediate Output

| State | End of Batch #6 | | End of Batch #7) - After | |
|---|---|---|---|---|
| | $\alpha$ (EKF) | $\beta$ (IEKF) | $\alpha$ (EKF) | $\beta$ (IEKF) |
| X(m) | 407280.0317 | 4.9537 | 2340837.9835 | 8.0329 |
| Y(m) | 267709.9240 | 9.2157 | 566814.6803 | 0.7537 |
| Z(m) | 184296.0433 | 5.4234 | 3025870.0294 | 0.8134 |
| Vx(m/s) | 147.8404 | 0.0028 | 4731.1437 | 0.0081 |
| Vy(m/s) | 793.0966 | 0.0001 | 11469.8375 | 0.0044 |
| Vz(m/s) | 361.9798 | 0.0093 | 3859.5161 | 0.0169 |
| yk(m) | 183061.6412 | 7.8710 | 2134791.3973 | 3.3742 |
| NMSE | 3.3191E-001 | 8.2508E-006 | 3.0272E+000 | 6.9350E-006 |

Similar to the previous cases, the filter performance was compared for the batch before and the batch following the largest outage. This information can be found in Table 5.11. The EKF estimate has diverged from the true solution as clearly noted by the $\alpha$ values and residual; however, the performance of the IEKF did not suffer due to the initial outage or any outages throughout the simulation. This was due to the formulation of the IEKF algorithm. The covariance matrix is not updated until the iterated solution for each observation has converged, which is found in Equation 3.28.

Table 5.12: $\omega = 90°$: Output for All Observations (318 - 16460 $s$) Processed

| State | $\alpha$ (EKF) | $\beta$ (IEKF) |
|---|---|---|
| X(m) | 3197640.7249 | 5.3589 |
| Y(m) | 2571119.2984 | 1.2943 |
| Z(m) | 3567720.2319 | 5.9253 |
| Vx(m/s) | 7062.2632 | 0.0104 |
| Vy(m/s) | 8570.047 | 0.0042 |
| Vz(m/s) | 4803.1641 | 0.0147 |
| yk(m) | 3662603.4439 | 0.3185 |
| NMSE | 9.3240E+000 | 1.8473E-005 |

Following the processing of all additional measurements, the final performance values can be found in Table 5.12. The IEKF continues to produce an accurate estimate of the true state, from which it differs by a maximum of approximately 6 $m$ in any position component. The EKF estimate has diverged completely, which can be stated from the difference from the true state as well as the residual value.

## 5.5 Additional Results

Results for additional cases can be found Appendix B. The results of each case belong to one of three categories, which are defined from the previously discussed cases. Cases behaving similar to the baseline case include results where both filters provided accurate and similar results. Apparent divergence in the EKF, similar to the $i = 75.0°$ case, defines the second category of results. EKF divergence defines the third category, and was evident in the $\omega = 90°$ case. The categories of the additional test cases can be found in Table 5.13.

Table 5.13: Additional Results Details

| Test Case | Performance |
|---|---|
| $i = 28.5°$ | Similar performance |
| $\frac{r_p}{r_a} = 800km/1000km$ | EKF divergence |
| $\frac{r_p}{r_a} = 500km/700km$ | Similar performance |
| $\Omega = 0°$ | EKF divergence |
| $\Omega = 90°$ | Similar performance |
| $\omega = 45°$ | Apparent divergence |
| $\nu = 90°$ | Similar performance |
| $\nu = 270°$ | Apparent divergence |

# Chapter 6

## Conclusions and Future Work

A simulation was built to compare the performance of an Extended Kalman Filter and an Iterated Extended Kalman Filter for a piece of debris with poor *apriori* data, intermittent, and innacurate observations. The altitude, inclination, longitude of the ascending node, argument of periapsis, true anomaly, and measurement covariance were varied to generate fifteen cases of initial conditions for gaining the performance data for the two filtering methods. With a constant ground network to generate observations, the longitude of the ascending node, argument of periapsis, and true anomaly generated observation data sets with varying measurement outage times, which tested the ability of the filters to recover following an outage.

In many situations, the covariance matrix for the EKF became very small due to the low observation covariance and lack of process noise. This lead to smugness, or filter divergence due to the covariance matrix becoming small, in the EKF, an issue that was not anticipated during the problem formulation. The IEKF overcame this issue due to the process of calculating the covariance matrix from processing each measurement multiple times.

The performance of the IEKF generally allowed for a more accurate estimation of the state of the object with fewer measurements. However, this increase in accuracy occurred with an increase in computing cost. On average, the IEKF uses triple the processing needed by the EKF to produce an accuracy increase of at least an order of magnitude in the NMSE.

The changes to the observation residual of the measurement without a change to the given observation residual produced unexpected results. Since the IEKF processes a measurement multiple times, it was expected that an increase in the measurement noise to increase the error in the estimate of the state produced by the IEKF. However, the IEKF

continued to produce a more accurate estimate of the state than the EKF in this situation due to the ability to continue processing a measurement until local convergence.

To enhance this study in the future, many changes could be made to the simulation. Including process noise and aerodynamic drag in the dynamical model, adding intermittent measurements based on the attitude of the debris, and incorporating a detailed analysis of the computing power required are a few changes that could be incorporated to extend this study. The addition of process noise would test the ability of the IEKF to filter unknown accelerations. Aerodynamic drag calculations would allow LEO conditions to be better tested. Intermittent measurements based on the attitude of the debris would allow for the modeling of debris that might not produce a radar echo due to an orientation, which is an issue with lower power radar stations or small debris. A detailed analysis of the increase in computing power would allow for the formation of a ratio of increased power needed to the increase in accuracy to be defined. This definition would allow for an in depth study of all higher order filters for orbit determination to be compared more easily.

Bibliography


[1] *Orbital Debris: A Technical Assessment*, National Academy, 1995.

[2] Kessler, D. J. and Cour-Palais, B. G., "Collision Frequency of Artificial Satellites: The Creation of a Debris Belt," *Orbital Debris Quarterly News*, Vol. 83, 1978.

[3] Portree, D. S. and Joseph P. Loftus, J., "Orbital Debris: A Chronology," NASA paper nasa/tp-1999-208856, 1999.

[4] *Limiting Future Collision Risk to Spacecraft: An Assessment of NASA's Meteoroid and Orbital Debris Programs*, National Academies, 2011.

[5] Liou, J.-C. and Shoots, D., "Fengyun-1C Debris: One Year Later," *Orbital Debris Quarterly News*, Vol. 12, No. 1, 2008.

[6] Liou, J.-C. and Johnson, N. L., "A Sensitivity Study of the Effectiveness of Active Debris Removal in LEO," *Acta Astronautica*, Vol. 64, 2009, pp. 236 – 243.

[7] Kessler, D. J., Johnson, N. L., Liou, J.-C., and Matney, M., "The Kessler Syndrome: Implications to Future Space Operations," AAS paper 10-016, 2010.

[8] Sibert, D., Borgeson, D., Peterson, G., Jenkin, A., and Sorge, M., "Operational Impact of Improved Space Tracking on Collision Avoidance in the Future LEO Space Debris Environment," USAF space command report, 2010.

[9] Thomson, W. T., *Introduction to Space Dynamics*, Wiley, 1961.

[10] Montenbruck, O. and Gill, E., *Satellite Orbits: Models, Methods and Applications*, Springer, 2005.

[11] Chobotov, V. A., *Orbital Mechanics*, American Institute of Aeronautics and Astronautics, Inc., 2002.

[12] Tapley, B. D., Shutz, B. E., and Born, G. H., *Statistical Orbit Determination*, Elsevier Academic Press, 2004.

[13] Gelb, A., *Applied Optimal Estimation*, M.I.T. Press, 1974.

[14] Jazwinski, A. H., *Stochastic Processes and Filtering Theory*, Academic Press, 1970.

[15] Simon, D., *Optimal State Estimation: Kalman, H [infinity] and Nonlinear Approaches*, Wiley, 2006.

[16] Kelso, T., "Validation of SGP4 and IS-GPS-200D Against GPS Precision Ephemerides," AAS paper 07-127, 2007.

[17] Vallado, D. A. and McClain, W. D., *Fundamentals of Astrodynamics and Applications*, Springer, 2007.

Appendices

# Appendix A

## Derivation of $J_2$ Equations of motion

In chapter 2, the acceleration due to the $J_2$ perturbation was discussed. The full derivation of the $J_2$ acceleration in ECI components will be presented here, which will begin with Equation 2.7 and Equation 2.8, and end with Equation 2.9, which are also presented below as Equation A.1, Equation A.2, and Equation A.3 respectively for completion.

$$U_{J_2} = \frac{-\mu}{r} J_2 \left(\frac{r_e}{r}\right)^2 \left(\left(\frac{3}{2}\right) sin(\phi) - \left(\frac{1}{2}\right)\right) \tag{A.1}$$

$$\ddot{\boldsymbol{r}} = \nabla U_{J_2} \tag{A.2}$$

$$\ddot{\boldsymbol{r}}_{J_2} = \frac{\frac{3}{2}\mu J_2 r_e^2}{r^7} \begin{bmatrix} X_1\left(5X_3^2 - r^2\right) \\ X_2\left(5X_3^2 - r^2\right) \\ X_3\left(5X_3^2 - 3r^2\right) \end{bmatrix} \tag{A.3}$$

Expanding the gradient operator in Equation A.2 yields Equation A.4, which will be evaluated individually by component.

$$\nabla U_{J_2} = \frac{\partial U_{J_2}}{\partial X_1}\,\hat{\mathbf{I}} + \frac{\partial U_{J_2}}{\partial X_2}\,\hat{\mathbf{J}} + \frac{\partial U_{J_2}}{\partial X_3}\,\hat{\mathbf{K}} \tag{A.4}$$

The definition of $\mathbf{r}$ in the ECI coordinate system and the norm of $\mathbf{r}$, Equation A.5 and Equation A.6 respectfully, will be used to transform a portion of Equation A.1 from spherical

coordinate frame to the ECI coordinate frame. A substitution for $sin(\phi)$ will complete the transformation, and is found from Figure 2.5. This is presented in Equation A.7.

$$\mathbf{r} = [X_1 \;\; X_2 \;\; X_3] \begin{bmatrix} \mathbf{I} \\ \mathbf{J} \\ \mathbf{K} \end{bmatrix} \tag{A.5}$$

$$r = \left[X_1^2 + X_2^2 + X_3^2\right]^{\frac{1}{2}} \tag{A.6}$$

$$sin(\phi) = \frac{X_3}{r} \tag{A.7}$$

Substitute Equation A.7 into Equation A.1 and distribute.

$$U_{J_2} = \frac{-\frac{3}{2}\mu J_2 r_e^2 X_3^2}{r^5} + \frac{\frac{1}{2}\mu J_2 r_e^2}{r^3} \tag{A.8}$$

Substitute Equation A.6 into Equation A.8 and invert the denominators. This now gives $U_{J_2}$ only in terms of constants and the components of the ECI position vector.

$$U_{J_2} = -\frac{3}{2}\mu J_2 r_e^2 X_3^2 \left(X_1^2 + X_2^2 + X_3^2\right)^{-\frac{5}{2}} + \frac{1}{2}\mu J_2 r_e^2 \left(X_1^2 + X_2^2 + X_3^2\right)^{-\frac{3}{2}} \tag{A.9}$$

Combine the constants $\mu$ $J_2$ and $r_e^2$ to form a new constant C and substitute into Equation A.9.

$$C = \mu J_2 r_e^2 \tag{A.10}$$

$$U_{J_2} = -\frac{3}{2} C X_3^2 \left(X_1^2 + X_2^2 + X_3^2\right)^{-\frac{5}{2}} + \frac{1}{2} C \left(X_1^2 + X_2^2 + X_3^2\right)^{-\frac{3}{2}} \tag{A.11}$$

**$\hat{\mathbf{I}}$ Component**

$$(\nabla U_{J_2})_i = \frac{\partial}{\partial X_1}\left[-\frac{3}{2}CX_3^2\left(X_1^2+X_2^2+X_3^2\right)^{-\frac{5}{2}}+\frac{1}{2}C\left(X_1^2+X_2^2+X_3^2\right)^{-\frac{3}{2}}\right] \tag{A.12}$$

Perform the chain rule on each portion of the sum.

$$(\nabla U_{J_2})_i = \left(-\frac{15}{4}\right)(2X_1)\,CX_3^2\left(X_1^2+X_2^2+X_3^2\right)^{-\frac{7}{2}}+\left(-\frac{3}{4}\right)(2X_1)\,C\left(X_1^2+X_2^2+X_3^2\right)^{-\frac{5}{2}} \tag{A.13}$$

Simplify, obtain a common denominator, factor the numerator and substitute for C.

$$(\nabla U_{J_2})_i = \left(\frac{15}{2}\right)\frac{CX_3^2X_1}{r^7}+\left(-\frac{3}{2}\right)\frac{CX_1}{r^5} \tag{A.14}$$

$$(\nabla U_{J_2})_i = \left(\frac{15}{2}\right)\frac{CX_3^2X_1}{r^7}+\left(-\frac{3}{2}\right)\frac{CX_1r^2}{r^7} \tag{A.15}$$

$$(\nabla U_{J_2})_i = \frac{\frac{3}{2}\mu J_2 r_e^2 X_1\left(5X_3^2-r^2\right)}{r^7} \tag{A.16}$$

**$\hat{\mathbf{J}}$ Component**

$$(\nabla U_{J_2})_j = \frac{\partial}{\partial X_2}\left[-\frac{3}{2}CX_3^2\left(X_1^2+X_2^2+X_3^2\right)^{-\frac{5}{2}}+\frac{1}{2}C\left(X_1^2+X_2^2+X_3^2\right)^{-\frac{3}{2}}\right] \tag{A.17}$$

Perform the chain rule on each portion of the sum.

$$\left(\nabla U_{J_2}\right)_j = \left(\frac{15}{4}\right)\left(2X_2\right) C X_3^2 \left(X_1^2 + X_2^2 + X_3^2\right)^{-\frac{7}{2}} + \left(-\frac{3}{4}\right)\left(2X_2\right) C \left(X_1^2 + X_2^2 + X_3^2\right)^{-\frac{5}{2}} \tag{A.18}$$

Simplify, obtain a common denominator, factor the numerator and substitute for C.

$$\left(\nabla U_{J_2}\right)_j = \left(\frac{15}{2}\right)\frac{C X_3^2 X_2}{r^7} + \left(-\frac{3}{2}\right)\frac{C X_2}{r^5} \tag{A.19}$$

$$\left(\nabla U_{J_2}\right)_j = \left(\frac{15}{2}\right)\frac{C X_3^2 X_2}{r^7} + \left(-\frac{3}{2}\right)\frac{C X_2 r^2}{r^7} \tag{A.20}$$

$$\left(\nabla U_{J_2}\right)_j = \frac{\frac{3}{2}\mu J_2 r_e^2 X_2 \left(5X_3^2 - r^2\right)}{r^7} \tag{A.21}$$

**$\hat{\mathbf{K}}$ Component**

$$\left(\nabla U_{J_2}\right)_k = \frac{\partial}{\partial X_3}\left[-\frac{3}{2} C X_3^2 \left(X_1^2 + X_2^2 + X_3^2\right)^{-\frac{5}{2}} + \frac{1}{2} C \left(X_1^2 + X_2^2 + X_3^2\right)^{-\frac{3}{2}}\right] \tag{A.22}$$

Perform the chain rule on each portion of the sum (broken into the three terms for clarity).

$$\left(\nabla U_{J_2}\right)_k = \left(-\frac{3}{2}\right)\left(2X_3\right) C \left(X_1^2 + X_2^2 + X_3^2\right)^{-\frac{5}{2}} \tag{A.23}$$

$$+ \left(\frac{15}{4}\right)\left(2X_3\right) C X_3^2 \left(X_1^2 + X_2^2 + X_3^2\right)^{-\frac{7}{2}} \tag{A.24}$$

$$+\left(-\frac{3}{4}\right)(2X_3)\,C\left(X_1^2+X_2^2+X_3^2\right)^{-\frac{5}{2}} \tag{A.25}$$

Sum Equations A.23 - A.25 and simplify, obtain a common denominator, factor the numerator and substitute for C.

$$(\nabla U_{J_2})_k = \left(\frac{15}{2}\right)\frac{CX_3^2X_3}{r^7} - \left(\frac{9}{2}\right)\frac{CX_3}{r^5} \tag{A.26}$$

$$(\nabla U_{J_2})_k = \left(\frac{15}{2}\right)\frac{CX_3^2X_3}{r^7} - \left(\frac{9}{2}\right)\frac{CX_3r^2}{r^7} \tag{A.27}$$

$$(\nabla U_{J_2})_k = \frac{\frac{3}{2}\mu J_2 r_e^2 X_3\left(5X_3^2-3r^2\right)}{r^7} \tag{A.28}$$

**Result**

Combining Equation A.16, Equation A.21, and Equation A.28 yields the equations of motion for the $J_2$ perturbation in the ECI coordinate frame.

$$\mathbf{a}_{J_2} = \frac{\frac{3}{2}\mu J_2 r_e^2}{r^7}\begin{bmatrix} X_1\left(5X_3^2-r^2\right) \\ X_2\left(5X_3^2-r^2\right) \\ X_3\left(5X_3^2-3r^2\right)\end{bmatrix} \tag{A.29}$$

Appendix B

Additional Results

## B.1 Variations on Inclination

### B.1.1 Inclination $\rightarrow i = 28.5°$

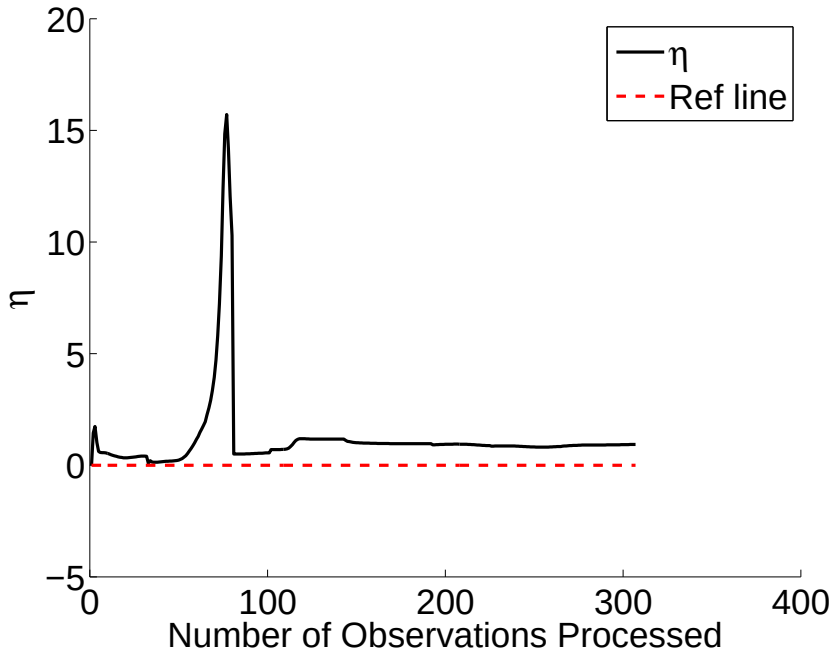


Figure B.1: $i = 28.5°$ : $\eta$ vs. Number of Observations Processed

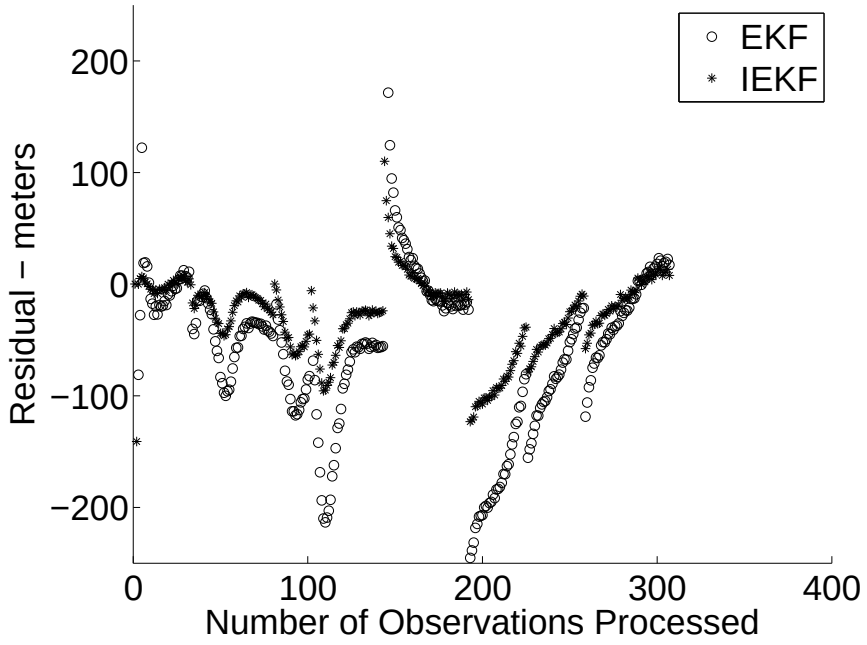


Figure B.2: $i = 28.5°$ : Residuals vs. Number of Observations Processed

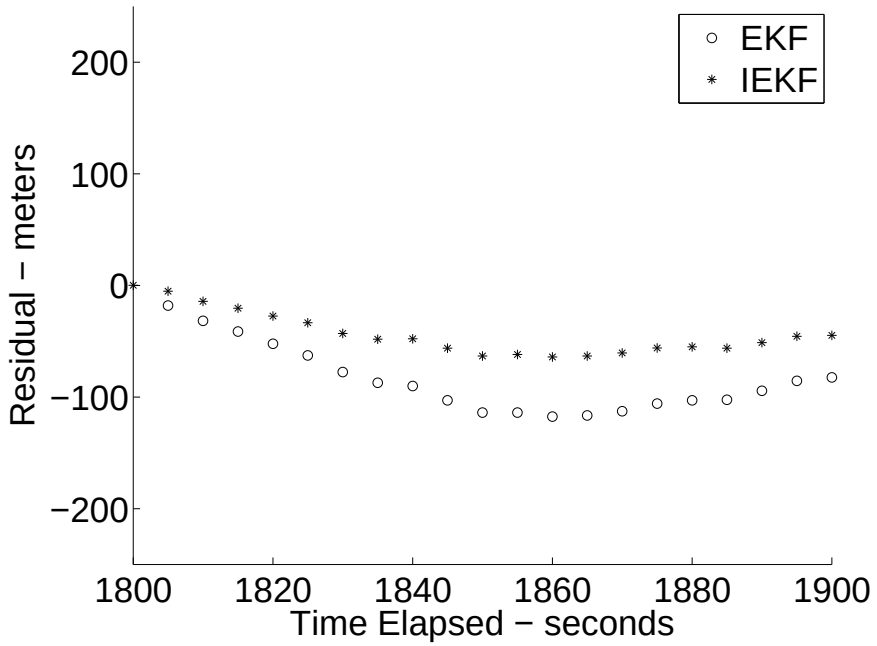


Figure B.3: $i = 28.5°$ : Residuals Before Largest Outage vs. Time

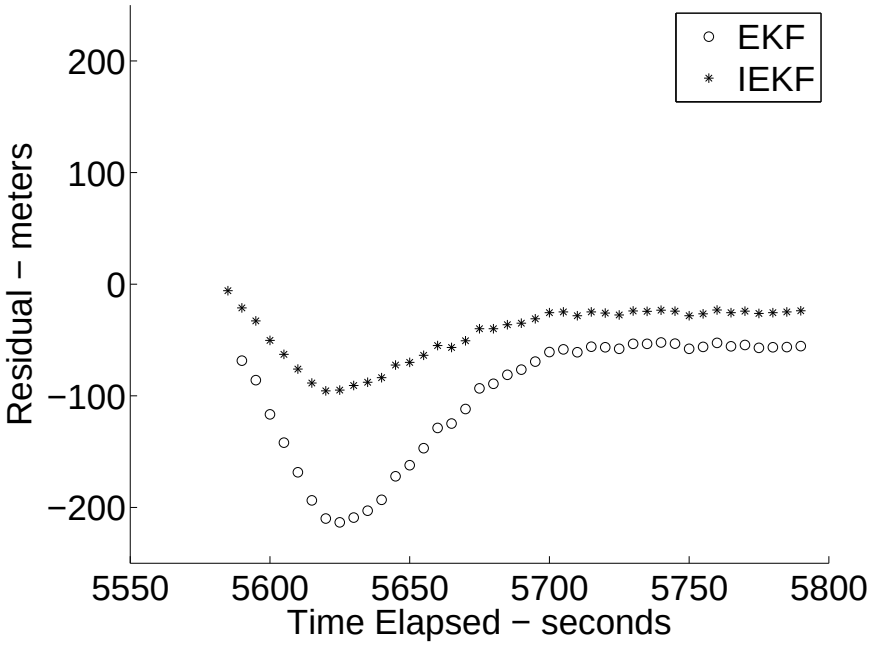


Figure B.4: $i = 28.5°$ : Residuals After Largest Outage vs. Time

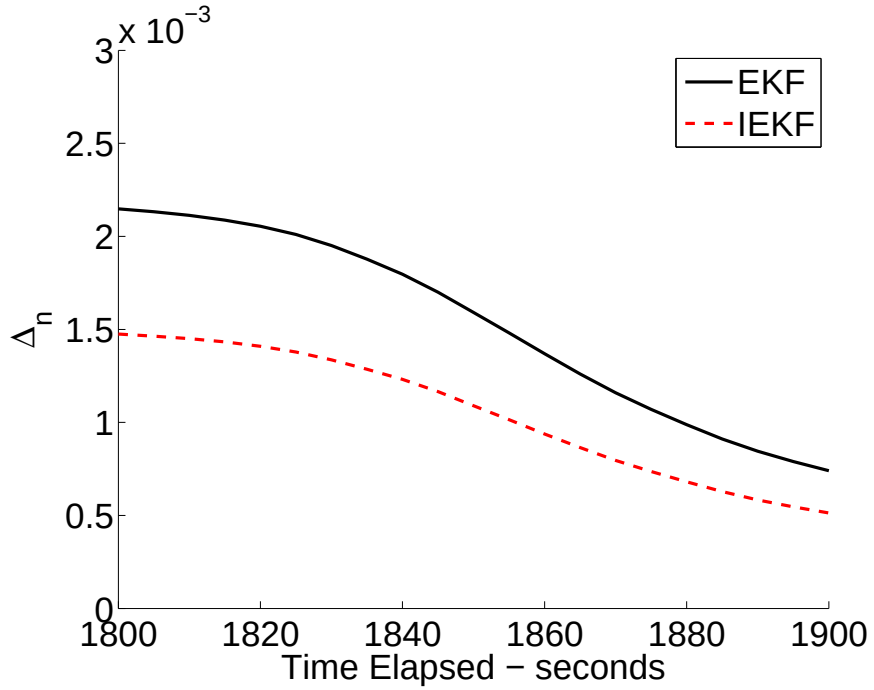


Figure B.5: $i = 28.5°$ : NMSE Before Largest Outage vs. Time

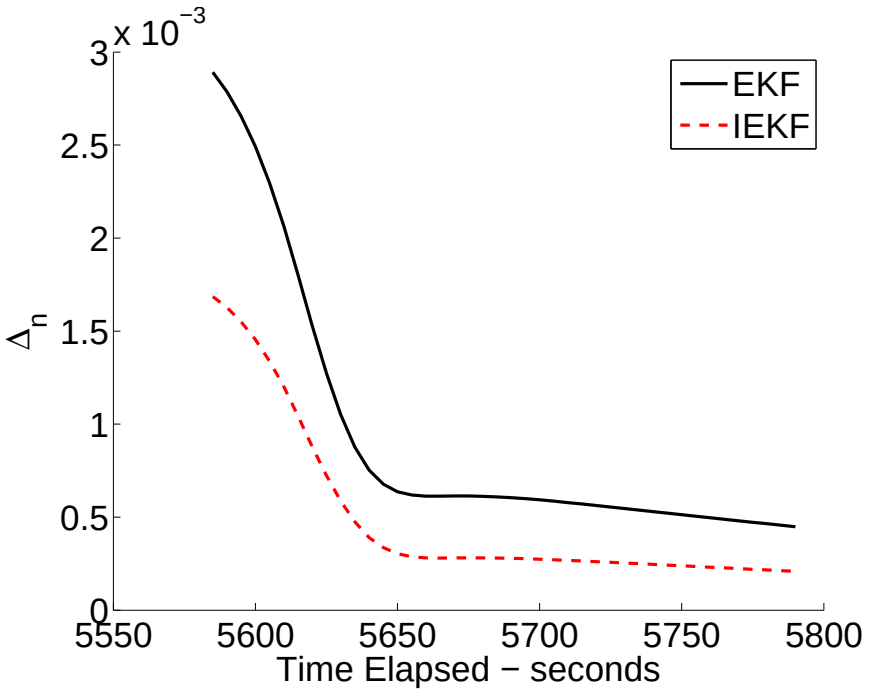


Figure B.6: $i = 28.5°$ : NMSE After Largest Outage vs. Time

Table B.1: $i = 28.5°$: Intermediate Output

| | 101 observations (1900 $s$) - Before | | 143 observations (5790 $s$) - After | |
|---|---|---|---|---|
| State | $\alpha$ (EKF) | $\beta$ (IEKF) | $\alpha$ (EKF) | $\beta$ (IEKF) |
| X(m) | 696.7952 | 447.1226 | 169.4131 | 78.3011 |
| Y(m) | 50.5685 | 15.1300 | 476.5338 | 217.3360 |
| Z(m) | 94.0815 | 71.4660 | 461.5652 | 215.0349 |
| Vx(m/s) | 1.9554 | 1.2306 | 0.5576 | 0.2643 |
| Vy(m/s) | 0.2796 | 0.1241 | 0.0613 | 0.0128 |
| Vz(m/s) | 1.1402 | 0.8525 | 0.0168 | 0.0021 |
| yk(m) | 82.3730 | 44.7652 | 55.6191 | 23.8096 |
| NMSE | 7.4027E-004 | 5.1267E-004 | 4.4888E-004 | 2.0883E-004 |

Table B.2: $i = 28.5°$: Output for All Observations (307 - 7830 $s$) Processed

| State | $\alpha$ (EKF) | $\beta$ (IEKF) |
|---|---|---|
| X(m) | 3.1548 | 2.4580 |
| Y(m) | 21.5692 | 10.5556 |
| Z(m) | 87.5892 | 45.5551 |
| Vx(m/s) | 0.0584 | 0.0299 |
| Vy(m/s) | 0.0095 | 0.0046 |
| Vz(m/s) | 0.2404 | 0.1244 |
| yk(m) | 17.1910 | 7.7568 |
| NMSE | 9.5393E-005 | 4.9467E-005 |

## B.2 Variations on Altitude

### B.2.1 Altitudes $\rightarrow \frac{r_p}{r_a} = 800km/1000km$

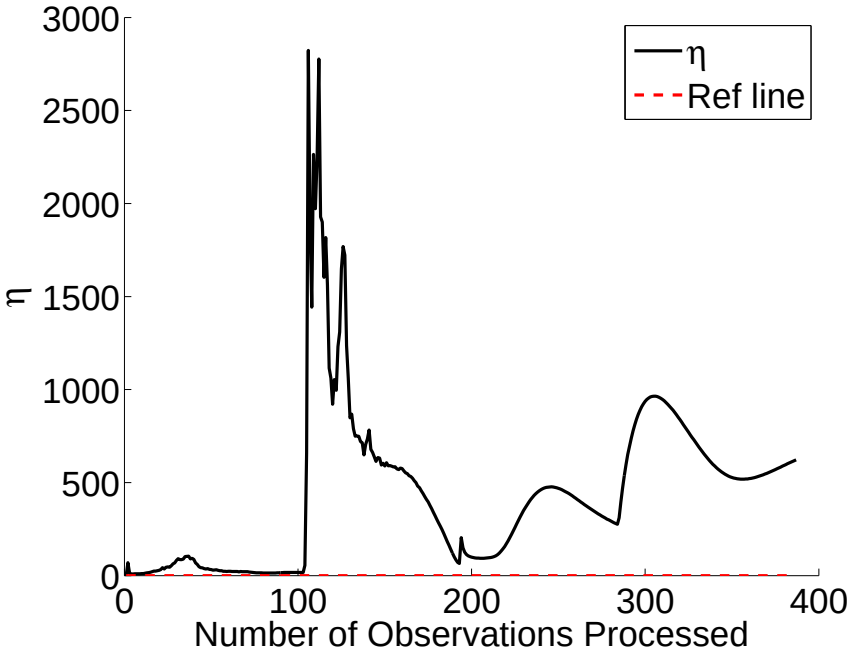


Figure B.7: $\frac{r_p}{r_a} = 800km/1000km$ : $\eta$ vs. Number of Observations Processed

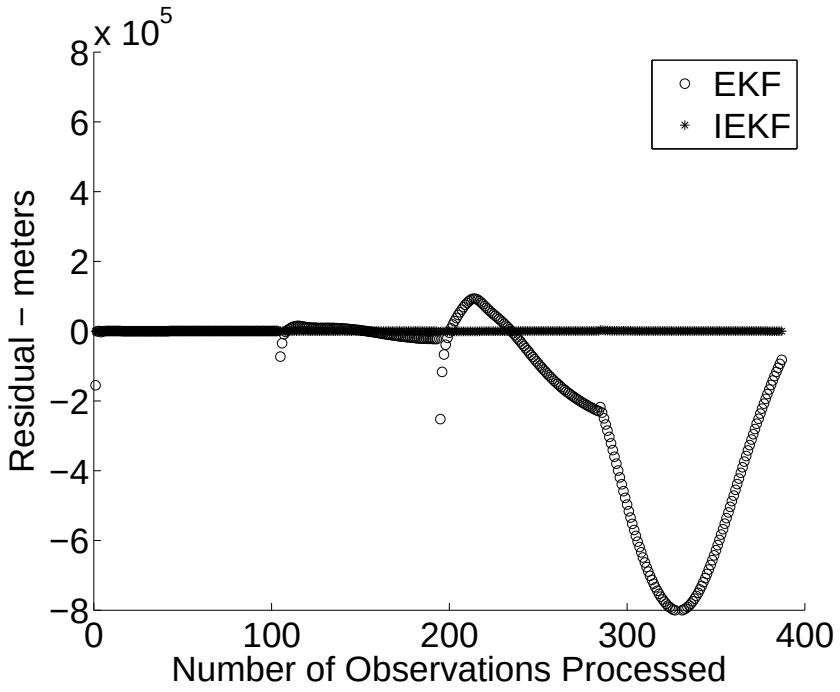


Figure B.8: $\frac{r_p}{r_a} = 800km/1000km$ : Residuals vs. Number of Observations Processed

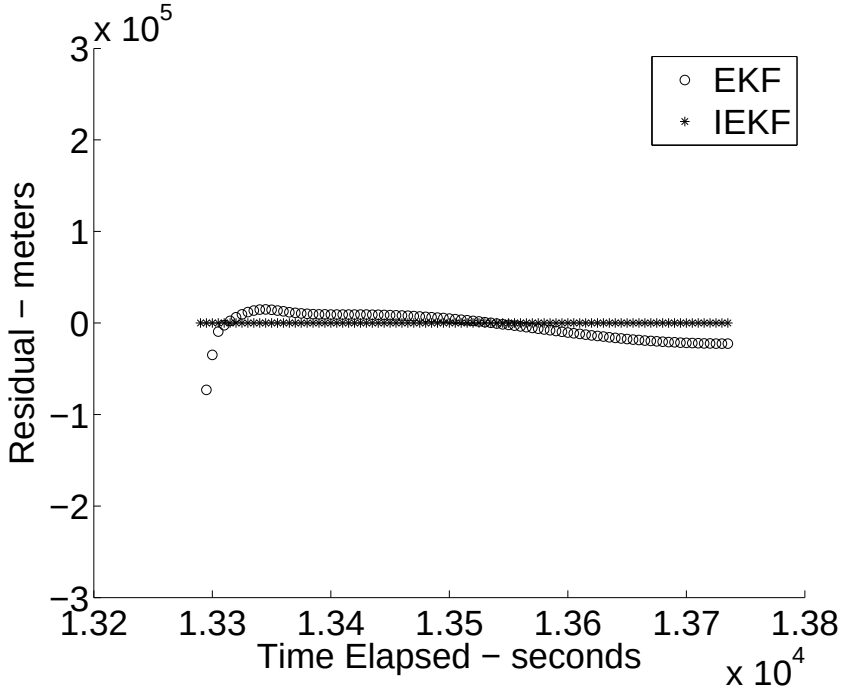


Figure B.9: $\frac{r_p}{r_a} = 800km/1000km$ : Residuals Before Largest Outage vs. Time

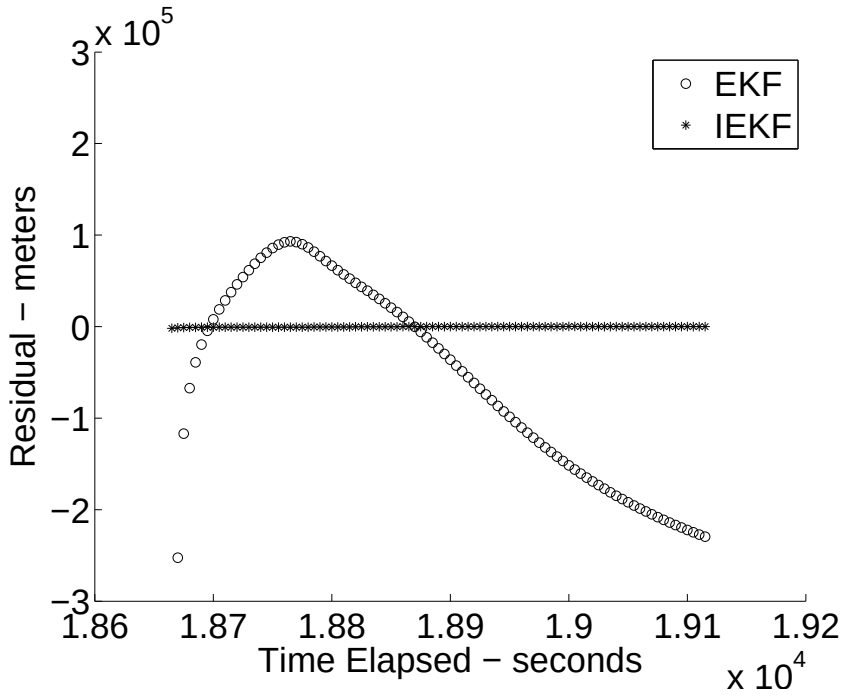


Figure B.10: $\frac{r_p}{r_a} = 800km/1000km$ : Residuals After Largest Outage vs. Time

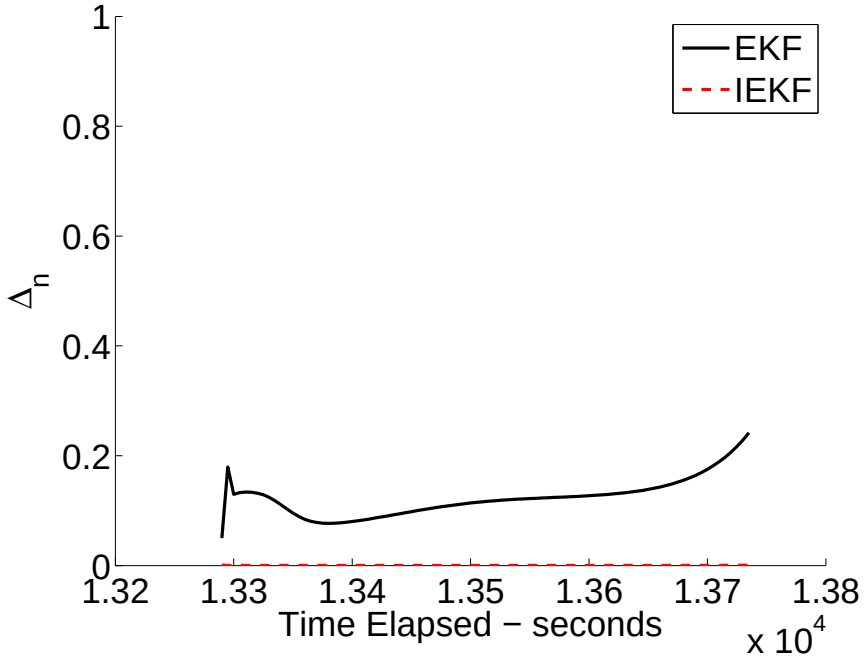


Figure B.11: $\frac{r_p}{r_a} = 800km/1000km$ : NMSE Before Largest Outage vs. Time

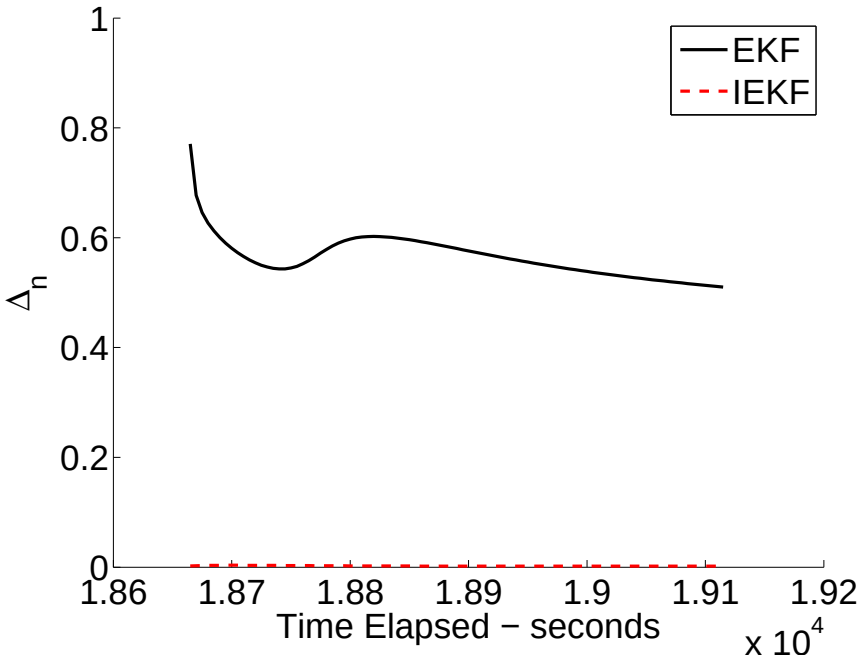


Figure B.12: $\frac{r_p}{r_a} = 800km/1000km$ : NMSE After Largest Outage vs. Time

Table B.3: $\frac{r_p}{r_a} = 800km/1000km$: Intermediate Output

| | 103 observations (3180 $s$) - Before | | 193 observations (13735 $s$) - After | |
|---|---|---|---|---|
| State | $\alpha$ (EKF) | $\beta$ (IEKF) | $\alpha$ (EKF) | $\beta$ (IEKF) |
| X(m) | 30803.5776 | 843.7531 | 10827.2371 | 68.2194 |
| Y(m) | 21335.0050 | 2114.0440 | 19576.7362 | 58.0021 |
| Z(m) | 22438.5898 | 898.8687 | 3489.0570 | 328.0003 |
| Vx(m/s) | 34.8935 | 0.1445 | 110.3779 | 0.0079 |
| Vy(m/s) | 12.7174 | 3.5697 | 84.6951 | 0.1300 |
| Vz(m/s) | 17.0665 | 2.3051 | 101.5724 | 0.1981 |
| yk(m) | 126.8850 | 4.5325 | 22496.07682 | 0.0034 |
| NMSE | 6.0557E-002 | 3.9742E-003 | 2.4168E-001 | 4.4422E-004 |

Table B.4: $\frac{r_p}{r_a} = 800km/1000km$: Output for All Observations (387 - 20195 $s$) Processed

| State | $\alpha$ (EKF) | $\beta$ (IEKF) |
|---|---|---|
| X(m) | 669004.4833 | 483.2484 |
| Y(m) | 580538.8523 | 86.5897 |
| Z(m) | 701111.6741 | 1743.8944 |
| Vx(m/s) | 73.9316 | 0.9436 |
| Vy(m/s) | 991.5891 | 1.1375 |
| Vz(m/s) | 1289.7717 | 1.4730 |
| yk(m) | 82558.1852 | 102.4162 |
| NMSE | 1.7505E+000 | 1.9810E-003 |

### B.2.2 Altitudes $\rightarrow \frac{r_p}{r_a} = 500km/700km$

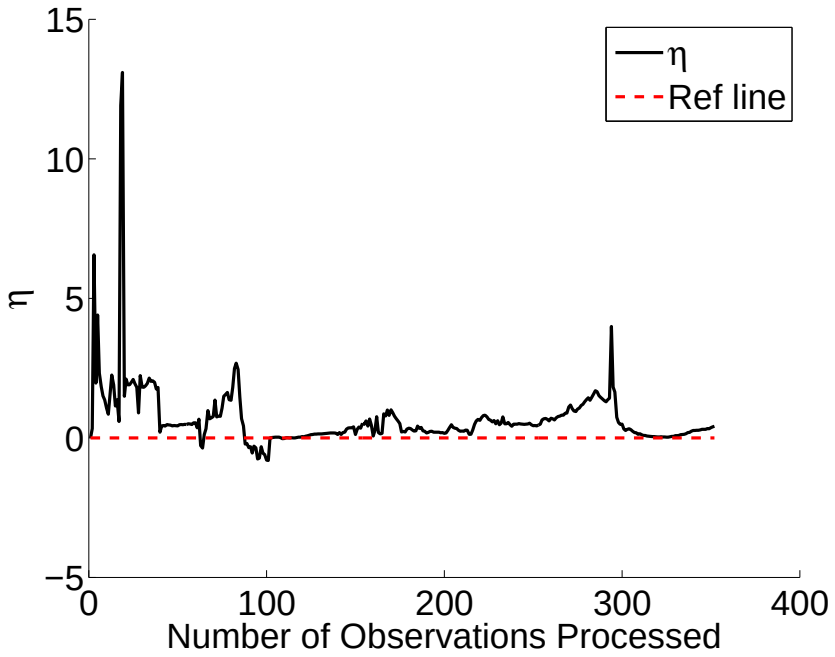


Figure B.13: $\frac{r_p}{r_a} = 500km/700km$ : $\eta$ vs. Number of Observations Processed

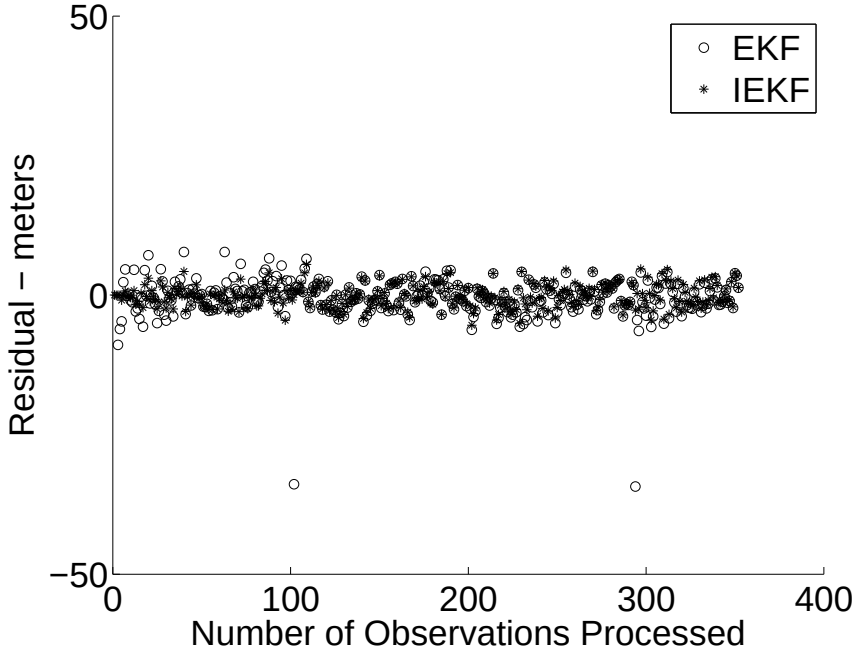


Figure B.14: $\frac{r_p}{r_a} = 500km/700km$ : Residuals vs. Number of Observations Processed

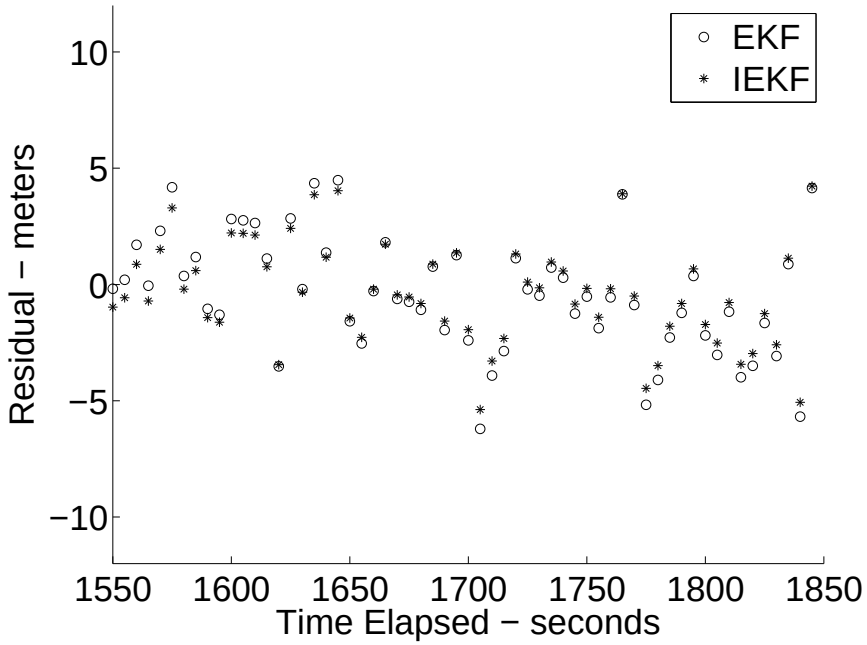


Figure B.15: $\frac{r_p}{r_a} = 500km/700km$ : Residuals Before Largest Outage vs. Time

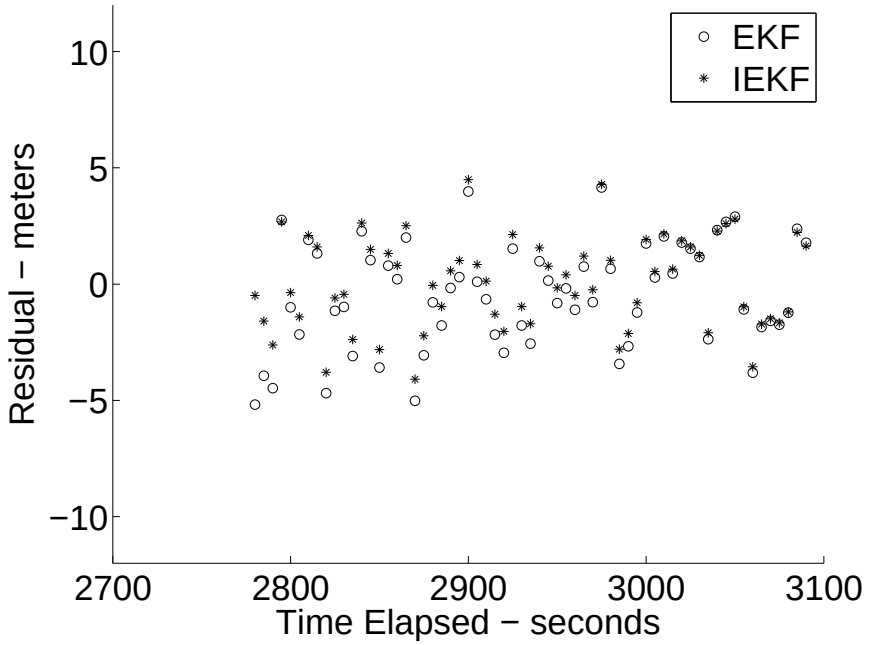


Figure B.16: $\frac{r_p}{r_a} = 500km/700km$ : Residuals After Largest Outage vs. Time

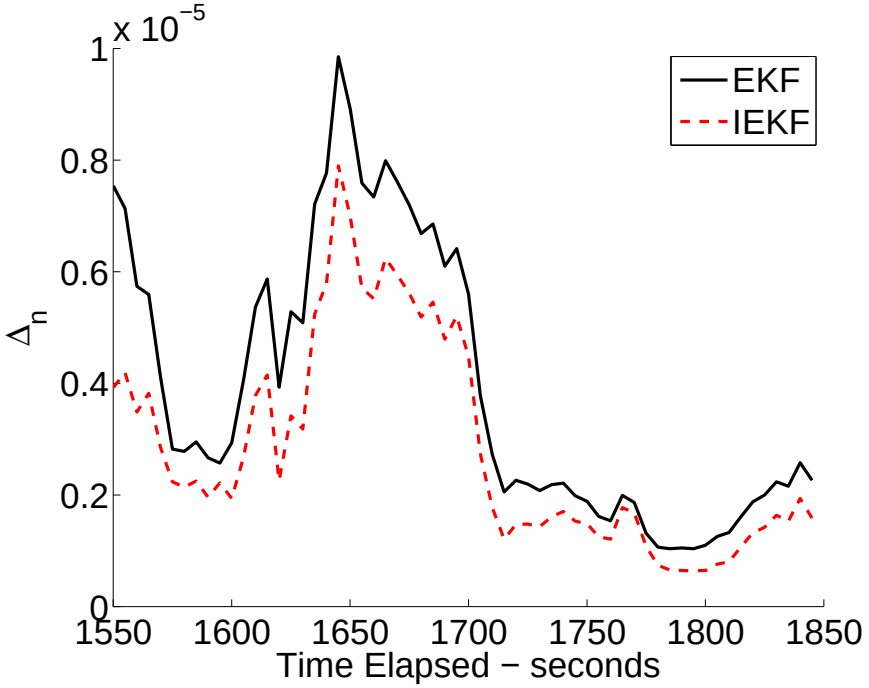


Figure B.17: $\frac{r_p}{r_a} = 500km/700km$ : NMSE Before Largest Outage vs. Time

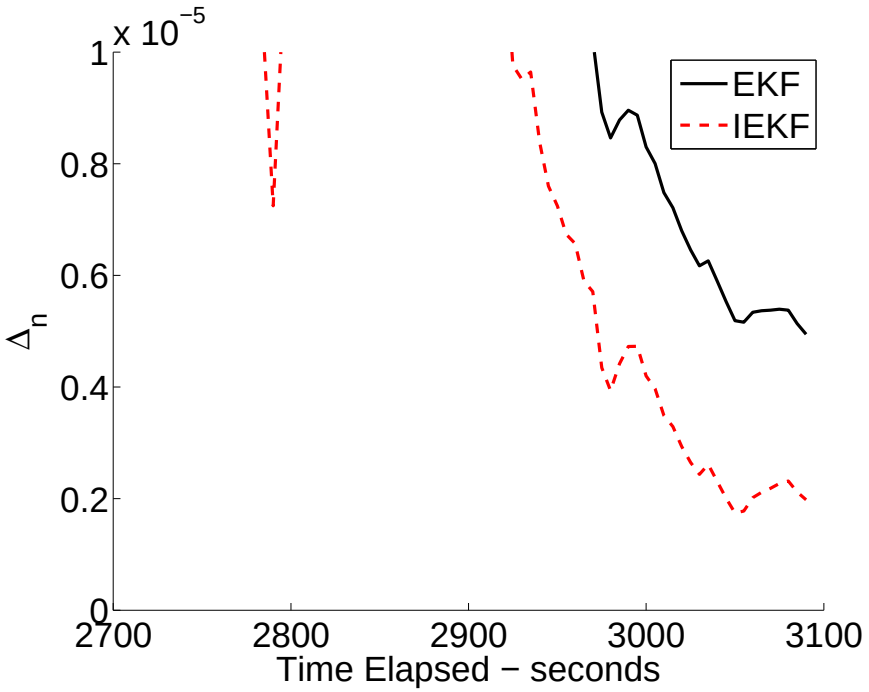


Figure B.18: $\frac{r_p}{r_a} = 500km/700km$ : NMSE After Largest Outage vs. Time

Table B.5: $\frac{r_p}{r_a} = 500km/700km$: Intermediate Output

| | 230 observations (1845 $s$) - Before | | 293 observations (3090 $s$) - After | |
|---|---|---|---|---|
| State | $\alpha$ (EKF) | $\beta$ (IEKF) | $\alpha$ (EKF) | $\beta$ (IEKF) |
| X(m) | 3.9550 | 2.5127 | 2.9155 | 1.3144 |
| Y(m) | 1.8746 | 0.9790 | 5.2372 | 2.1131 |
| Z(m) | 0.3748 | 0.3505 | 1.2955 | 0.4534 |
| Vx(m/s) | 0.0039 | 0.0030 | 0.0001 | 0.0001 |
| Vy(m/s) | 0.0027 | 0.0004 | 0.0069 | 0.0025 |
| Vz(m/s) | 0.0010 | 0.0005 | 0.0019 | 0.0010 |
| yk(m) | 4.1478 | 4.2310 | 1.7809 | 1.6388 |
| NMSE | 2.2612E-006 | 1.5855E-006 | 4.9449E-006 | 1.9766E-006 |

Table B.6: $\frac{r_p}{r_a} = 500km/700km$: Output for All Observations (352 - 6125 $s$) Processed

| State | $\alpha$ (EKF) | $\beta$ (IEKF) |
|---|---|---|
| X(m) | 1.2736 | 0.9745 |
| Y(m) | 0.5712 | 0.0809 |
| Z(m) | 0.0420 | 0.1487 |
| Vx(m/s) | 0.0003 | 0.0007 |
| Vy(m/s) | 0.0008 | 0.0004 |
| Vz(m/s) | 0.0001 | 0.0001 |
| yk(m) | 1.3117 | 1.3566 |
| NMSE | 8.1530E-007 | 6.2982E-007 |

## B.3 Variations on Longitude of the Ascending Node

### B.3.1 Longitude of the Ascending Node $\rightarrow \Omega = 0°$

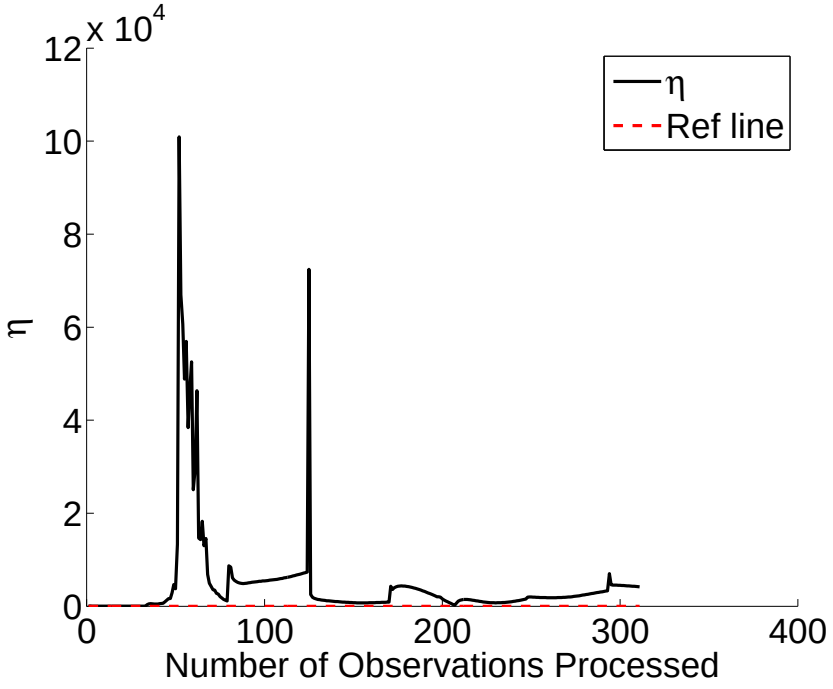


Figure B.19: $\Omega = 0°$ : $\eta$ vs. Number of Observations Processed

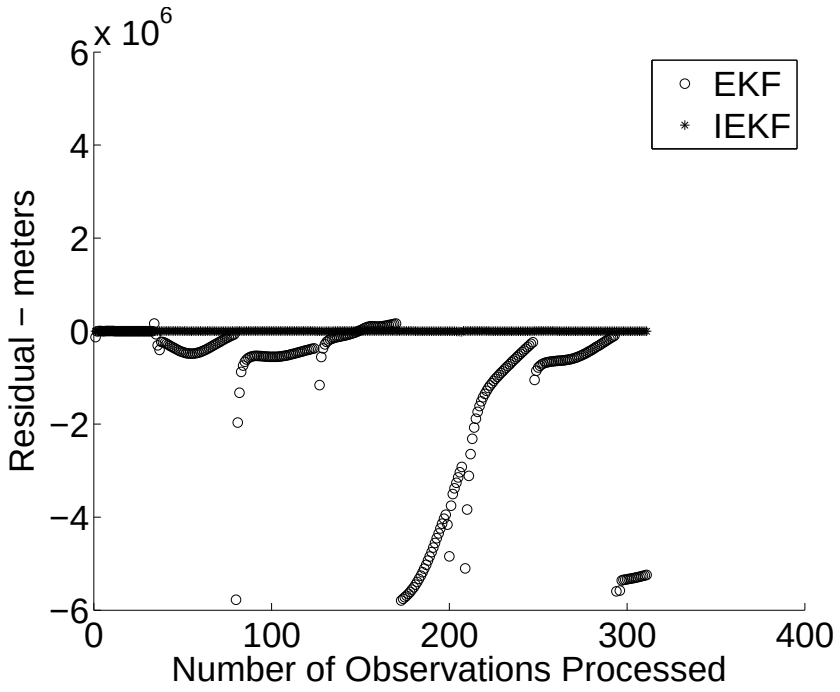


Figure B.20: $\Omega = 0°$ : Residuals vs. Number of Observations Processed

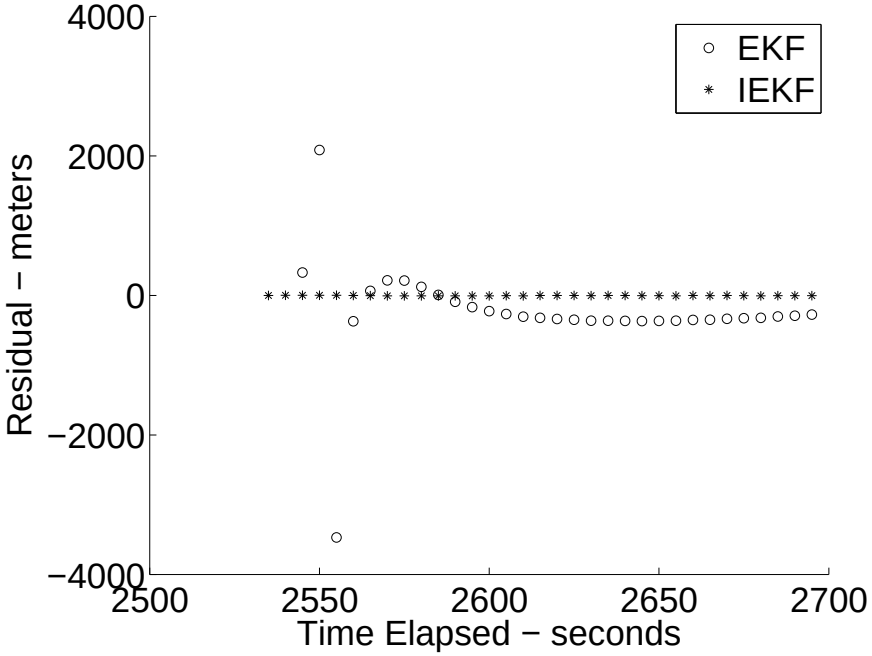


Figure B.21: $\Omega = 0°$ : Residuals Before Largest Outage vs. Time

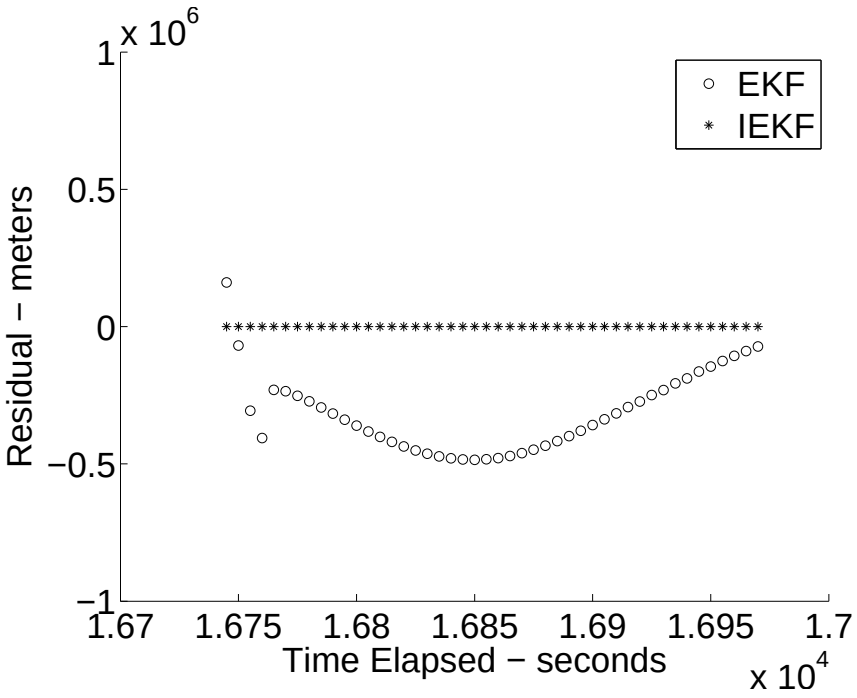


Figure B.22: $\Omega = 0°$ : Residuals After Largest Outage vs. Time

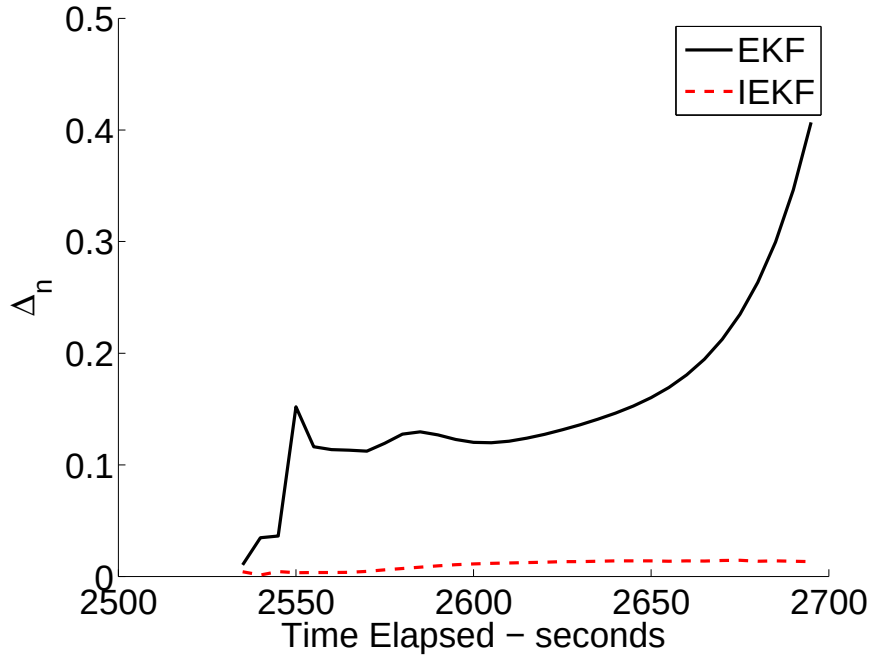


Figure B.23: $\Omega = 0°$ : NMSE Before Largest Outage vs. Time

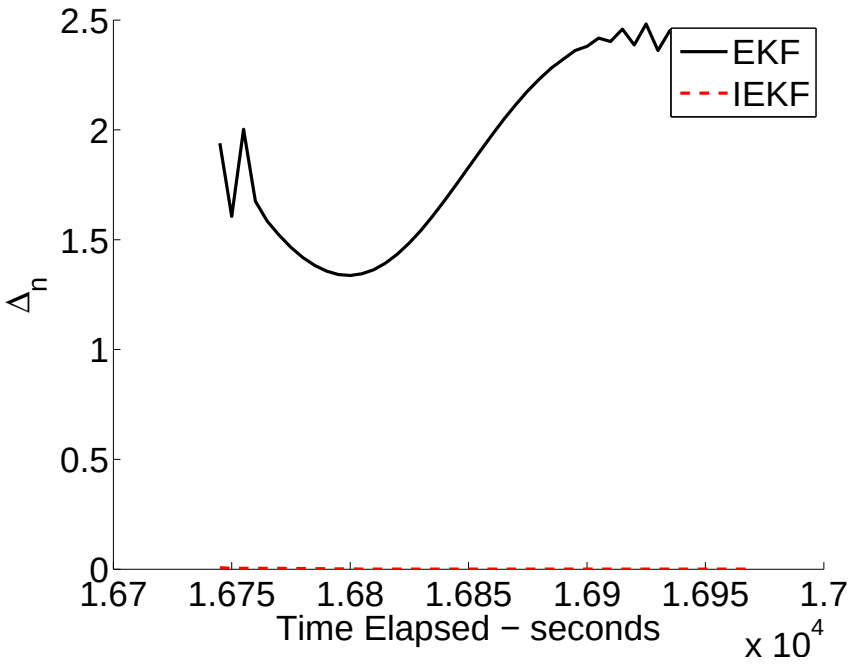


Figure B.24: $\Omega = 0°$ : NMSE After Largest Outage vs. Time

Table B.7: $\Omega = 0°$: Intermediate Output

| | 33 observations (2695 $s$) - Before | | 79 observations (16970 $s$) - After | |
|---|---|---|---|---|
| State | $\alpha$ (EKF) | $\beta$ (IEKF) | $\alpha$ (EKF) | $\beta$ (IEKF) |
| X(m) | 17077.7443 | 93.4052 | 123554.1400 | 47.8484 |
| Y(m) | 65766.6982 | 1981.8738 | 37632.0560 | 70.8962 |
| Z(m) | 8785.4193 | 426.7605 | 54013.8444 | 90.1187 |
| Vx(m/s) | 69.1645 | 2.5717 | 5830.9754 | 0.0089 |
| Vy(m/s) | 402.4925 | 15.1743 | 1819.2047 | 0.1625 |
| Vz(m/s) | 266.2634 | 11.8059 | 7545.5126 | 0.1870 |
| yk(m) | 276.0592 | 4.9075 | 72437.4711 | 2.3038 |
| NMSE | 4.0674E-001 | 1.3350E-002 | 2.2345E+000 | 7.4732E-005 |

Table B.8: $\Omega = 0°$: Output for All Observations (311 - 29325 $s$) Processed

| State | $\alpha$ (EKF) | $\beta$ (IEKF) |
|---|---|---|
| X(m) | 4816071.3633 | 84.0402 |
| Y(m) | 2461167.8588 | 933.7677 |
| Z(m) | 3802048.3414 | 1271.3336 |
| Vx(m/s) | 1871.2821 | 0.4234 |
| Vy(m/s) | 3623.3970 | 1.4689 |
| Vz(m/s) | 5647.5764 | 2.1060 |
| yk(m) | 5243457.7008 | 507.2702 |
| NMSE | 4.0350E+000 | 1.3556E-003 |

### B.3.2 Longitude of the Ascending Node $\rightarrow \Omega = 90°$

Longitude of the Ascending Node 90 degrees

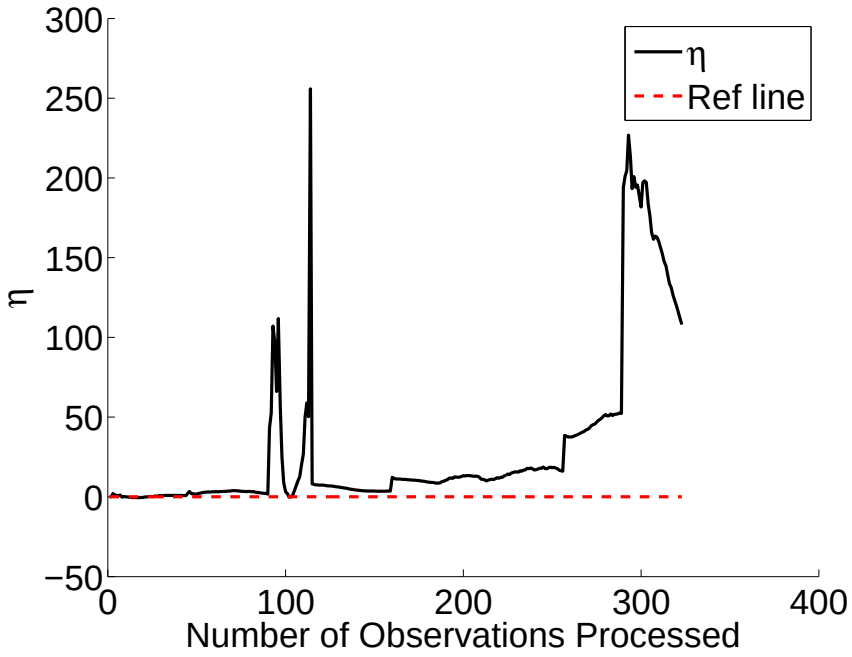


Figure B.25: $\Omega = 90°$ : $\eta$ vs. Number of Observations Processed

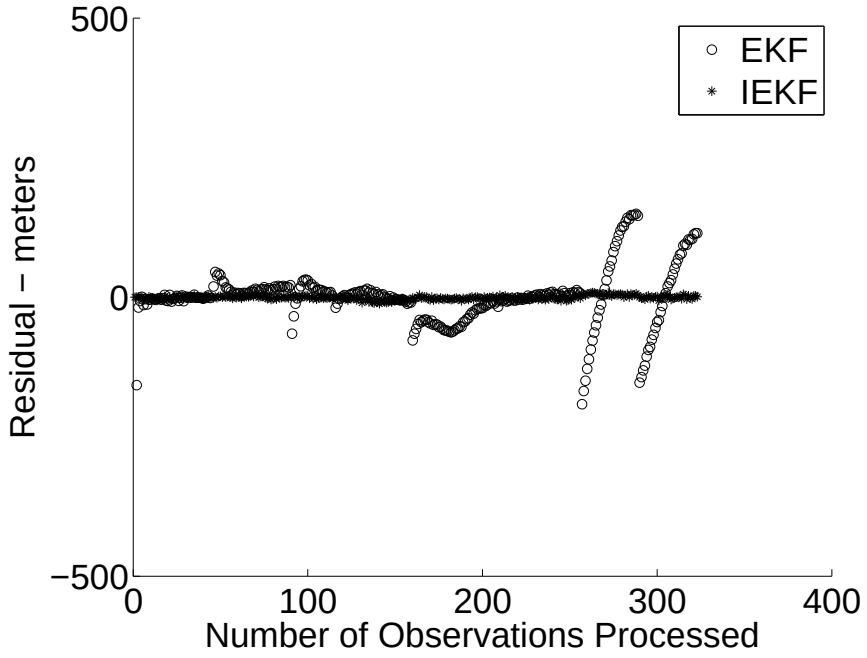


Figure B.26: $\Omega = 90°$ : Residuals vs. Number of Observations Processed

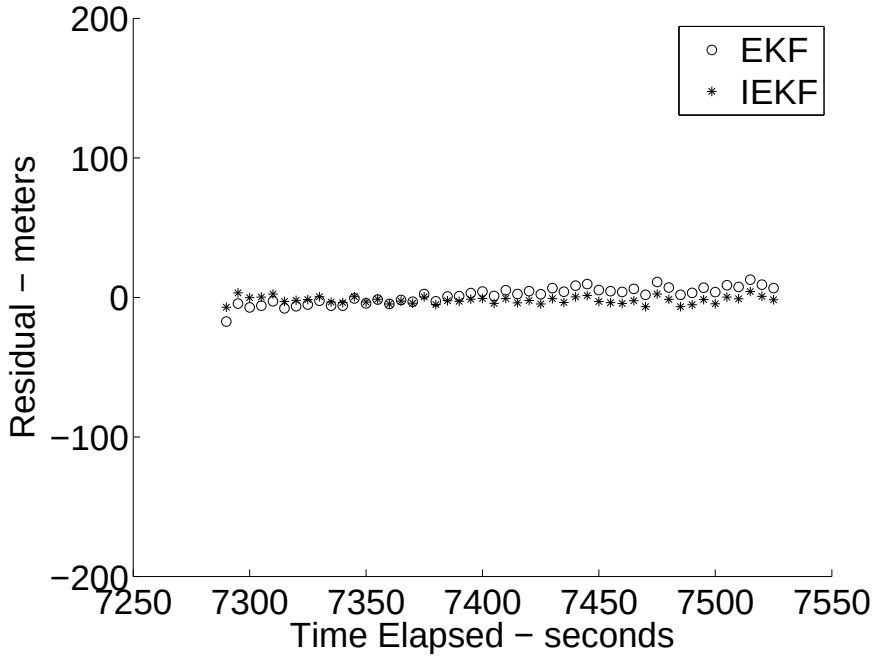


Figure B.27: $\Omega = 90°$ : Residuals Before Largest Outage vs. Time

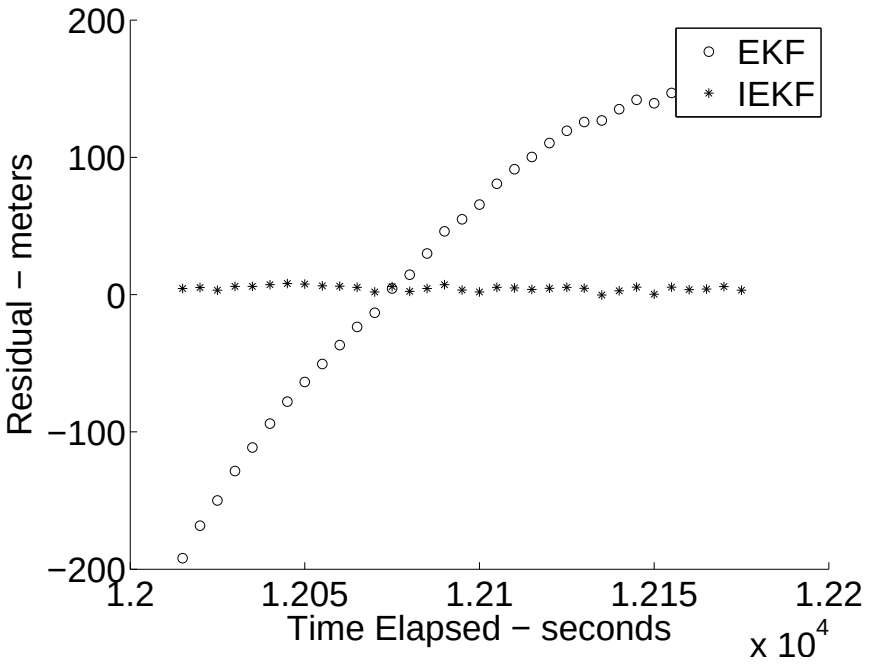


Figure B.28: $\Omega = 90°$ : Residuals After Largest Outage vs. Time

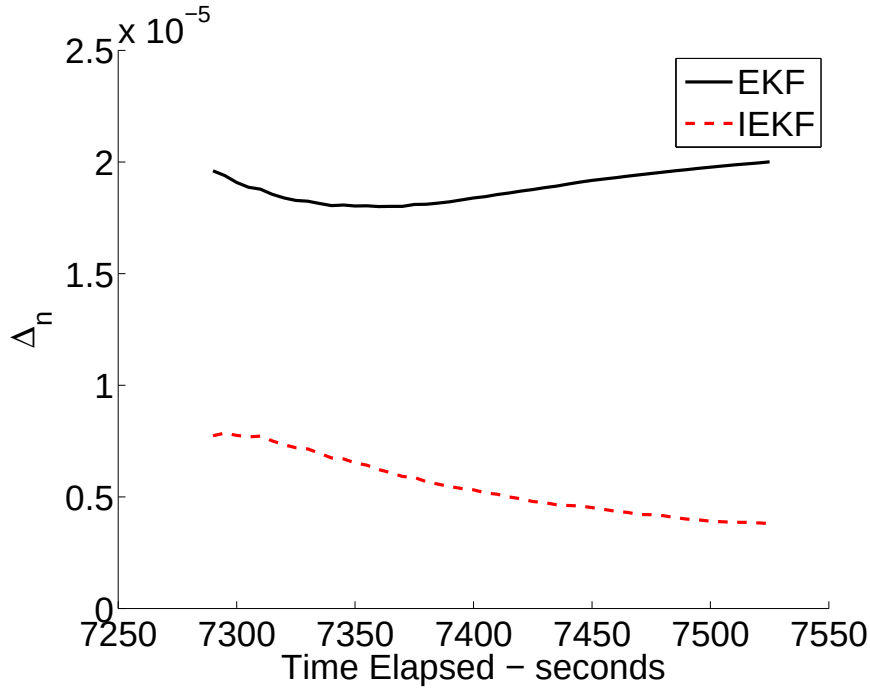


Figure B.29: $\Omega = 90°$ : NMSE Before Largest Outage vs. Time

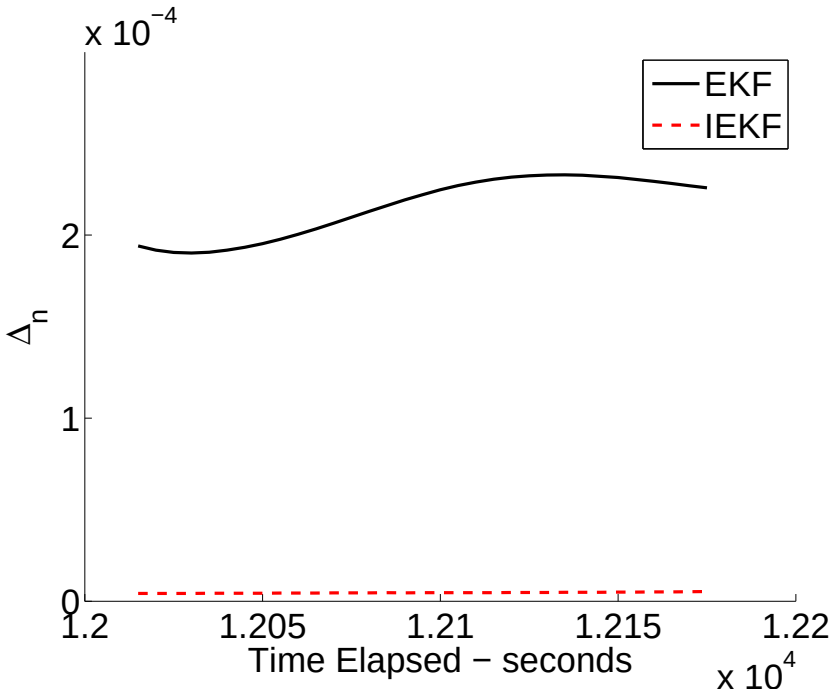


Figure B.30: $\Omega = 90°$ : NMSE After Largest Outage vs. Time

Table B.9: $\Omega = 90°$: Intermediate Output

| | 256 observations (7525 $s$) - Before | | 289 observations (12175 $s$) - After | |
|---|---|---|---|---|
| State | $\alpha$ (EKF) | $\beta$ (IEKF) | $\alpha$ (EKF) | $\beta$ (IEKF) |
| X(m) | 17.1138 | 2.2958 | 48.9182 | 3.0406 |
| Y(m) | 9.8902 | 0.4304 | 216.8610 | 0.9163 |
| Z(m) | 47.6340 | 1.9219 | 9.0753 | 2.7026 |
| Vx(m/s) | 0.0438 | 0.0100 | 0.1633 | 0.0056 |
| Vy(m/s) | 0.0226 | 0.0001 | 0.0819 | 0.0006 |
| Vz(m/s) | 0.0124 | 0.0075 | 0.2202 | 0.0044 |
| yk(m) | 6.6001 | 1.7129 | 145.7722 | 3.2522 |
| NMSE | 2.0006E-005 | 3.8020E-006 | 2.2582E-004 | 5.2616E-006 |

Table B.10: $\Omega = 90°$: Output for All Observations (323 - 12915 $s$) Processed

| State | $\alpha$ (EKF) | $\beta$ (IEKF) |
|---|---|---|
| X(m) | 68.8861 | 1.4080 |
| Y(m) | 141.9399 | 0.7742 |
| Z(m) | 131.4218 | 0.9827 |
| Vx(m/s) | 0.1679 | 0.0061 |
| Vy(m/s) | 0.1082 | 0.0001 |
| Vz(m/s) | 0.1686 | 0.0052 |
| yk(m) | 114.3858 | 0.5844 |
| NMSE | 1.0019E-004 | 2.9362E-006 |

## B.4 Variations on the Argument of Perigee

### B.4.1 Argument of Perigee $\rightarrow \omega = 45°$

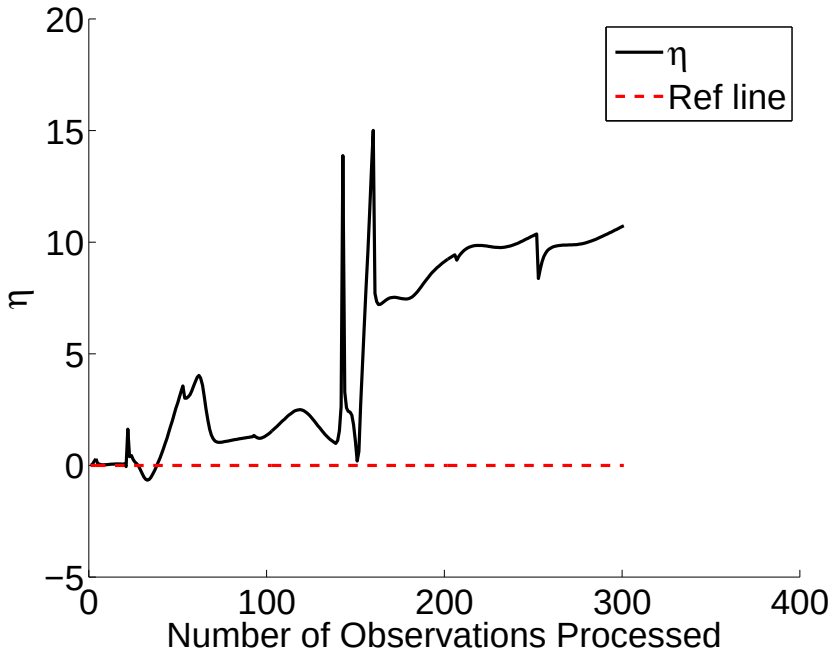


Figure B.31: $\omega = 45°$ : $\eta$ vs. Number of Observations Processed

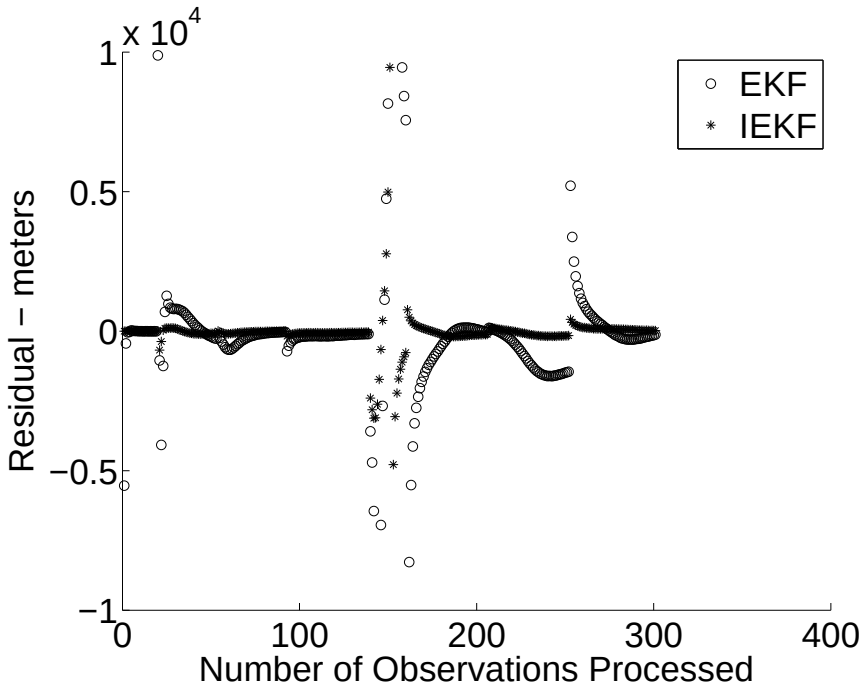


Figure B.32: $\omega = 45°$ : Residuals vs. Number of Observations Processed

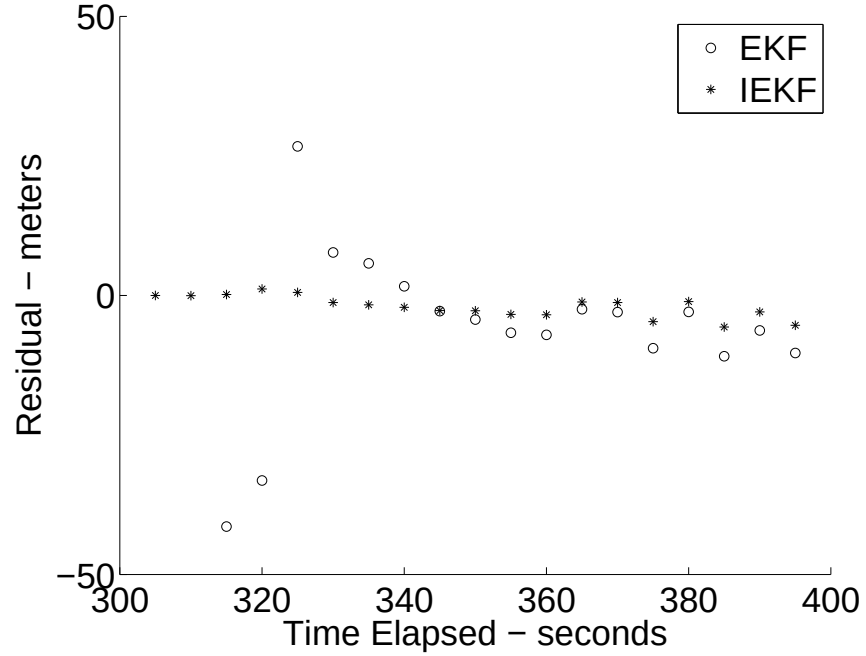


Figure B.33: $\omega = 45°$ : Residuals Before Largest Outage vs. Time

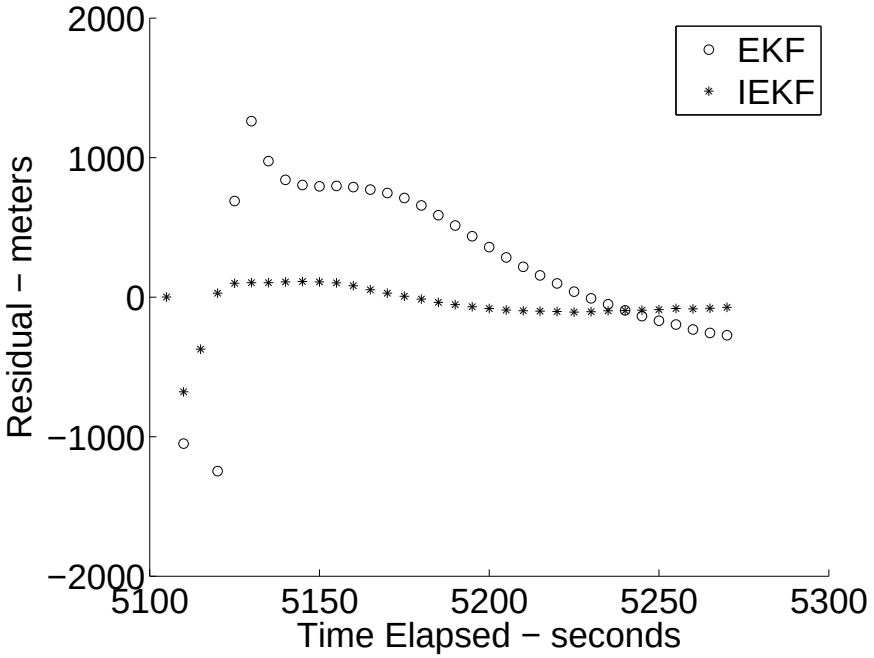


Figure B.34: $\omega = 45°$ : Residuals After Largest Outage vs. Time

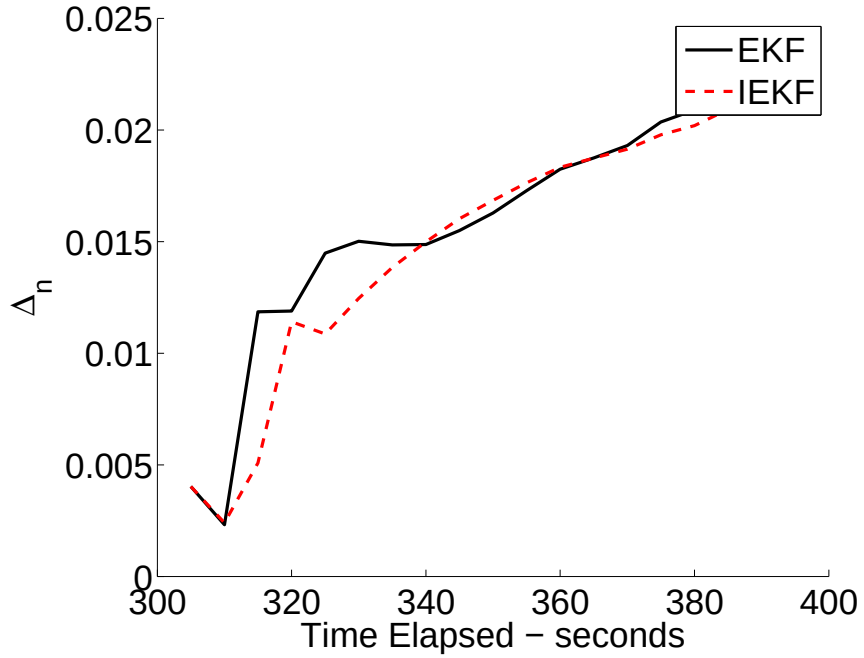


Figure B.35: $\omega = 45°$ : NMSE Before Largest Outage vs. Time

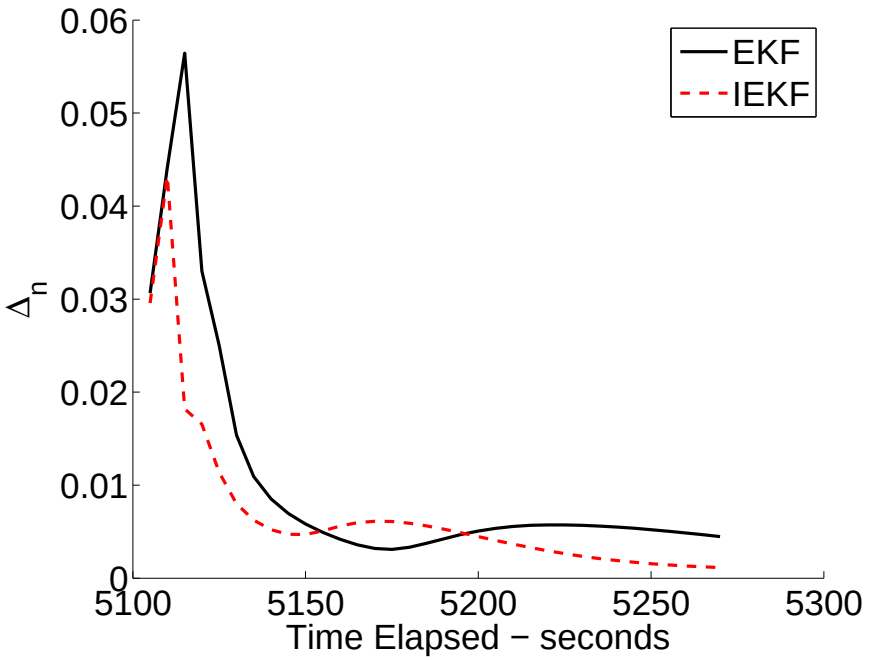


Figure B.36: $\omega = 45°$ : NMSE After Largest Outage vs. Time

Table B.11: $\omega = 45°$: Intermediate Output

| | 19 observations (395 $s$) - Before | | 53 observations (5270 $s$) - After | |
|---|---|---|---|---|
| State | $\alpha$ (EKF) | $\beta$ (IEKF) | $\alpha$ (EKF) | $\beta$ (IEKF) |
| X(m) | 2724.5758 | 2579.9428 | 2986.3228 | 685.4223 |
| Y(m) | 3020.5290 | 2587.4315 | 8828.9447 | 1967.9265 |
| Z(m) | 1015.5812 | 1550.4209 | 7485.3752 | 1595.5966 |
| Vx(m/s) | 34.0881 | 31.3766 | 8.9811 | 0.9847 |
| Vy(m/s) | 3.0843 | 2.3657 | 4.0107 | 1.1805 |
| Vz(m/s) | 13.0670 | 13.8903 | 5.7072 | 3.7943 |
| yk(m) | 10.3421 | 5.3753 | 272.9182 | 72.8696 |
| NMSE | 2.4088E-002 | 2.2472E-002 | 4.4730E-003 | 1.1370E-003 |

Table B.12: $\omega = 45°$: Output for All Observations (301 - 13425 $s$) Processed

| State | $\alpha$ (EKF) | $\beta$ (IEKF) |
|---|---|---|
| X(m) | 2098.7609 | 214.1174 |
| Y(m) | 1943.8066 | 85.5751 |
| Z(m) | 1073.0904 | 120.8817 |
| Vx(m/s) | 3.6188 | 0.2484 |
| Vy(m/s) | 3.2936 | 0.1270 |
| Vz(m/s) | 1.7417 | 0.1291 |
| yk(m) | 129.9064 | 16.1376 |
| NMSE | 2.3449E-003 | 1.9357E-004 |

## B.5 Variations on the True Anomaly

### B.5.1 True Anomaly $\rightarrow \nu = 90°$

True Anomaly 90 degrees

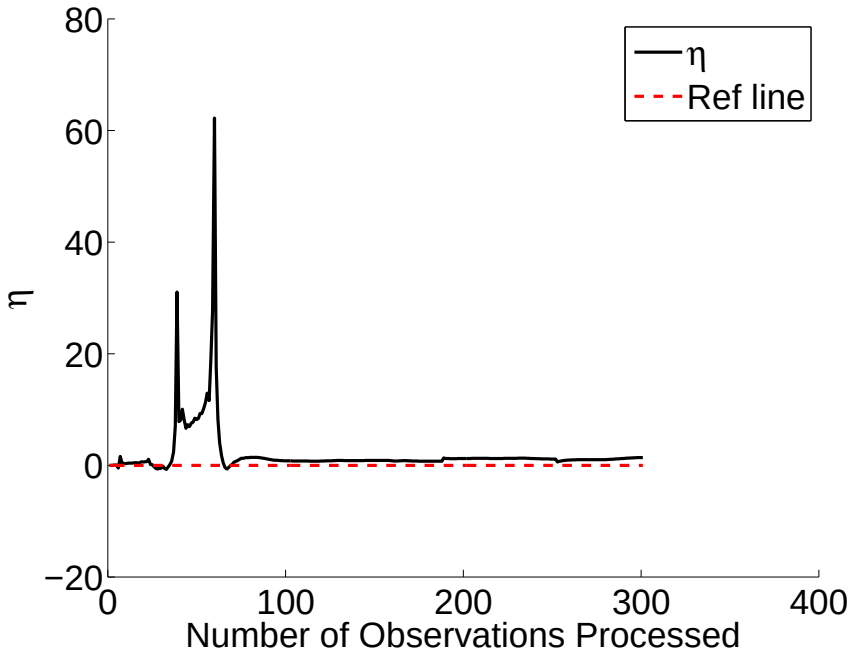


Figure B.37: $\nu = 90°$ : $\eta$ vs. Number of Observations Processed

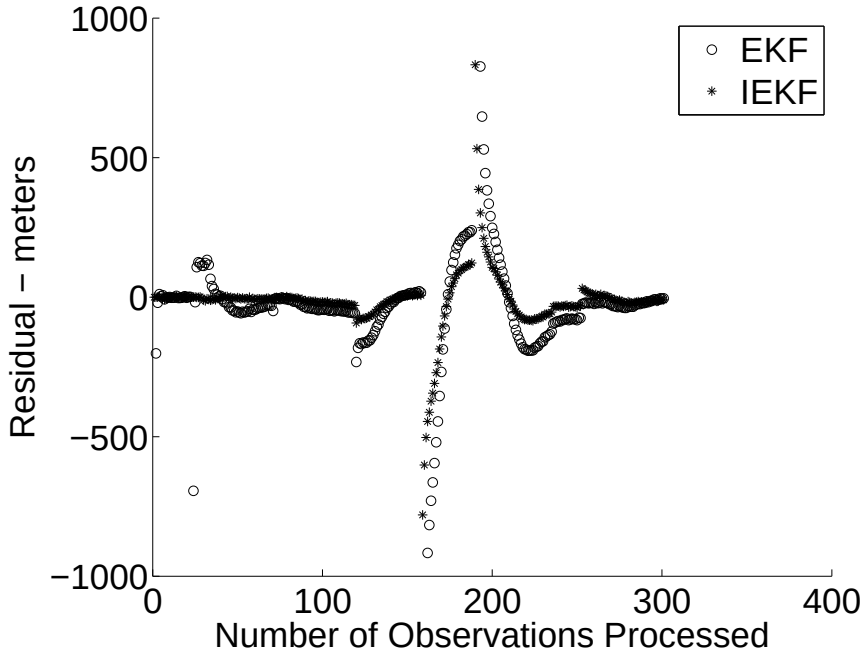


Figure B.38: $\nu = 90°$ : Residuals vs. Number of Observations Processed

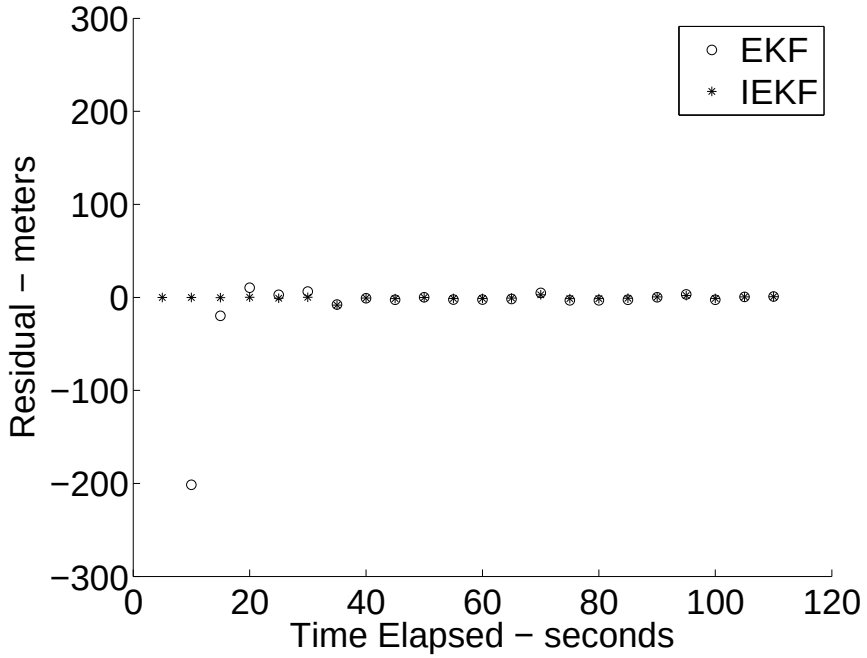


Figure B.39: $\nu = 90°$ : Residuals Before Largest Outage vs. Time

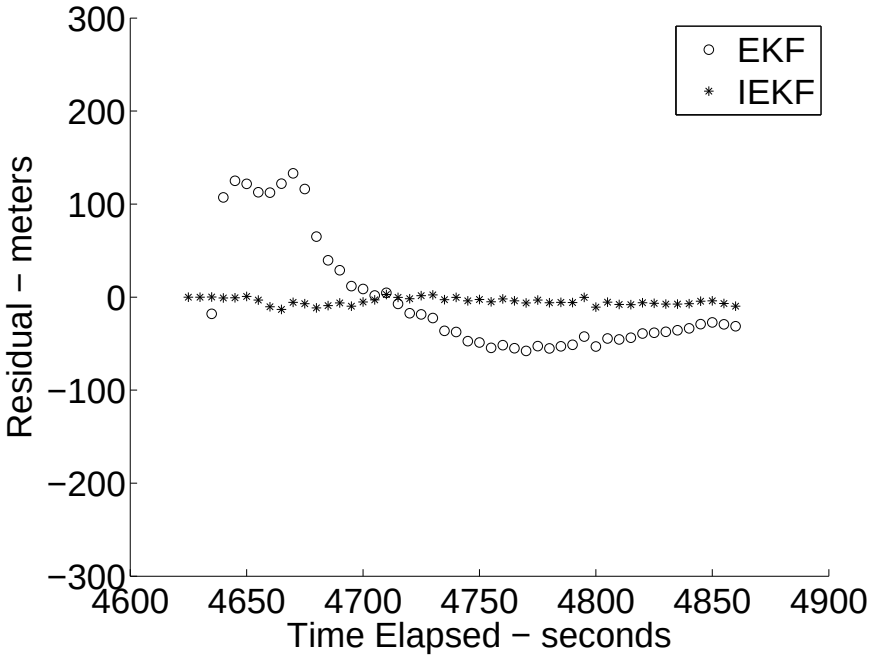


Figure B.40: $\nu = 90°$ : Residuals After Largest Outage vs. Time

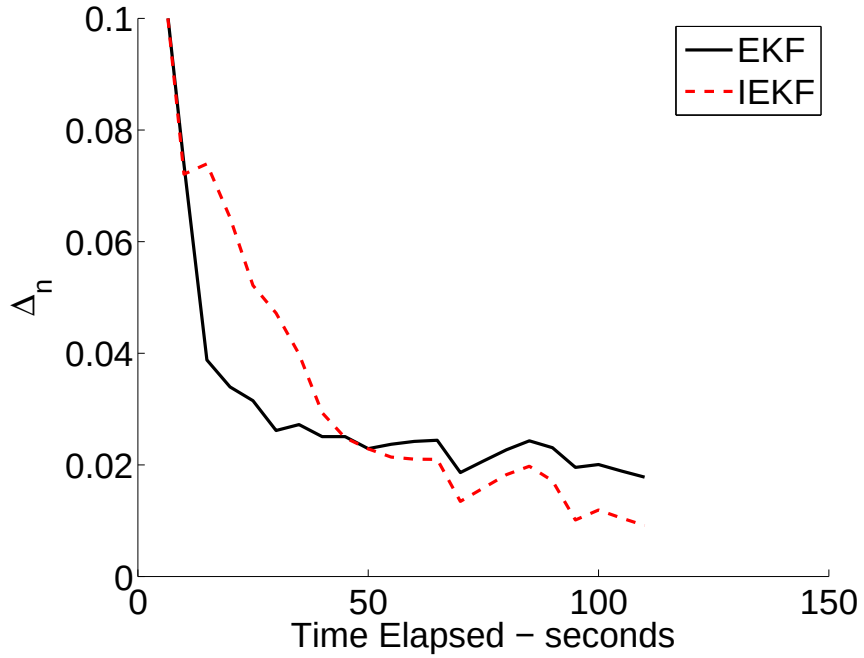


Figure B.41: $\nu = 90°$ : NMSE Before Largest Outage vs. Time

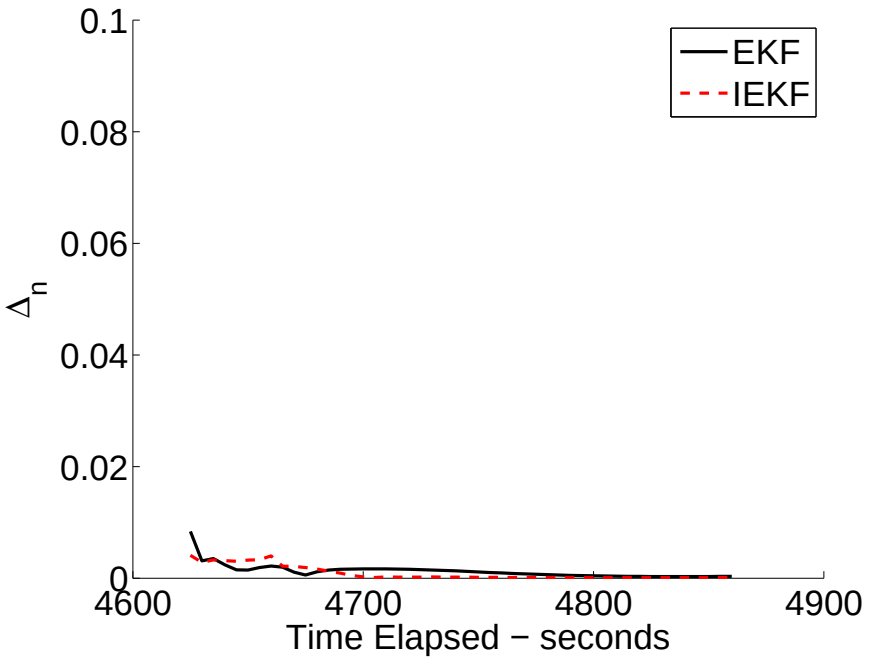


Figure B.42: $\nu = 90°$ : NMSE After Largest Outage vs. Time

Table B.13: $\nu = 90°$: Intermediate Output

| | 22 observations (110 $s$) - Before | | 70 observations (4860 $s$) - After | |
|---|---|---|---|---|
| State | $\alpha$ (EKF) | $\beta$ (IEKF) | $\alpha$ (EKF) | $\beta$ (IEKF) |
| X(m) | 1681.0471 | 583.7434 | 69.6992 | 77.4679 |
| Y(m) | 400.9202 | 16.4311 | 86.4232 | 63.8825 |
| Z(m) | 4112.8134 | 2594.4797 | 150.5687 | 120.9722 |
| Vx(m/s) | 7.1026 | 0.4560 | 0.0970 | 0.1351 |
| Vy(m/s) | 1.3260 | 1.1095 | 0.3631 | 0.0991 |
| Vz(m/s) | 12.1601 | 7.6690 | 1.2757 | 0.3698 |
| yk(m) | 0.8732 | 0.6893 | 31.4049 | 9.8177 |
| NMSE | 1.7805E-002 | 9.1377E-003 | 3.1994E-004 | 1.0862E-004 |

Table B.14: $\nu = 90°$: Output for All Observations (301 - 16150 $s$) Processed

| State | $\alpha$ (EKF) | $\beta$ (IEKF) |
|---|---|---|
| X(m) | 23.1059 | 7.0732 |
| Y(m) | 32.1170 | 6.0575 |
| Z(m) | 53.9966 | 26.2700 |
| Vx(m/s) | 0.0166 | 0.0002 |
| Vy(m/s) | 0.0214 | 0.0048 |
| Vz(m/s) | 0.0642 | 0.0337 |
| yk(m) | 4.7738 | 10.1642 |
| NMSE | 2.7934E-005 | 1.2870E-005 |

### B.5.2 True Anomaly $\rightarrow \nu = 270°$

True Anomaly 270 degrees

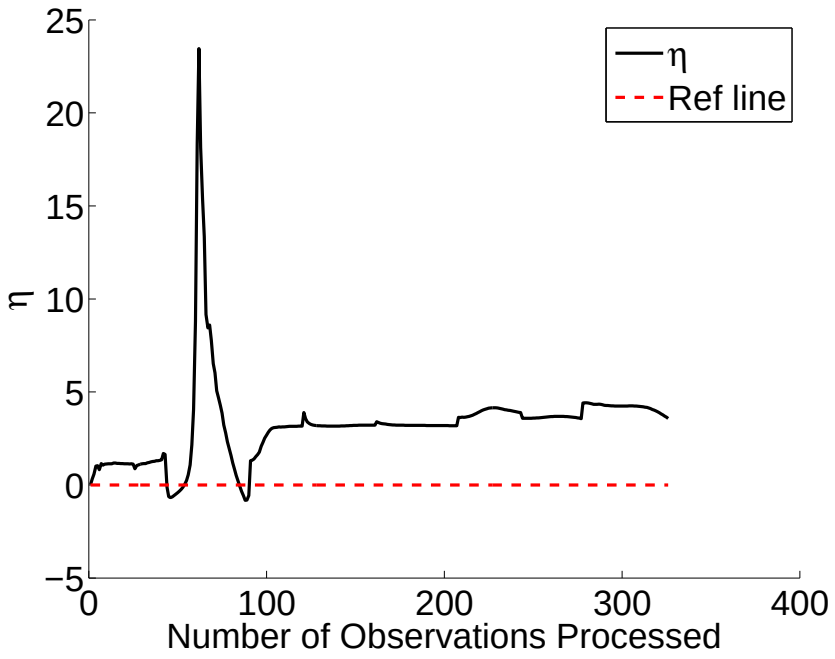


Figure B.43: $\nu = 270°$ : $\eta$ vs. Number of Observations Processed

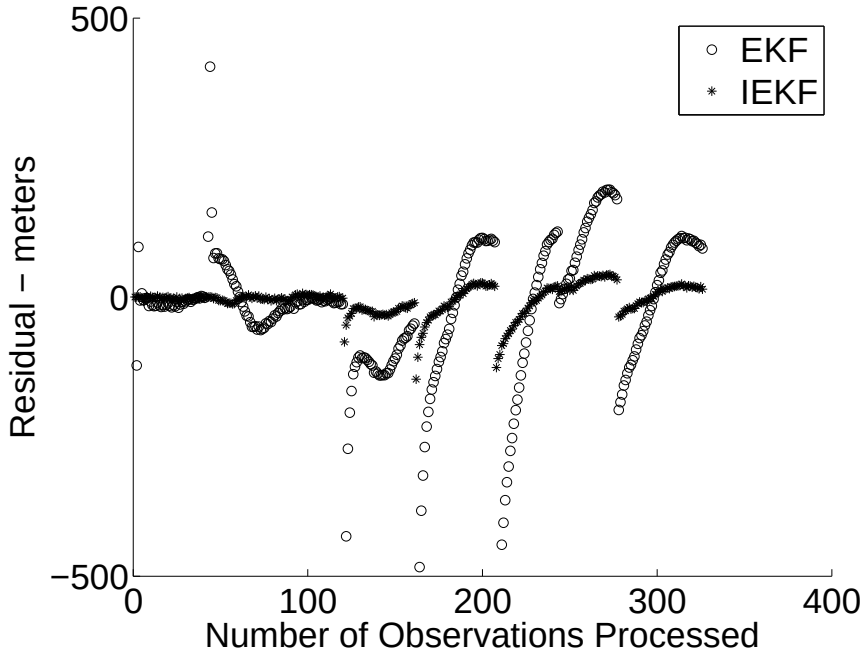


Figure B.44: $\nu = 270°$ : Residuals vs. Number of Observations Processed

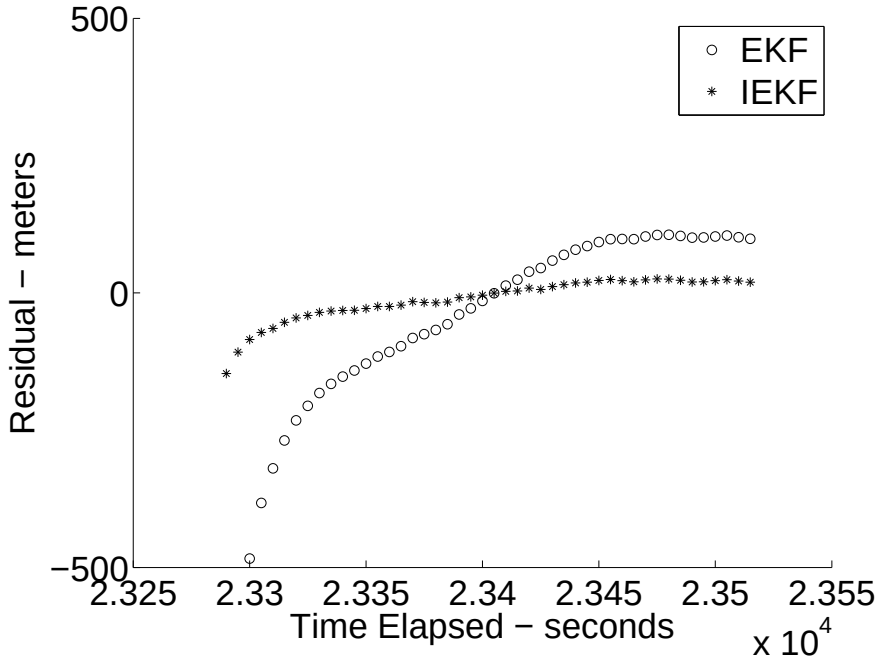


Figure B.45: $\nu = 270°$ : Residuals Before Largest Outage vs. Time

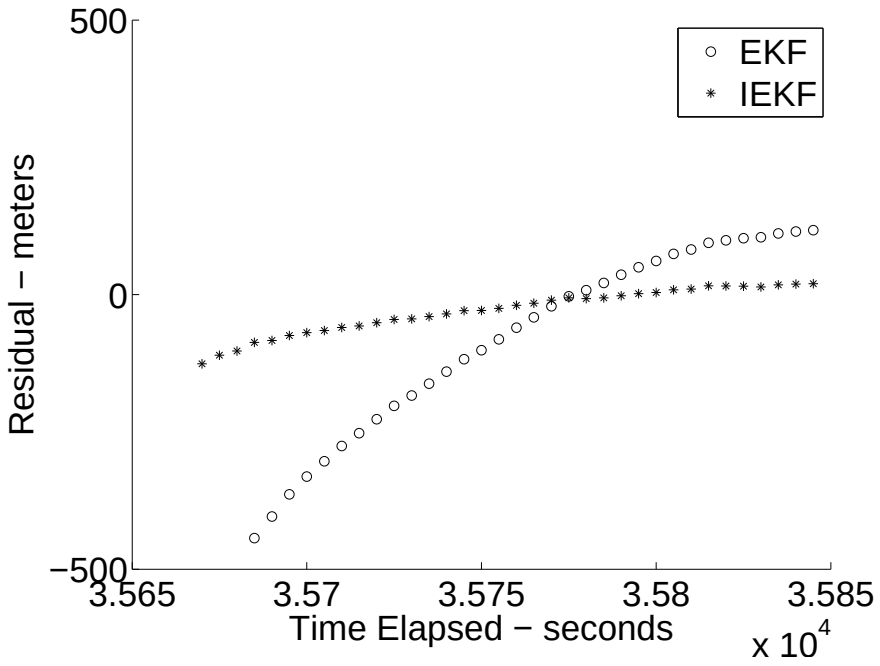


Figure B.46: $\nu = 270°$ : Residuals After Largest Outage vs. Time

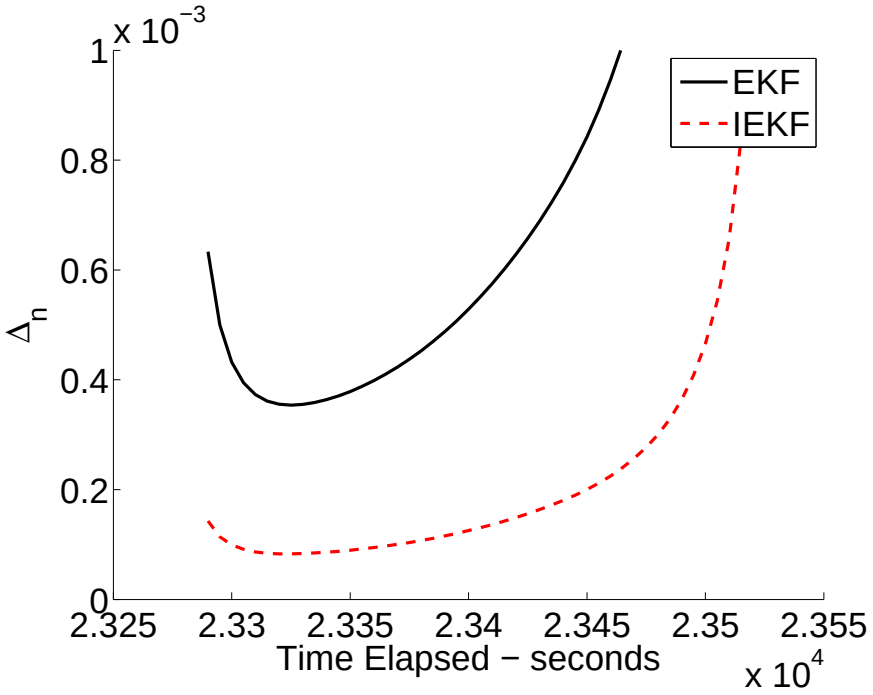


Figure B.47: $\nu = 270°$ : NMSE Before Largest Outage vs. Time

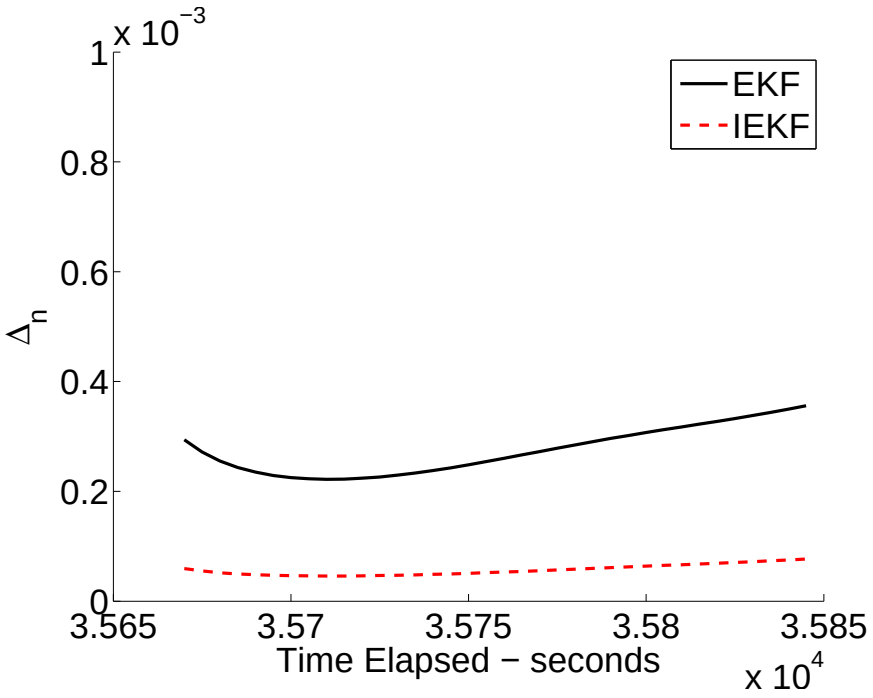


Figure B.48: $\nu = 270°$ : NMSE After Largest Outage vs. Time

Table B.15: $\nu = 270°$: Intermediate Output

| | 43 observations (2,820 $s$) - Before | | 61 observations (2,910 $s$) - After | |
|---|---|---|---|---|
| State | $\alpha$ (EKF) | $\beta$ (IEKF) | $\alpha$ (EKF) | $\beta$ (IEKF) |
| X(m) | 14039.59483 | 2908.0591 | 2122.2537 | 65.95151 |
| Y(m) | 10357.9379 | 206.7330 | 60.4991 | 29.0566 |
| Z(m) | 746.5737 | 6057.0141 | 6353.7477 | 210.5541 |
| Vx(m/s) | 9.5159 | 5.9085 | 7.2863 | 0.2481 |
| Vy(m/s) | 1.3419 | 0.5698 | 0.6326 | 0.2020 |
| Vz(m/s) | 5.3723 | 0.7508 | 0.8307 | 0.1025 |
| yk(m) | 110.1015 | 0.0421 | 11.4919 | 1.5893 |
| NMSE | 3.4027E-002 | 1.6058E-002 | 8.7018E-003 | 3.1182E-004 |

Table B.16: $\nu = 270°$: Output for All Observations (326 - 41630 $s$) Processed

| State | $\alpha$ (EKF) | $\beta$ (IEKF) |
|---|---|---|
| X(m) | 8.8143 | 0.8248 |
| Y(m) | 15.5944 | 8.2807 |
| Z(m) | 92.1830 | 45.0967 |
| Vx(m/s) | 0.0201 | 0.0364 |
| Vy(m/s) | 0.4172 | 0.2035 |
| Vz(m/s) | 0.4210 | 0.1500 |
| yk(m) | 13.8092 | 4.3864 |
| NMSE | 2.1635E-004 | 8.2804E-005 |